A STUDY OF HYDROGENATED NANOCRYSTALLINE SILICON THIN FILMS DEPOSITED BY HOT – WIRE CHEMICAL VAPOUR DEPOSITION (HWCVD).

Sylvain Halindintwali

A thesis submitted in partial fulfilment of the requirements for the degree of Doctor Philosophiae in the Department of Physics, University of the Western Cape.

Supervisor: Prof. Dirk Knoesen

September 2005.

KEYWORDS

Intrinsic silicon

Hot – wire chemical vapour deposition

Amorphous silicon

Protocrystalline silicon

Staebler Wronski effect

Bonded hydrogen

Ordering

Photoresponse

Degradation

ABSTRACT

In this thesis, intrinsic hydrogenated nanocrystalline silicon thin films for solar cells application have been deposited by means of the hot – wire chemical vapour deposition (HWCVD) technique and have been characterised for their performance.
It is noticed that hydrogenated nanocrystalline silicon is similar in some aspects (mainly optical) to its counterpart amorphous silicon actually used as the intrinsic layer in the photovoltaic industry. Substantial differences between the two materials have been found however in their respective structural and electronic properties.
We show that hydrogenated nanocrystalline silicon retains good absorption coefficients known for amorphous silicon in the visible region. The order improvement and a reduced content of the bonded hydrogen in the films are linked to their good stability.
We argue that provided a moderate hydrogen dilution ratio in the monosilane gas and efficient process pressure in the deposition chamber, intrinsic hydrogenated nanocrystalline silicon with photosensitivity better than 10^2 and most importantly resistant to the Staebler Wronski effect (SWE) can be produced.
This work explores the optical, structural and electronic properties of this promising material whose study – samples have been exclusively produced in the HWCVD reactors based in the Solar Cells laboratory of the Physics department at the University of the Western Cape.

September 2005.

DECLARATION

I declare that *A Study Of Hydrogenated Nanocrystalline Silicon Thin Films Deposited By Hot – Wire Chemical Vapour Deposition (HWCVD)* is my own work, that it has not been submitted for any degree or examination in any other university, and that all the sources I have used or quoted have been indicated and acknowledged by complete references.

Sylvain Halindintwali

September 2005

Signed: 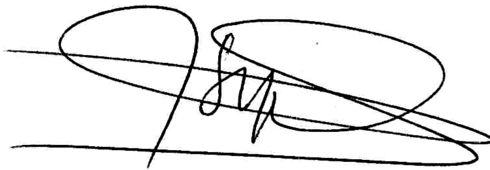

To

My late father *Jean Baptiste Gahigi* who taught me the first numbers.

ACKNOWLEDGEMENTS

God Almighty who kept me alive and opened for me this door of opportunities.

I am grateful to the following people without whose support and guidance, the thesis would not have been possible:

Prof. Dirk Knoesen of the Physics Department at the University of the Western Cape (UWC) to have promoted the thesis, for his worthy guidance, patience and continuous support throughout this investigation.

Prof. Ryno Swanepoel of the Physics Department at UWC, co – supervisor of the thesis, who accepted to share his expertise in optical analysis. His guidance during all the time Prof. D. Knoesen was away on sabbatical is fully acknowledged.

Dr. Chris Theron of iThemba LABS, co – supervisor of the thesis, whose knowledge and expertise in ions beam studies have been instrumental in this work. His contribution in organizing the funding of this project is also acknowledged.

Prof. D. Britton of the Physics Department at the University of Cape Town (UCT) is acknowledged for his help during the soaking experiments and for his enlightening discussions at various occasions.

Proff. Werner van der Weg and Ruud Schropp of Utrecht University in the Netherlands, external supervisors of the thesis, for their guidance and sustained help during my stay at Utrecht in 2004.

Dr. Jatin Rath of Utrecht University for his valuable discussions and suggestions on Raman and conductivity data analysis.

Dr. A. Gordijn, Drs. P.C.P.Bronsveld and H.Li of Utrecht University for their help in Raman, conductivity and PDS measurements during my visit at Utrecht. Dr. H. Goldbach and Drs. V. Verlaan are also acknowledged for their help with the FTIR measurements during the same period.

Dr. Chris Arendse, Messrs. T. Muller and Nolan Botha to have welcomed me with kindness in the solar cells research group in the Physics department at UWC. Their help and friendship eased my integration in the department and allowed me a smooth start of the project.

Dr. Basil Julies and Dr.Gerald Malgas of the microscopy group at UWC, for their help in SEM and TEM investigations. Dr Malgas is especially thanked for his help with computer software during my early days at UWC.

Proff. D. Adams and R. Lindsay of the Physics department at UWC for their help and support in their capacity as Heads of the department and for their interest in the project.

Prof. M. Härting, Ms. Terry Davis of the Physics and the Geology departments at UCT, Dr. Remy Bucher, Mr. Tshepo Ntsoane of iThemba LABS, Dr. Maren Hempel formerly of iThemba LABS for their help in XRD measurements and analysis.

Mr. Timothy Lesch of the Chemistry Department at UWC for his help with the FTIR measurements.

Mr. Karl Springhorn of iThemba LABS (formerly the National Accelerator Centre) for his assistance with the ERD measurements.

Mssrs. Evariste Minani, Schadrack Nsengiyumva and Girma Goro Gonfa of the Physics department at UCT for their valuable assistance in the samples degradations measurements.

Other fellow Material Research students in the time: Messrs. Shiradz Majiet and George Odhiambo, for their friendship and support.

The staff and other post-graduate students of the Physics Department at UWC for their constant support and encouragement. Dr. R. Nchodu and Dr. Shaun Wyngaardt, formerly at UWC are acknowledged for their diverse support and helpful discussions.

My close family: Albertina, Boris and Dorianne for their love and patience.

A special thank - you to Lily and Werner van der Weg, Liliana and Ernst van Faassen for their friendship and companionship during my visit in Utrecht.

My friends Narcisse Nduwayezu, Gaspard Hitiyaremye, Callixte Rushemeza, the Louw and Frans families for their support.

The National Research Foundation, iThemba LABS, the Physics Department at UWC, Utrecht University through the "van der Weg" scholarship for their financial assistance during the course of this investigation.

Sylvain Halindintwali

September 2005.

Contents

KEYWORDS ... ii
ABSTRACT ... iii
ACKNOWLEDGEMENTS ... vi
Preface ... 3
Chapter 1. Introduction ... 5
1.1. Overview of Solar cells ... 5
1.1.1. Definition ... 5
1.1.2. c-Si vs. a-Si: H band structure ... 5
1.1.3. Semiconductor junction ... 8
1.1.4. Junction bias ... 10
1.1.5. Light absorption (optical excitation) by a semiconductor ... 11
1.2. Aim and outline of this thesis ... 12
Chapter 2. Hot-wire chemical vapour deposition ... 14
2.1. The HWCVD chambers ... 14
2.2. The HWCVD process ... 14
2.3. Nanocrystalline silicon in HWCVD ... 17
2.4. Keys issues pertaining to the deposition process in HWCVD ... 18
2.4.1. Deposition rate (r_d) ... 18
2.4.2. The role of the filament ... 19
2.4.3. The role of hydrogen dilution ... 20
2.4.4. Influence of pressure ... 21
2.4.5. Incorporation of hydrogen ... 21
Chapter 3. Analysis techniques ... 23
3.1. Optical Characterization ... 23
3.1.1. Optical Absorption and Energy Gap ... 23
3.1.2. Experimental determination of the refractive index and thickness ... 25
3.1.2.1. Case of film with uniform thickness ... 25
3.1.2.2. Case of film with non uniform thickness ... 29
3.1.2.3. Relation with the spectrum of a uniform thickness ... 34
3.2. X-rays Diffraction characterization ... 36
3.2.1. Electromagnetic radiation ... 36
3.2.2. Absorption of X-rays ... 37
3.2.3. Depth of X-Rays Penetration ... 38
3.2.4. Diffraction of X- rays ... 39
3.3. Raman Spectroscopy ... 40
3.3.1.Theoretical background ... 40
3.3.2. Application on thin films ... 43
3.4. Fourier transform infrared spectroscopy ... 44
3.4.1. Fundamentals ... 44
3.4.2. Hydrogen content and bonding in hydrogenated silicon ... 45
3.5. Elastic Recoil Detection ... 48

3.5.1.Theoretical background 48
3.5.2. The experimental set-up 53
3.6. Transmission electron microscopy (TEM) Analysis 55
3.6.1. Theoretical background 55
3.6.2. Specimen preparation 57
3.7. Electrical measurements 60
3.7.1. Dark and photo-conductivity 60
3.7.2. Conductivity and Mobility 61
3.7.3. Activation energy measurements 62
Chapter 4. Results and Discussion 64
4.1. Layer growth 65
4.1.1. Influence of hydrogen dilution on the deposition rate 65
4.1.2. Influence of the process pressure on the deposition rate 66
4. 2. Optical properties 67
4.2.1. Refractive index 68
4.2.1.1. Variation of n_0 with hydrogen dilution ratio 70
4.2.1.2. Influence of the pressure on n_0 71
4.2.2. Absorption coefficient 72
4.2.2.1. Influence of the hydrogen dilution ratios on α 73
4.2.2.2. Influence of the pressure on α 74
4.2.3. Optical energy gap 76
4.2.3.1. Influence of the hydrogen dilution on the energy gap E_g 78
4.2.3.2. Influence of the process pressure on the energy gap 80
4.3. Phase transitions 81
4.3.1. Results of films grown at low substrate heater temperature 82
4.3.2. Results of the material grown at moderate substrate temperature 84
4.3.3. Results of the material grown at high substrate temperature. 88
4.3.4. UV reflection probe on microcrystallinity 95
4.3.5. Phase diagram 97
4.4. Hydrogen content and order in the material 101
4.4.1. Hydrogen content in films grown at high substrate temperature 102
4.4.2. Hydrogen content in films grown at moderate substrate temperature 110
4.4.3. Ordering in amorphous Si films 116
4.5. Electrical properties 117
4.5.1. Photoresponse of the films grown at high temperature 118
4.5.2. Photoresponse at low substrate temperature 120
4.5.3. Electronic properties at moderate substrate temperature 122
4.5.3.1 Photoresponse 122
4.5.3.2. Activation energy 124
4.5.3.3. Degradation of the films 127
Summary and conclusions 130
References 132
Appendices 139
Curriculum vitae 148

Preface

Energy is an essential necessity to human daily life and is closely linked to the quality of life; the more a person enjoys a wide range of energy services, the better is his quality of life.

From early days, people have relied on the traditional biomass and the readily available sun radiation to sustain their lives. The supply was then unlimited and the energy itself was not an issue. However since the age of industrialisation only a few decades ago, people have shifted from non – commercial to commercial forms of energy. The new needs of the new era have prompted beneficiaries in industrialised countries to move from the use at small scale of traditional and renewable source energy to the extensive exploitation of the non – renewable fossil fuels (coal, oil, natural gas) reserves. Considering the energy full chain from extraction to services whose list extended with the industrialisation boom, the energy sector became a profitable business and has been linked ever since to human activity and development in all facets. As the rapid market was expanding and requiring an increased fuel supply, an equal pressure on the environment was observed. Founded concerns have now raised the public awareness on air pollution and ecosystem degradation so that global warming and climate change have became a global issue.

Another equally important issue is the non – availability and / or the non – affordability of electricity in developing countries; world – wide 2 billion people are without access to electricity and an equal number continue to use traditional solid fuels for cooking[1].

A way forward is to design proper energy security schemes that will require from diverse policy makers, governments, civil society and the scientific community to join hands and promote new affordable and sustainable forms of energy.

---

[1] WED (World Energy assessment), *Energy and the challenge of sustainability*, UNDP (United Nations Development Programme), Bureau for Development Policy, One United Nations Plaza, New York, NY 10017 (2000).

It is a fact that fossil fuels will be depleted and at the present rate of energy consumption, the earth's remaining fossil fuel reserves can only last up to 500 years[2]. Nuclear energy is also increasingly meeting public resentment due to concerns related to its safety, its waste disposal drawback and most importantly the risk of nuclear weapons proliferation. New Renewable (modern biomass, small hydropower, geothermal energy, wind energy, solar energy and marine energy) are tipped to play an ever increasing role in possible scenarios to future energy supply frameworks. The supply is indeed huge, potentially unlimited and without ecological pollution. To make them however competitive vis-à-vis to the conventional sources of energy will require, beside the political will, a sustained effort in increasing their conversion efficiency and in reducing their cost.

This thesis is a modest contribution to the ongoing debate on the how to produce a silicon based photovoltaic intrinsic material potentially resistant to the efficiency degradation during use.

Sylvain Halindintwali

September 2005.

[2] WEC (World Energy Council), *Survey of energy resources*, http://www.worldenergy.org/wec-geis/publications/reports/ser/solar/solar.asp

Chapter 1. Introduction

1.1. Overview of Solar cells

1.1.1. Definition

A solar cell can be defined as a fundamental power conversion unit of a photovoltaic system.
They are usually manufactured from semiconductor materials. The ultimate goal is to extract maximum power from the device while keeping the cost to a minimum.
The physical principle behind the process is the ability of the semiconductor material to convert sunlight into electricity by the photovoltaic effect.
Several types of semiconductors can be used as intrinsic layers: Silicon in its crystalline or polycrystalline state, copper indium diselenide ($CuInSe_2$), gallium arsenide (GaAs), cadmium telluride (CdTe) and hydrogenated amorphous silicon (a-Si:H).
This last one has been the object of intense research in many groups worldwide during the last two decades because of its low production cost and the fact that it can be deposited at large scale on any substrate. The research on a-Si:H devices was started in 1976 by Carlson and Wronski at RCA Laboratories with the development of photovoltaic devices [1].
The amorphous silicon structure is viewed as a continuous random network where each silicon atom is fourfold coordinated.

1.1.2. c-Si vs. a-Si: H band structure

Si is a group IV elemental semiconductor, which falls in the so-called diamond lattice structural group where each atom has four nearest neighbors at the vertices of a tetrahedron.

The energy width between the conduction and valence bands (band gap) in crystalline silicon has a value of 1.12 eV versus more or less 1.75 eV for hydrogenated amorphous silicon.

The short-range order of the amorphous phase is similar to that of the crystalline phase only for distances less than 2 nm. [2]

The broadening of the a-Si:H gap lies in its own configuration: The material lacks long-range order, and distortions in both bond length and bond angle (from the tetrahedral value of 109.5°) are observed. Fig.1.1.(a) illustrates this fact. This disorder in atomic configuration perturbs the energies of the electronic states causing the broadening of the band in contrast to c-Si where the bands edges are sharp (fig.1.1.(b)). The existence of the defect densities in the band gap of around 10^{19} cm^{-3} in pure amorphous silicon [3] constitutes good recombination centers and decreases the photoconductivity. The crucial role of hydrogen is to passivate those dangling bonds.

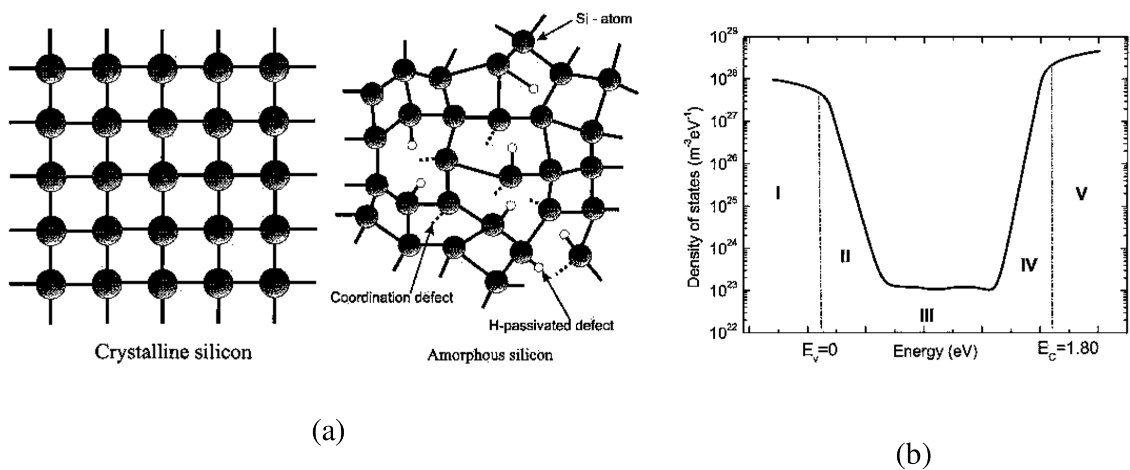

Figure 1.1. (a) The general schematic illustration of the atomic structure of crystalline and amorphous silicon.

(b) Schematic diagram for the density of states in amorphous silicon showing the extended states (I and V), the tail states (II and IV) and the midgap states region (III) [4].

In amorphous silicon, the uncertainty in the wave vector is of the same order as the wave vector itself ($\mathbf{k} = \mathbf{p} / \hbar$) with the consequence that the momentum is no longer a good quantum number and is not conserved in optical transitions [4]. There is then no selection rule imposed for photon absorption like in c-Si, where the only allowed transitions are the ones that conserve the momentum. That is why the a-Si is said to have a direct band gap and the probability of transition is greater than in case of c-Si where the electronic transition is phonon assisted because the minimum in the conduction band is located away from k = 0 as shown in fig.1. 2.

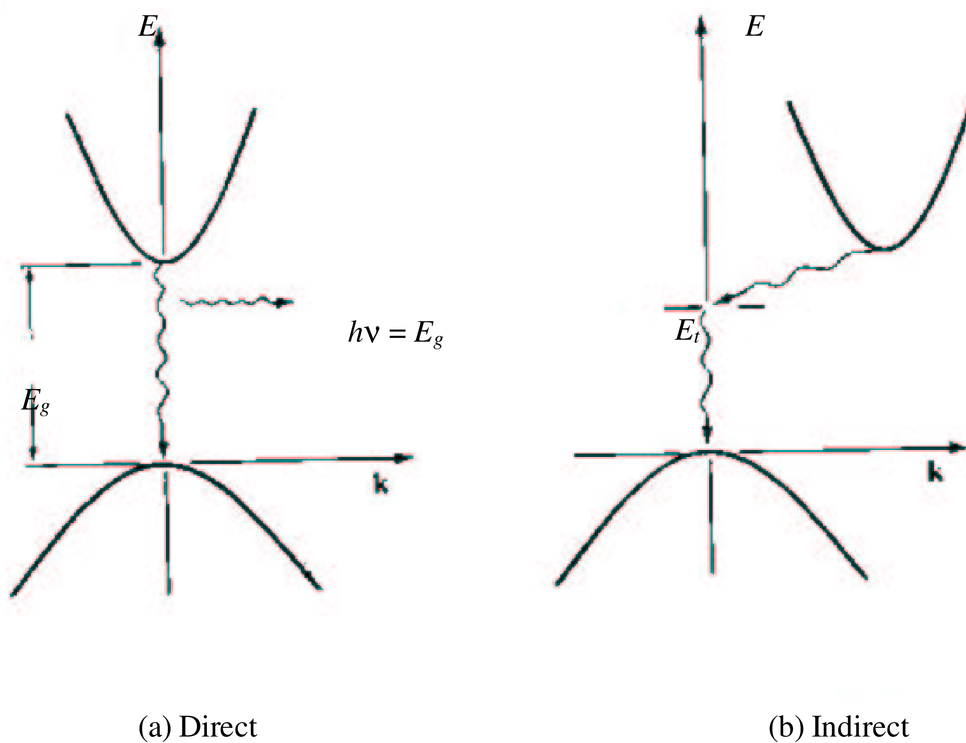

(a) Direct (b) Indirect

Figure 1. 2. E-K diagrams of electron transition from the conduction band to empty (hole) states in the valence band for (a) direct band –gap materials such as GaAs, a-Si, and (b) indirect band-gap materials such as c-Si. [5]

This fact translates into a higher absorption coefficient for a-Si; a very thin film of a-Si will for instance be enough to absorb a certain portion of the spectrum where several thousands of microns of c-Si will be needed to absorb the same part of the spectrum.

An intrinsic semiconductor will conduct electricity only if the carriers are introduced into the conduction band or removed from the valence band. This is done with alloying the intrinsic material with impurities or doping. a-Si: H can be doped *n* and *p* as found in 1975 by Spear and LeComber [6].

The prevailing charge carriers in a semiconductor are called majority carriers, the opposite type of much lower concentration are said to be minority carriers.

The electrons are then majority carriers in *n*-type semiconductor, where the holes are minority carriers, while the holes are majority carriers in the *p*-type semiconductor and the electrons minority carriers.

1.1.3. Semiconductor junction

A *p-n* junction occurs at the interface between *n* and *p* regions; when the two parts originate from the same semiconductor (same bandgap) the junction is said to be a homojunction.

The equilibrium condition is defined in terms of the chemical potential. The Helmholtz thermodynamic free energy function *F* can be expressed [7]:

$$dF = -S\,dT - P\,dV + \mu\,dN \quad (1.1)$$

where *S* is the entropy of the system, *P* the pressure, *V* the volume, *T* the temperature and *N* the number of atoms per unit volume and μ is the chemical potential.

As the condition of equilibrium requires the temperature, the pressure and the atomic species to be homogeneous in the system, we can write (for constant volume)

$$\mu = \partial F / \partial N \quad (1.2)$$

The condition of equilibrium of atoms means that the chemical potential energy is the same for all the atoms in the system; this is not applicable to electrons in equilibrium since the exclusion principle would be violated. The energy spectrum of electrons is better described by the Fermi – Dirac distribution [7],

$$F_{FD}(E) = \frac{1}{\exp[(E-\mu)/kT]+1} \tag{1.3}$$

where μ is the electron chemical potential or the Fermi level. At 0K, the Fermi level is equal to the Fermi energy E_F, which is the highest energy level in the electron distribution.

The electrical equilibrium imposes on the system to have the same Fermi level everywhere, meaning that the junction formation is accompanied by a flow of carriers across the junction in order to align their respective Fermi levels. This is illustrated in the fig.1.3. with the subsequent built-in potential V_{bi} .

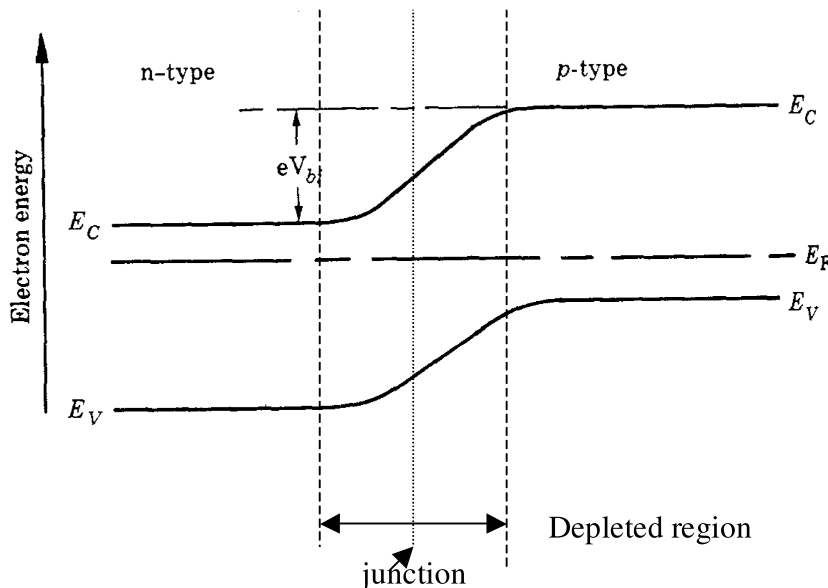

Figure 1.3. The energy band diagram of a p-n junction with a built-in potential V_{bi}.

Because of the electron surplus in the *n*-type zone and surplus of holes in the *p*-type zone, a diffusion phenomenon of the majority carriers across the junction is observed leaving the transition zone depleted of carriers.

The electrons diffuse from *n*-zone to *p*-zone leaving a positive charge ⊕ in the *n*-zone; similarly the holes (majority carriers in the *p*-zone) diffuse from *p* to *n*-zone leaving behind a negative charge - in the *p*-zone. An electric field ***E*** (oriented from the ⊕ charged zone *n* to the – charged zone *p*) is created generating a potential barrier *V* across the junction. This electric field then promotes the holes from the positively charged *n* to the negatively charged *p*-zone and the electrons from *p* to *n*-zone. The created electric field acts then against the majority carriers, promoting instead the minority ones.

1.1.4. Junction bias

When a positive voltage is applied to the *p*-side, the height of the potential barrier is reduced and an increase in diffusion current I_d through the diode is observed, the junction is said to be forward biased**;** on the other hand when a negative voltage is applied to the *p*-side, the height of the barrier is increased and no diffusion current can flow through the junction, only a small current I_0 (the dark saturation current) due to the promoted minority carriers. The diode is said to be reversed biased**.**

The reason why the saturation current in the dark is small is explained by the fact that the minority carriers in an intrinsic material are in small number unless a thermal excitation is involved.

The mathematical expression of the *I-V* characteristic for an ideal diode is given by the Schockley formula [8],

$$I = I_0 \left[\exp(\frac{qV}{kT}) - 1 \right] \qquad (1.4)$$

where the q is the elemental charge

V is the applied voltage

k is the Boltzmann constant

T is the temperature in Kelvin

It is seen from the equation above that at T = 0K, I_0 is negligible while its contribution is more appreciable when the temperature increases.

1.1.5. Light absorption (optical excitation) by a semiconductor

It is known from the quantum mechanics theory that light has dual properties of a wave and a particle. Each particle (photon) carries an energy given by

$$E_{ph}(\lambda) = \frac{hc}{\lambda} \qquad (1.5)$$

Where h is the Planck constant,

c is the speed of light,

λ is the wavelength of light.

On a clear day a number of about 4.4×10^{17} photons fall on a square centimeter on the earth surface per second from the sun. Those with energy $\geq E_g$ are absorbed in a semiconductor and create electron-hole pairs. The role of the electric field $\boldsymbol{E}$ is to promote the created carriers (electrons from p-side to n-side and holes from n-side to p-side) and a current I_L with opposite direction to the diode dark current I_d is generated. It is given for an ideal diode by:

$$I = I_L - I_0\left[\exp\left(\frac{qV}{kT}\right) - 1\right] \qquad (1.6)$$

The upper limit in voltage that a solar cell can generate is given by [2]

$$V = \frac{E_g}{q} \qquad (1.7)$$

A straightforward conclusion is that semiconductors with wide bandgaps generate higher voltage.

In terms of efficiency, higher bandgap materials give a better open-circuit voltage V_{oc} and hence better energy conversion efficiency.

However not all those electrons with energy greater than the energy gap contribute to useful power. Instead some of the created electron-holes recombine with the states in the tail and midgap regions. The excess energy is lost as heat (thermalisation) and not only the electron -pair recombination but also the excess heat has a detrimental effect on the solar cell. Long hours of solar cell light exposure has been observed to produce a reversible degradation of electronic properties, which stabilize only at reduced levels. The phenomenon is known as Staebler –Wronski effect (SWE) [9]. This drawback of a-Si has been a subject of intense research in the last decades, even if to date its microscopic origin is still not well understood. However a large consensus has been reached that the SWE is accompanied by an increase of dangling bonds during illumination. Several models have been proposed to explain it, and efforts are invested in the deposition of a new class of material more stable and less affected by the SWE.

1.2. Aim and outline of this thesis

In this thesis, we want to deposit a nano-crystalline material using the Hot Wire Chemical Vapor Deposition (HWCVD) technique; it has been shown that amorphous films degrade to a great extent and stabilize only at reduced level, while microcrystalline films degrade very little but are not photosensitive [10]. The films in the transition region incorporating a finite volume fraction of crystals in an amorphous network are expected to have very low degradation accompanied with reasonably high values of photosensitivity and to keep good values of absorption coefficient due to its amorphous nature.

In the second chapter we give an overview on the hot wire technique: a short historical overview of the technique is given and keys issues pertaining to HWCVD are discussed.

The third chapter will give a comprehensive background on diverse analysis techniques used to characterize the samples.

Chapter four will focus on the deposition conditions, main results obtained and discussion.

The last part of this work consists of the main conclusions and recommendations.

Chapter 2. Hot-wire chemical vapour deposition

2.1. The HWCVD chambers

All the films described in this study have been deposited in the hot-wire CVD system, part of the solar energy research facility at the University of the Western Cape.
The system consists of two vacuum chambers: a load-lock and an ultrahigh vacuum (UHV) reaction chamber able to achieve pressures as low as 10^{-9} mbar. A detailed description of the chambers has been given by Arendse [11].

2.2. The HWCVD process

Hot-wire CVD was first introduced by Wiesmann [12] in 1979 when he succeeded to deposit a-Si:H by thermal decomposition of silane from a hot tungsten or carbon foil heated to about 1600° C. Unfornatunately due to very low gas pressures (1.33 x 10^{-6} – 1.33 x 10^{-4} mbar), he achieved too low deposition rates (0.6 – 8.7 Å / sec.) and films with low quality due to the poor vacuum used. The process itself and the nature of the produced species on the surface filament were not understood at that stage. Evidence of the catalytic nature of the decomposition has now been found: The 12.9 eV needed to pyrolytically cleave four Si-H bonds [13] is much higher than the activation energy of Si radical on the surface of the main wires used (Mo, Ta and W) of (2.6, 1.0, and 0.74 eV) respectively as reported by Tange *et al.*[14].
Later, in 1986 Matsumura [15] obtained high quality hydro- fluorinated a-Si (a-Si: F: H) and hydrogenated amorphous silicon (a-Si: H) by thermal and catalytic reactions between deposition-gas and a heated tungsten catalyzer. He named it “Catalytic – CVD (CTL – CVD)” method. A deposition rate larger than 20 Å / sec was achieved and more importantly, he reported that the magnitude of the SWE of the films produced seemed smaller than that of the glow discharge a-Si:H produced films.

J. Doyle *et al.* [16] using what they referred to as "evaporative surface decomposition (ESD) method" reported in 1988 a deposition of excellent a-Si:H film quality from silane decomposition with silane pressures ranging from 4 to 30 mTorr (~ 5 – 40 μbar).
They explained the deposition mechanism and postulated for the first time the nature of the radicals giving growth at the substrate surface. As actually agreed upon, they identified the 3 main phases of the deposition process:

1. The deposition of the feed gas on the hot surface of the wire.
2. The evaporation of the radicals and gas-phase collision (creation of secondary species).
3. Film growth on the substrate surface.

At the ~1700 *K* temperature where they were working, they noted that the decomposed silane gas was mostly atomized into H and Si atoms. A major fraction of the Si and H atoms is expected to arrive at the substrate without reacting, but a significant fraction may react to form other radicals. Hot hydrogen and silicon atoms which have not undergone the gas-phase collisions process were observed to dominate the radical flux to the hydrogen-passivated a-Si: H surface. They observed that the dominant species impinging on the substrate were SiH_4 and H_2. The reaction between SiH_4 and the surface dangling bond was postulated to give SH_3 and a passivated surface bond. Thus considerable SiH_3 , lesser SiH_2 and Si_2H_2 (which increase with the gas pressure) were expected to contribute to the deposition. J. Perrin *et al.*[17] has confirmed the nature of these radicals as exothermic gas phase reactions in the HWCVD:

$$H + SiH_4 \rightarrow SiH_3 + H_2 \qquad (2.1)$$

$$H + SiH_3 \rightarrow SiH_2 + H_2 \qquad (2.2)$$

$$SiH_3 + SiH_3 \rightarrow SiH_4 + SiH_2 \qquad (2.3)$$

$$Si + SiH_4 \rightarrow Si_2H_2 + H_2 \qquad (2.4)$$

$$Si_2H_2 + SiH_4 \rightarrow Si_3H_4 + H_2 \qquad (2.5)$$

In 1991, Mahan *et al.*[18] demonstrated for the first time the possibility to produce device-quality a-Si:H with reduced hydrogen content. Good quality films with less than 1 at. % hydrogen compared to 8-12 at. % contained in good quality a-Si: H obtained by

plasma enhanced CVD, confirmed that only a small quantity of hydrogen was needed to passivate the dangling bonds. Mahan and co-authors obtained thin films with photosensitivity $(\sigma_p / \sigma_d) \sim 10^5$ and Urbach edges (see Appendix 1) that, in contrast to PECVD films, did not broaden as the hydrogen content was reduced. After the work of Mahan, many groups worldwide took a keen interest in this Si-based new technology.

Efforts have been focused on the understanding of the decomposition process itself, the issues related to the growth and improvement of deposition rate and on the deposition of a new class of materials which is more stable and less sensitive to the SWE.

Among these, micro- and polycrystalline silicon have been the object of research in some groups.

Schropp [19] defines hydrogenated micro-crystalline silicon (μc-Si:H) as a material with two phases, amorphous and crystalline with crystal sizes lower than 20 nm, and hydrogenated poly-crystalline silicon as a material with a single phase crystalline with grain boundaries, the smallest crystal dimension must be larger than 20 nm.

Specific characteristic values of the main parameters (crystalline volume fraction V_f, the orientation of the grains, the band gap E_g, the photoconductivity σ_{ph}, the dark conductivity σ_d and activation energy E_a) give a clear cut distinction between both μc-Si:H and polycrystalline silicon on one hand, and between microcrystalline and amorphous silicon on the other hand.

As will be later seen in chapters 3 and 4, Raman spectrum analysis gives enough information on the phases of the deposited material. The crystalline volume fraction is calculated using

$$V_f = \frac{I_c}{I_c + mI_a} \tag{2.6}$$

where I_c and I_a are the deconvoluted intensities of the Raman spectra centered around 520 cm^{-1} and 480 cm^{-1} respectively.

m is a correction factor expressing the ratio of the cross section for the amorphous to the crystalline phase that varies with the grain size x as proposed by Bustarret [20]

$$m(x) = 0.1 + e^{-x/250} \tag{2.7}$$

when x is expressed in Å.
Amorphous materials will have obviously $V_f = 0$ since the 520 cm^{-1} band is absent in their Raman signal, and only a broad peak centered around 480 cm^{-1} is observed. The absence of this 480 cm^{-1} centered peak can be interpreted as the absence of amorphous tissue and the film to be fully polycrystalline.

2.3. Nanocrystalline silicon in HWCVD

It is actually agreed that the best quality amorphous material is found at the edge of crystallinity just before the threshold of crystallinity.
Thin silicon nanocrystalline films can be obtained in HWCVD by a good control of the deposition conditions. The amorphous to nanocrystalline transition can be achieved by increasing the hydrogen dilution in the SiH_4 feed gas [21-22], by increasing the substrate temperature [18,22], by varying the deposition pressure [23] and by varying the filament temperature [24].
Nanocrystalline silicon being a material grown at the edge of crystallinity, just above the threshold, it is believed to retain both benefits of the two phases that coexist in it. The incorporation of a finite amount of crystallites makes it more electronically stable than its amorphous counterpart; at the same time due to its amorphous nature, it retains good absorption characteristics of a-Si:H films and it has been reported to be reasonably photosensitive [10].
Its apparent energy gaps, as will be shown in our results, are higher (1.5-1.8 eV) than those of crystalline silicon (1.12 eV).
Much more research is however needed in this regime since the obtained films have inferior electronic quality compared to their a-Si: H counterparts as shown by the results of many groups [25].

2.4. Keys issues pertaining to the deposition process in HWCVD

2.4.1. Deposition rate (r_d)

This is a key parameter to control if one wants to produce a commercially cheap intrinsic material but at the same time preserve the electronic and structural properties of a device quality.

We will define in this thesis the deposition rate r_d as the ratio between the accumulated thickness and the time of deposition. The abundance of silane flow rate in the reaction chamber is a key element in order to achieve high deposition rates. If the gas flow rate is too low, the environment nearest to the filament will become depleted of silane [3]. As it has been shown previously by our group [11], the deposition rate increases almost linearly with the pressure in a certain range; this can be explained by the increase of the Si-containing radicals as the process pressure increases. Moreover Van Sark [2] has proposed a linear relation between the molecules impingement rate per unit area (r_i) at the filament and the pressure P as

$$r_i = \frac{P}{\sqrt{2\pi k_B T_g}} \tag{2.8}$$

where k_B is the Boltzman constant and T_g is the gas temperature.

Increasing the pressure further though will result in deposition rate saturation because the surface at the filament is limited and thus the saturation of the decomposition of the feed gas will result.

The growth rate is reduced with the increase in the hydrogen dilution as will be seen in our results, due mainly to the decrease of the SiH_4 pressure in the chamber as well as the etching effect of the hydrogen atoms known to etch away the weak Si-Si bonds [3].

It is evident that the hot wire temperature must be high enough to ensure efficient gas decomposition in order to achieve a high deposition rate.

Although progress has been made in increasing the deposition rate up to 16.5 Å/s with 9.8% active area device efficiency [26-27], much more work on the films grown at ultra-high deposition rates is still needed. It has been observed that increasing the deposition rate is accompanied with the lowering of the initial efficiency and the increase in the SWE [28].

Mahan *et al.* [27] recently however, in a twofold effort to get both high deposition and preserve good electrical and structural properties of the material, reported a series of films and devices deposited in the high silane depletion regime. They were able to achieve r_d as high as 100Å/s, keeping the Urbach edge E_0 slope as low as 55 mV and the void volume fraction (see Appendix 2) was found to saturate for $r_d > 40$ Å/s. This last finding allowed them to conclude that, since the weak bonds are linked to high E_0, the strained weak bonds shall be said to lie on or near the microvoid surfaces. The high density of atomic hydrogen in very high silane depletion regime was held responsible for the preservation of improved film quality at very high r_d.

2.4.2. The role of the filament

The role of the filament in HWCVD is mainly to decompose the gaseous molecules and to catalytically influence the reactions. Its temperature must be high enough to allow an efficient cracking of those molecules. Moreover the wire should be brought to a minimum critical temperature, otherwise silicon will react with the filament forming silicide on the surface. In this case the resistivity of the wire would change making impossible the reproducibility of deposition. Doyle *et al.* [16] have identified that minimum critical temperature as 1400° C for Tungsten.

Care must be taken to introduce a reducing gas such as H_2 in the chamber during filament heating in order to avoid its oxidation [29]. Since the melting point of an oxidized metal is lower than the intrinsic one, contamination of the film would occur from an oxidized filament.

Another precaution is be to reduce the thermal irradiation of the substrate from the filament. Although the real substrate temperature might not fluctuate extensively in case

of the substrate with large heat capacity, a shutter should be placed in front of it during filament heating and special thermocouples should be embedded inside in order to detect the discrepancy between the preset and real substrate temperature.

As stated by Matsumura *et al.* [29] the number of molecules colliding with the filament is proportional to the gas pressure and inversely proportional to the square root of the gas temperature while the rate of cracked molecules is dependent on the surface of the catalyser and on the chemical property of the adsorbed species. The activation energy is dependent on the catalyzing material.

2.4.3. The role of hydrogen dilution

Hydrogen dilution is one of the parameters that we have used in this study to induce crystallinity in the films.

The beneficial influence of hydrogen dilution is attributed to 3 mechanisms as proposed by Feenstra [3]:

1. In the presence of H_2 atoms, the surface passivation is more complete, resulting in a more homogeneous film growth.
2. With increasing H_2 dilution, the ratio [SiH_3] / [SiH_2] increases because hydrogen species will react with SiH_4 to form SiH_3.
3. The hydrogen radicals are known to etch away weak Si-Si bonds in the subsurface region promoting the growth of a dense, high-quality material.

Very high dilutions however are not recommended since they are accompanied with a change of the crystals preferential orientation as will be shown by our XRD results and as previously observed by other groups [22,30,31].

Another drawback observed in the very high hydrogen dilution regime is the decrease of the deposition rate. This is explained by the depletion of the SiH_4 in the chamber resulting in less species decomposed on the filament for film growth. Moreover the increase of H_2 in the chamber give rise to the concentration of atomic hydrogen decomposed from the wire that in its turn will increase the etching effect on the growing surface.

2.4.4. Influence of pressure

Another parameter of importance that influences both growth and properties of the material is the gas flow pressure.

As will be seen in the results-chapter, the gas pressure influences the deposition rate r_d. In general the deposition rate increases with increasing the gas pressure [32]. In an extensive study, Feenstra [3] distinguishes between two regimes of low and high pressures. In the low-pressure case, the mean free path (λ_{mfp}) of the decomposed species is large and they arrive on the surface of the substrate without secondary reactions. It is observed that the deposition rate is directly proportional to the pressure. If the gas pressure is increased, the λ_{mfp} decreases and the increase in the number of reactions slows the transport of the precursors from the filament to the substrate: a subsequent decrease in r_d is observed and the species contributing to the growth are different. At low pressure the main growth precursor is Si and due to its high sticking coefficient it will give rise to growth of a void rich material.

SiH_3 species are some of the radicals generated in gas phase reactions between SiH_4 and H previously produced at the wire from SiH_4 decomposition. Since SiH_3 has a high reaction probability and is more mobile [33], it will react with the growing surface and move to a better energetic position before contributing to the film growth. This fact results in both a deposition rate decrease and in the improvement of the material quality.

It is obvious that the distance between the filament and the substrate (compared to λ_{mfp}) plays a big role in the deposition process and in the microstructure of the films since it will determine the number of precursors arriving on the growing film without gas reactions.

2.4.5. Incorporation of hydrogen

Hydrogen incorporation in the films plays an important role in the properties of both amorphous and microcrystalline silicon.

Indeed the hydrogen content has been linked to the metastability change upon light exposure [34-36] and its bonding configuration has been reported to influence the structural properties in the material [37].

The study of S. M. Pietruszko *et al.* [34] has shown that higher hydrogen concentration causes greater metastable changes but shorter relaxation times.

Considering the weak Si-Si breaking bonds model [4] and taking into account that the network is stressed in the vicinity of Si-H bonds, two dangling bonds are created at each Si-Si broken bond resulting in the increase of the defect density.

Pen *et al.* [38] had in an earlier glow discharge study linked the hydrogen content to the widening of the energy gap.

Ouwens [37] explained that hydrogen alloying increased the band gap of a-Si since the Si-H bonds are stronger than Si-Si ones thus absorbing at higher energies.

Several studies have concluded that the hydrogen content in a-Si:H films was strongly dependent on the deposition temperature [3,39,40].

P.V. Santos *et al.* [39] in their hydrogen density-of-states model suggest that hydrogen is trapped in shallow (bond-centre and interstitial sites) and deep traps (dangling bond sites).

The chemical potential of hydrogen is given by [3]:

$$\mu_H = E_t + k\, T_{sub.} \ln \frac{N_H}{N_t - N_H} \qquad (2.9)$$

where μ_H is the hydrogen chemical potential;

E_t the energy level of deep traps and

N_t, N_H are the deep trap density and occupied deep trap density respectively.

Since μ_H in the gas phase must be equal to the hydrogen chemical potential in the solid phase (film), which obviously increases with the substrate temperature, according to the above equation the occupancy of the deep traps N_H must be lowered to keep the two components of the equation equal. This explains why the hydrogen content is reduced as the temperature of the substrate is increased.

Chapter 3. Analysis techniques

3.1. Optical Characterization

3.1.1. Optical Absorption and Energy Gap

When light impinges on a semiconductor, the photons of energy $h\nu \geq E_g$ are absorbed while those of energy less than the bandgap are transmitted.
The ratio of the transmitted and the incident light is a function of both the photon wavelength and the thickness traveled. Lambert's law states that the proportion of the radiation absorbed by a substance is independent of the incident radiation but instead the relative loss of intensity is proportional to the traveled thickness dx according [41]

$$-\frac{dI(x)}{I(x)} = \alpha\, dx \qquad (3.1)$$

The differential equation has as solution

$$I(x) = I_0 e^{-\alpha x} \qquad (3.2)$$

where I_0 is the intensity of the incident beam (at position $x = 0$) and α the absorption coefficient in cm^{-1}.
The measured transmission T is given by:

$$T = \frac{I}{I_0} \qquad (3.3)$$

It is related to another expression *absorbance (A)* frequently used in the literature by [41]

$$A = log_{10}\frac{1}{T} \quad (3.4)$$

The equations (3.2); (3.3) and (3.4) combined allow to relate the absorption coefficient to the absorbance by

$$\alpha = \frac{A \ln 10}{d} \approx \frac{2.303 A}{d} \quad (3.5)$$

where d is the sample thickness.

The plot of α vs. wavelength gives a good estimation of the E_g at the abscissa of the inflection point.

The photon energy $h\nu$ is related to the wavelength as

$$E = h\nu = \frac{hc}{\lambda} = 1240/\lambda \quad (3.6)$$

with E in eV and λ in nm

For a practical determination of E_g, Tauc [42] (assuming that the density of states near the band edges have a parabolic shape) has suggested the relation

$$(n\alpha h\nu)^{1/2} = B\,(h\nu - E_g) \quad (3.7)$$

Klazes *et al.* [43] (assuming a linear shape) proposed a similar relation where the square root is replaced by a cubic one with different constants in the second part of the equation;

$$(n\alpha h\nu)^{1/3} = B'\,(h\nu - E_g) \quad (3.8)$$

The plot of the first part of the equations vs. the photon energy ($h\nu$) and the extrapolation of the linear part give the E_g at the intercept with the E-axis.

The value found using the cubic-plot is generally lower by about 0.2 eV than the one calculated using the Tauc-plot.

The fit procedure, unfortunately, varies from one experimentator to the other and can sometimes lead to large uncertainties, which is the reason why some authors prefer to use $E_{opt.}$ corresponding to the absorption coefficient value of 10^4 cm^{-1}, referred to as E_{04}. [44]

3.1.2. Experimental determination of the refractive index and thickness

3.1.2.1. Case of film with uniform thickness

For the experimental determination, we have used a method proposed by Swanepoel [45] where the optical functions of a uniform film deposited on a transparent substrate are determined from the transmission spectrum $T(\lambda)$ obtained from a UV-visible spectrophotometer. We give in the following paragraphs important optical relations developed by Swanepoel under certain assumptions, as they constitute the theoretical basis of the numerical determination of the optical parameters used in this thesis.
The optical response of amorphous silicon is expressed as follows in terms of the refractive index n and the extinction coefficient k.

$$\tilde{n}(\lambda) = n(\lambda) - ik(\lambda) \tag{3.9}$$

When considering a uniform homogeneous film with thickness d and optical functions $n(\lambda)$ and $k_1(\lambda)$ on a transparent ($k_2 = 0$) thick substrate with refractive index $s(\lambda)$ (Corning glass in our experiment), no coherent multiple reflections take place in the substrate and the amorphous film alone is responsible for an interference pattern spectrum T expressed as follows: [46]

$$T = \frac{Ax}{B - Cx\cos\varphi + Dx^2} \tag{3.10}$$

where $A = 16n^2 s$ (3.11)

$$B = (n+1)^3 (n+s^2) \tag{3.12}$$

$$C = 2(n^2-1)(n^2-s^2) \tag{3.13}$$

$$D = (n-1)^3 (n-s^2) \tag{3.14}$$

$$\varphi = \frac{4\pi nd}{\lambda} \tag{3.15}$$

$$\alpha = \frac{4\pi k_1}{\lambda} \tag{3.16}$$

$$x = exp(-\alpha d) \tag{3.17}$$

A typical transmission spectrum for amorphous silicon of about 1 µm thick is shown in fig. 3.1.

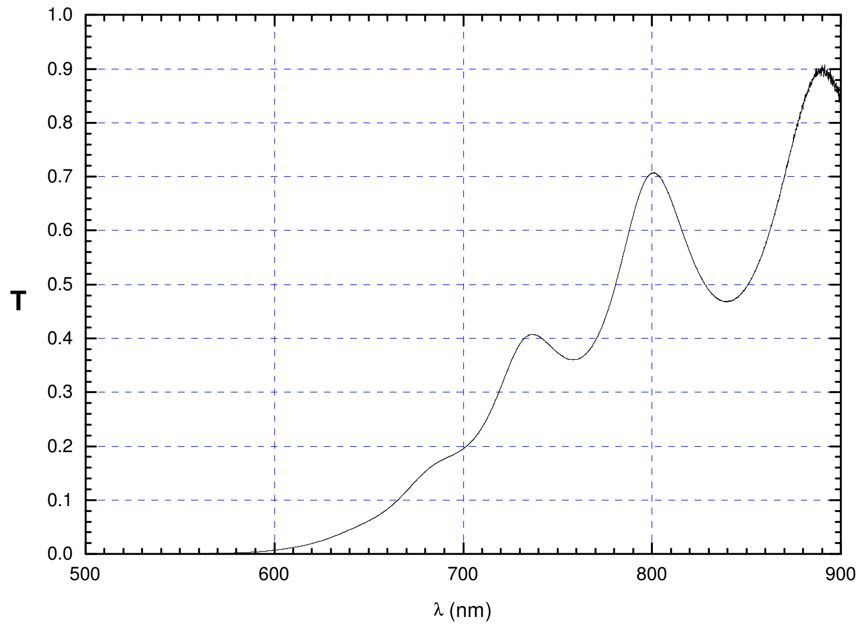

Figure 3.1. Transmission spectrum of a film grown at 20 µbar with 90% hydrogen dilution and a substrate heater temperature of 450°C.

Assuming $\cos\varphi = +1$ equation (3.10) becomes

$$T_M = \frac{Ax}{B - Cx + Dx^2} \tag{3.18}$$

In the case of $\cos\varphi = -1$, equation (3.10) becomes

$$T_m = \frac{Ax}{B + Cx + Dx^2} \tag{3.19}$$

(3.18) and (3.19) are found from the 2 given boundary conditions representing the equations of smoothed envelopes around the transmission spectrum.
$\cos\varphi = 1$ implies from (3.15)

$$\frac{4\pi nd}{\lambda} = m \times 2\pi \Leftrightarrow 2nd = m\lambda \tag{3.20}$$

where $m = 0,1,2,3\ldots$
and $\cos\varphi = -1$ implies from (3.15)

$$\frac{4\pi nd}{\lambda} = m' \times 2\pi \tag{3.21}$$

where $m' = 1/2, 3/2, 5/2, 7/2, \ldots$

The combination of (3.20) and (3.21) gives a relation between the refractive index and the thickness, known as the interferometric equation

$$2nd = m\lambda_e \tag{3.22}$$

λ_e are the wavelengths at the extrema and m = 0; 1/2; 1; 3/2; 2; 5/2..integer at the maxima (from the equation (3.20)) and half integer at the minima (from the equation (3.21)).

The quantity x (given by the relation 3.17), known as the absorption, has values between 0 and 1. Solving the expression (3.10) for x yields a useful equation for the absorption

$$x = \left(\frac{A/T - C\cos\varphi}{2D}\right) \mp \left[\left(\frac{A/T - C\cos\varphi}{2D}\right)^2 - \frac{B}{D}\right]^{1/2} . \qquad (3.23)$$

Eliminating x from T_M and T_m expressions, one deduces on the other hand the expression of the refractive index n for a film with uniform thickness

$$n = \{N + (N^2 - s^2)^{1/2}\}^{1/2} \qquad (3.24)$$

where $N = 2s(\frac{T_M - T_m}{T_M T_m}) + (s^2+1)/2$ (3.25)

In the case of a transparent film for which $\alpha = 0$ (x=1), equations (3.18) and (3.19) become

$$T_M = \frac{2s}{s^2+1} \text{ and } T_m = \frac{4n^2 s}{n^4 + n(s^2+1) + s^2} . \qquad (3.26)$$

T_M coincides then with the transmission of the substrate alone because it is only a function of s.

Since s is known for a glass substrate, T_M and T_m are read from the transmission spectrum, the refractive index of the film is calculated. Subsequently the thickness d is determined from the interferometric equation (3.22).

3.1.2.2. Case of film with non uniform thickness

The formulae in the previous section were deduced assuming that the film thickness was uniform. If there is a variation in thickness, Δd, the amplitude of the interference pattern shrinks and the procedure is not as accurate any more. When calculations are carried out as if the film was uniform, this leads to the absorption band tail in the long-wavelength region (see fig.3.2 where an apparent absorption starting from the long –wavelength is observed) and serious errors occurred in the obtained values of n, d and α.
This shrinking can be corrected for however and Δd can be determined or a uniform film with same average thickness can be postulated [45].

Two equations with 5 unknowns (Δd, n, $\bar{d}$, x and m) are deduced from (3.10) and (3.22) given the new circumstances where the thickness d varies from the average thickness $\bar{d}$ as $d = \bar{d} \pm \Delta d$:
$T = T(\Delta d, n, \bar{d}, x)$ and
$2n\bar{d} = m\lambda$
Different regimes must be then considered and doing so one makes appropriate approximations leading to supplementary equations.

3.1.2.2.1. In the transparent region

In the transparent region the absorption is zero, thus $\alpha = 0$ ($x = 1$).
Equation (3.10) becomes

$$T = \frac{A}{B - C\cos\varphi + D} \quad (3.27)$$

φ being dependent of the thickness d that varies between
$\bar{d} - \Delta d$ and $\bar{d} + \Delta d$, one shall proceed to an integration of T between the boundaries

$\varphi_1 = 4\pi n(\bar{d} - \Delta d)/\lambda$ and $\varphi_2 = 4\pi n(\bar{d} + \Delta d)/\lambda$

The integration yields to [45]

$$T_{\Delta d} = \frac{\lambda}{4\pi n\Delta d}\frac{a}{(1-b^2)^{1/2}} \text{ x } \left[\tan^{-1}\left(\frac{(1+b)}{(1-b^2)^{1/2}}\tan\frac{\varphi_2}{2}\right) - \tan^{-1}\left(\frac{(1+b)}{(1-b^2)^{1/2}}\tan\frac{\varphi_1}{2}\right)\right] \quad (3.28)$$

where $a = \dfrac{A}{B+D}$ and $b = \dfrac{C}{B+D}$. (3.29)

Using the trigonometric relation $\tan(u+v) = \dfrac{\tan u + \tan v}{1 - \tan u \tan v}$, we can write

$$\tan \varphi_2/2 = \frac{\tan(2\pi n\bar{d}/\lambda) + \tan(2\pi n\Delta d/\lambda)}{1 - \tan(2\pi n\bar{d}/\lambda)\tan(2\pi n\Delta d/\lambda)} \quad (3.30)$$

The condition of maximum in equation (3.10) requires that $\cos\varphi = 1$ ($\sin\varphi = 0$) i.e.

$$\frac{4\pi nd}{\lambda} = l \times 2\pi \Rightarrow \frac{2\pi n\bar{d}}{\lambda} = l\pi$$

Where $l = 0,1,2,3,$ ..and thus $\tan(2\pi n\bar{d}/\lambda) = 0$

The equation (3.30) reduces then to

$$\tan(\varphi_2/2) = \tan\left(\frac{2\pi n\Delta d}{\lambda}\right) \quad (3.31)$$

Similarly and considering $\tan(-u) = -\tan(u)$

$$\tan(\varphi_1/2) = -\tan\left(\frac{2\pi n\Delta d}{\lambda}\right) \quad (3.32)$$

Substituting the 2 last expressions in equation (3.28), we get

$$T_{Md} = \frac{\lambda}{2\pi n\Delta d}\,\frac{a}{(1-b^2)^{1/2}}\,tan^{-1}\left[\frac{(1+b)}{(1-b^2)^{1/2}}\tan\left(\frac{2\pi n\Delta d}{\lambda}\right)\right] \qquad (3.33)$$

The condition of minimum in equation (3.10) requires cosφ = -1 which is equivalent to apply the same reasoning as above for the condition of maximum but the sign of C in equation (3.10) must be changed, and also for b in equation (3.29), since they are directly proportional. The following expression has been obtained by Swanepoel [45]

$$T_{md} = \frac{\lambda}{2\pi n\Delta d}\,\frac{a}{(1-b^2)^{1/2}}\tan^{-1}\left[\frac{(1-b)}{(1-b^2)^{1/2}}\tan\left(\frac{2\pi n\Delta d}{\lambda}\right)\right] \qquad (3.34)$$

It is clearly seen that the two previous equations are independent of $\bar{d}$ and are only function of Δd and n; this can physically be interpreted that the transmission spectra for films with the same variation in thickness lie between 2 same envelopes (T_{Md} & T_{md}) even if they have different thicknesses i.e. a thick sample will be found between the same envelopes as a thin one as long as they have the same variation in thickness Δd. The only difference will be that closer spaced fringes of interference are observed for the thicker sample.

The two equations can then be used to accurately determine Δd in the transparent region. The tangent factor in equation (3.34) allows to define the range of validity as $0<\Delta d<\frac{\lambda}{4n}$.

The physical meaning of this condition is the merging of the curves (3.28), (3.33) and (3.34) or the disappearance of the interference pattern at $\Delta d = \lambda / 4n$. Swanepoel had previously shown that this point is related to T_M and T_m by [46]

$$T_\alpha = (T_M\, T_m)^{1/2} \qquad (3.35)$$

As illustrated by fig.3.2, one cannot tell by the observation of a non-uniform film spectrum about the onset of absorption while for a uniform film, the departure of T_M from the substrate transmission means the threshold of absorption. As it can be seen from the graph, for a non-uniform thickness film T_{Md} approaches T_s only for long wavelengths and decreases consistently with decreasing λ, even if there is no absorption by the layer.

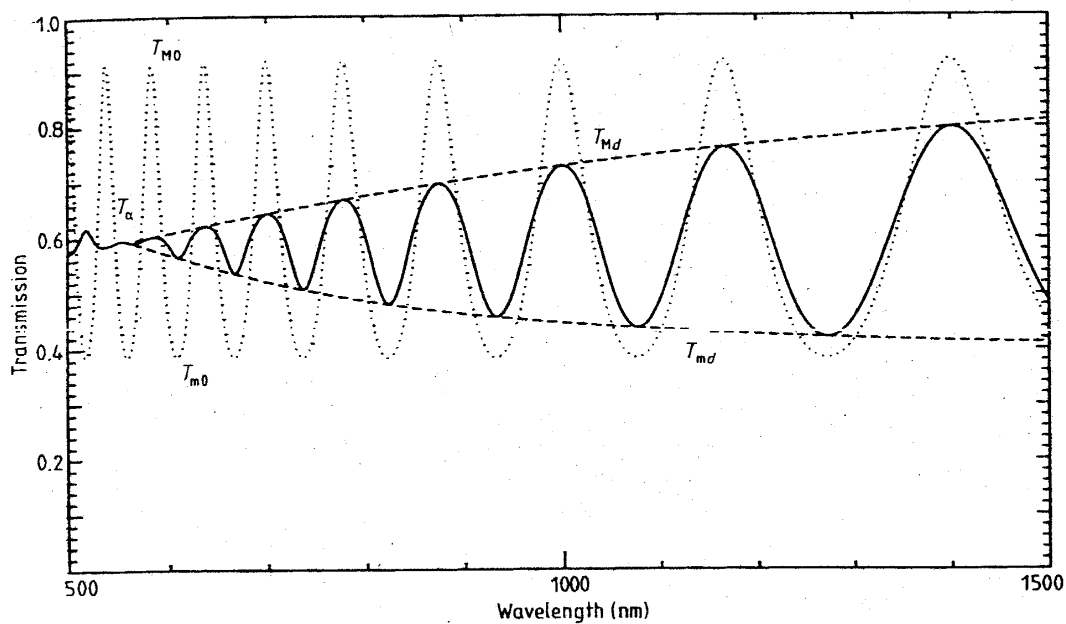

Figure 3.2. Simulated transmission for a transparent film with uniform thickness (dotted- curve spectrum) compared to that of a film with a thickness variation Δd = 40 nm (full-curve spectrum). [45]

It can be noticed as well from the figure above that the minima around the spectrum of a sample of non uniform thickness have an upward trend with decreasing λ, contrary to the opposite trend for the one of a uniform film as shown in fig. 3.3.

3.1.2.2.2. In the region of weak and medium absorption

This region corresponds to α>0 and the integration of T should be done over both Δd and x;

With the assumption that $\Delta d << \bar{d}$, the equations for the 2 envelopes become [45]

$$T_{Mx} = \frac{\lambda}{2\pi n \Delta d} \frac{a_x}{(1-b_x^2)^{1/2}} \text{ x } \tan^{-1}\left[\frac{(1+b_x)}{(1-b_x^2)^{1/2}} \tan\left(\frac{2\pi n \Delta d}{\lambda}\right)\right] \tag{3.36}$$

$$T_{mx} = \frac{\lambda}{2\pi n \Delta d} \frac{a_x}{(1-b_x^2)^{1/2}} \text{ x } \tan^{-1}\left[\frac{(1-b_x)}{(1-b_x^2)^{1/2}} \tan\left(\frac{2\pi n \Delta d}{\lambda}\right)\right] \tag{3.37}$$

where $a_x = \dfrac{Ax}{B+Dx^2}$; $b_x = \dfrac{Cx}{B+Dx^2}$; and $x = \exp(-\alpha\bar{d})$ (3.38)

The equations (3.36) and (3.37) contain only two unknowns n and x since Δd is known from the previous regime. They have one unique solution in the range $0 < x \leq 1$.

The obtained values of n are best fitted to an equation of the form [45]

$$n = \frac{d}{\lambda^2} + n_0 , \tag{3.39}$$

and n_0 is the value of n extrapolated at 0 eV.

3.1.2.2.3. In the region of strong absorption

This is the case where T, T_{Md} and T_{md} merge into a single curve. The spectrum approaches the interference- free transmission given by the relation (3.35) $(T_\alpha = (T_M T_m)^{1/2})$ and the same procedure can be used as in the case of film with uniform thickness.

Equations (3.18) and (3.19) are then valid and can be solved for x

$$x = \frac{A - (A^2 - (A^2 - 4T_i^2 BD)^{1/2}}{2T_i D} \tag{3.40}$$

Where $T_i = \dfrac{2T_M T_m}{T_M + T_m}$ (3.41)

Equation (3.40) can be used to calculate x in the region of strong absorption and (3.39) will be used to obtain n.

3.1.2.3. Relation with the spectrum of a uniform thickness

The rearrangement of equations (3.36) and (3.37) gives [45]

$$T_M' = \frac{(T_M T_m)^{1/2}}{\theta} \tan^{-1}\left[\left(\frac{T_M}{T_m}\right)^{1/2} \tan\theta\right] \tag{3.42}$$

$$T_m' = \frac{(T_M T_m)^{1/2}}{\theta} \tan^{-1}\left[\left(\frac{T_m}{T_M}\right)^{1/2} \tan\theta\right] \tag{3.43}$$

where $\theta = \dfrac{2\pi n \Delta d}{\lambda}$ (3.44)

and the range of validity for θ is between 0 and $\pi/2$.

Equations expressed in (3.42) & (3.43) are function of T_M, T_m and θ. In the transparent region, T_M is known since it corresponds to the substrate transmission $T_S = \dfrac{2s}{s^2+1}$.

The remaining unknowns in the transmission region are then T_m and θ and can be solved for. Once T_m is found, n can be calculated from equation (3.26) and Δd from (3.44).

There is however an alternative way to extrapolate the information obtained from the transparent region to the absorption one:

Swanepoel proposed that the interferometric equation could be written for successive extrema starting from the long wavelength [46]:

$$\frac{l}{2} = \frac{2n\bar{d}}{\lambda} - m_1 \qquad l = 0,1,2,3\ldots \qquad (3.45)$$

m_1 is the order number of the first extremum considered on the transmission spectrum. Equation (3.44) combined with (3.45) gives

$$\frac{l}{2} = \left(\frac{\bar{d}}{\pi\Delta d}\right)\theta - m_1 \qquad (3.46)$$

If $l/2$ is plotted against θ (more conveniently against $1000/\lambda$ as was used in our calculations), a best linear fit through the first few points of the transparent region allows to extrapolate, at λ infinity, the value of the order number of the first extremum considered (the absolute value of the intercept with the $l/2$ axis); it is an integer for a maximum and half integer for a minimum as already seen in section 3.1.2.1. The deviation of the straight line from the points corresponding to higher values of $1000 / \lambda$ has to be interpreted physically as the onset of absorption. They should be ignored in the fitting procedure.

The calculated slope of the fit and the equation (3.46) above allow the calculation of θ; T_M and T_m (maxima and minima of the generated spectrum corresponding to a film assumed to be uniform in thickness) can be calculated from (3.42) & (3.43) using the read values where the envelopes are tangent to the spectrum i.e. T_M' and T_m' as visualized in fig.3.3.

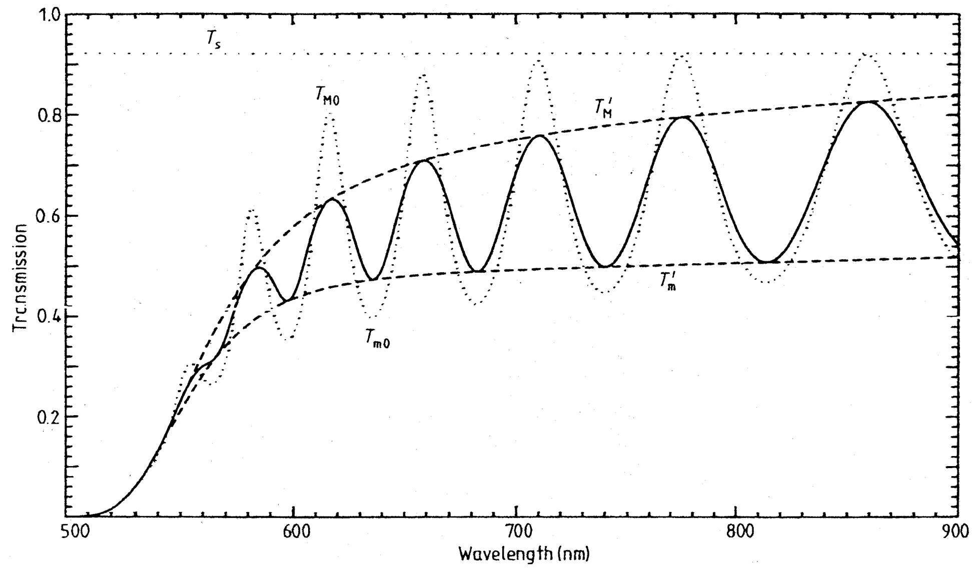

Figure 3.3. Simulated transmission for an absorbing film with uniform thickness of 1 µm (dotted-curve spectrum) compared to that of a film with a thickness variation Δd = 30 nm (full-curve spectrum). [45]

When T_M and T_m of the assumed uniform film are known, the procedures to obtain optical constants ($\bar{d}$, $n(\lambda)$ and $\alpha(\lambda)$) for a uniform film as previously discussed in section 3.1.2.1. can now be applied.

3.2. X-rays Diffraction characterization

*3.2.*1. Electromagnetic radiation

X-rays are electromagnetic radiation of exactly the same nature as light but of very much shorter wavelength [47]. They are ranging from 0.05 to 0.25 nm; Cu $K_{\alpha 1}$ with λ = 0.145 nm were used in our experiment.

Due to its wave nature, an X-rays beam carries energy and the rate of this energy per unit area is referred to as intensity I.
The average value of the intensity is proportional to the square of the amplitude of the wave carrier (A^2)·
Referring on the other hand to its particle nature, the energy carried by the X-rays radiation is proportional to the frequency, each photon energy being equivalent to $h\nu$, where h is the Planck's constant.

3.2.2. Absorption of X-rays

When X-rays penetrate the material of the film on a substrate, part of the energy is transmitted and another part is absorbed (included the scattered beam since they do not appear in the transmitted beam).
The decrease in the intensity as the X-rays passes through a distance x in the film is given by

$$-\frac{dI}{I} = \mu \; \mathrm{d}x \qquad (3.47)$$

where the proportionality constant μ is known as the linear absorption coefficient.
A simple integration of the previous equation gives

$$I_x = I_0 \, e^{-\mu x} \qquad (3.48)$$

where I_0 is the intensity of the incoming X-rays and I_x the X-rays intensity after traveling a thickness x into the film.
The equation above can be expressed as a function of the density of the material as follows

$$I_x = I_0 \, \mathrm{e}^{-(\mu/\rho)\, \rho x} \qquad (3.49)$$

The quantity μ/ρ known as the mass absorption coefficient is tabulated [47].

For Silicon (ρ = 2.33 gm/cm^3) upon Cu K_α line with wavelength 1.542 Å used in our experiment, the mass absorption has a value of 65.32 cm^2/gm.

In case of chemical compounds, mixtures or solutions independently of the phase state μ / ρ is given by [47]

$$\frac{\mu}{\rho} = w_1 \left(\frac{\mu}{\rho}\right)_1 + w_2 \left(\frac{\mu}{\rho}\right)_2 + \ldots \tag{3.50}$$

w_1, w_2 ,.. are the weight fractions of the different constituent elements in the compounds, mixture or solutions.

3.2.3. Depth of X-Rays Penetration

The accurate analysis of X-rays spectra requires the knowledge of the depth penetration of the beam especially when the collected spectrum includes the signal of the substrate. It is observed experimentally that the intensity of the incident beam does not become suddenly zero but decreases exponentially with distance below the surface.

The fraction G_x of the total diffracted intensity which is contributed by a layer of depth x for symmetric diffraction at an angle θ to the surface is [47]

$$G_x = (1 - e^{-2\mu x/\sin\theta}). \tag{3.51}$$

The penetration depth is then given by

$$x = \frac{k_x \sin\theta}{2\mu} \tag{3.52}$$

where $k_x = ln\left(\frac{1}{1-G_x}\right)$

It is seen from the above formula that the effective depth of X-rays penetration decreases as θ decreases.

3.2.4. Diffraction of X- rays

From the theory of constructive interference, it is known that diffraction happens when the wavelength of the light is of the same order as the path difference between the scattering centers. The condition is mathematically well known as the Bragg equation:

$$n\lambda = 2d\,sin\theta \qquad (3.53)$$

Where n = 1; 2; 3; …

λ is the x-rays wavelength

d is the repeat distance between the lattice planes

θ is the Bragg angle (angle of incidence)

If B is defined as the width at an intensity level equal to the half maximum (*fwhm*) of the diffracted peak, then

$$B = \frac{1}{2}(2\theta_1 - 2\theta_2) \qquad (3.54)$$

where $2\theta_1$ and $2\theta_2$ are 2 successive angular positions in units of 2θ where the peak intensity is zero, the Scherrer formula is given [47]

$$t = \frac{0.9\lambda}{B\cos\theta_B} \qquad (3.55)$$

where θ_B is the Bragg angle and the calculated t value is an estimation of the crystal size. It is clear from the above formula that bigger crystals yield smaller diffracted beam widths. It should be noted that the formula only applies if the peak broadening is large

compared to the instrumental width. The instrument used in our experiments has a width of about 0.1° so that the crystallites need to be less than 80 nm in the direction of the scattering vector (usually normal to the surface).
The Bragg condition is not completely fulfilled in liquids or in amorphous solids due to lack of long range order. The amorphous phase is characterized by one or 2 broad peaks. This contrasts with XRD spectra in crystals where sharp peaks are observed due to positive interference originating from scattering from regularly spaced atoms. Indeed the amplitude of the contributing waves add in the case of positive interference yielding $(nA)^2$ as intensity value from n scattering centres, while we have only nA^2 for randomly oriented scattering centres.

3.3. Raman Spectroscopy

3.3.1.Theoretical background

When light is incident on a sample, most of the light is elastically scattered in random directions (the total kinetic energy before collision K_1 = the total kinetic energy after collision K_2); this phenomenon is known as Rayleigh scattering.
The small remaining (or missing) fraction of the light is inelastically scattered; the phenomenon is known as Raman scattering (An illustrative example is displayed in appendix 3 for amorphous silicon). The resulting energy levels in the illuminated sample may be higher or lower than the energy level of the initial state of the electrons. Roughly speaking the inelastically scattered light has a wavelength higher or lower than the one of the incident light. The difference in energy is due to rotational and vibrational transitions in the material target. This shift in photon energy corresponds to the energy of phonons that have been created or annihilated [41]. During Raman scattering, both energy and momentum are conserved (fig.3.4.):

$$E_{\text{incident}} = E_{\text{Raman}} + E_{\text{phonon}} \tag{3.56}$$

$$\boldsymbol{k}_{\text{incident}} = \boldsymbol{k}_{\text{Raman}} + \boldsymbol{k}_{\text{phonon}} \tag{3.57}$$

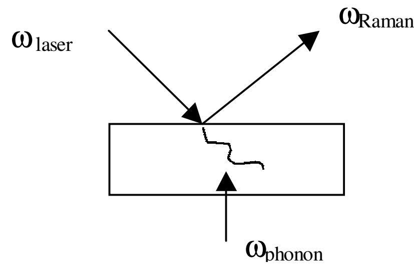

Figure 3.4. Energy and momentum conservation during Raman scattering

When the photon loses energy into the creation of a phonon, it is said to be Stokes scattered, and when it gains energy from the annihilation of a phonon it is said to be anti-Stokes scattered. Figure 3.5 illustrates the processes involved in both Rayleigh and Raman scattering:

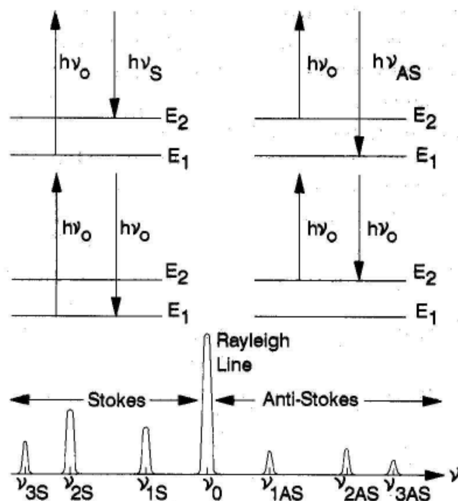

Figure 3.5. Processes involved in Rayleigh and Raman scattering and the production of Stokes and anti- Stokes lines. [48]

The Stokes lines are more likely to be observed because they are more intense. The ratio between the Stokes and anti-Stokes intensities is given by the Bose-Einstein statistics as

$$\frac{I_s}{I_{a-s}} = \left(\frac{\omega_{phonon} - \omega_0}{\omega_{phonon} + \omega_0}\right)^2 \exp\left(\frac{hc\omega_{phonon}}{kT}\right) \qquad (3.58)$$

Different Raman signals may be observed if there are more than one vibration or rotational degrees of freedom in the sample. To be active in the Raman spectrum, a vibration must produce an oscillating polarizability α [41]. The phenomenon is different in infrared spectroscopy where a vibration must produce an oscillating dipole. The polarizability is caused by an oscillating electric field $\boldsymbol{E}$ in the electromagnetic radiation; it causes a distortion in the shape of the molecule, the negative pole of the field attracts the positively charged nucleus while the negatively charged electrons are attracted to the positive pole. It can be intuitively understood that polarizability is a measure of the effectiveness of the electric field in disturbing the electron clouds.
We can express it mathematically as following [41]:

$$\boldsymbol{\mu} = \alpha \boldsymbol{E} \qquad (3.59)$$

μ is the induced dipole and α the polarisability.
From equation (3.56), it is seen that the observed frequency shifts correspond to the vibrational excitations of the molecules in the sample under investigations. This small signal can be detected by extremely sophisticated spectrometers and used to probe into the properties of the material such as phase state, degree of crystallinity, and crystal size among others.

3.3.2. Application on thin films

The Raman scattered wave is characteristic of the solid and independent of the incident light frequency; the main features associated with this phenomenon in thin films based on silicon are expressed in terms of the transverse optical mode (*TO*) of amorphous silicon centred around 480 cm^{-1} and the *TO* mode of crystalline silicon centred at 520 cm^{-1}. A shoulder is furthermore observed at around 510 cm^{-1}, it corresponds to a distribution of small crystallites or grain boundaries in the material. [49]
The crystalline fraction is calculated using the formula proposed by Brogueira *et al.* [50]

$$V_f = \frac{A_{510} + A_{520}}{A_{480} + A_{510} + A_{520}} \tag{3.60}$$

where A_{480}, A_{510} and A_{520} are the areas under the respective deconvoluted gaussians.

The *FWHM* of the 480 cm^{-1} centred *TO* peak is a measure of bond angle distribution and therefore allows a quantitative measure of disorder in the film [51].
S.R. Jadkar *et al.* [51] have found that as the structural disorder in the material increases this *TO* peak shifts to lower frequencies and both the Γ_{TO} *(FWHM)* and bond angle ($\Delta\theta$) increase. This is in agreement with theoretical studies, which indicate a linear relation between $\Gamma/2$ and the average bond angle variation $\Delta\theta$ in the amorphous network [52-53]. The last named authors have found that the linewidth (Γ) of the “optic peak” in cm^{-1} and the bond angle deviation $\Delta\theta_b$ are related by

$$\Gamma = 15 + 6\,\Delta\theta_b \tag{3.61}$$

The reported values of $\Delta\theta$, depending of the model used for calculations, vary between 4.4-8.2° and 11-14.1° for maximally ordered and maximally disordered networks respectively. [52]

3.4. Fourier transform infrared spectroscopy

3.4.1. Fundamentals

The method involves the passage of a long wavelength infrared beam through a film, which is deposited on a substrate supposed to be at least partially transparent to infrared light. In our case the samples in study were deposited on a c-Si substrate.
The transmitted signal intensity through a depth *l* is given by [54]

$$\frac{I_0}{I_t} = \exp\,[-kcl] \qquad (3.62)$$

I_0 is the intensity of the incident light on the sample; k the absorption coefficient that is the imaginary part of the complex function refractive index $\tilde{n}$ and c is the concentration of the absorbing material and $\frac{I_0}{I_t}$ is known as the transmittance T.

In the linear form, we have

$$log_{10}\left(\frac{I_t}{I_0}\right) = \varepsilon c l \qquad (3.63)$$

where $\varepsilon = \frac{k}{\ln 10}$ is known as the absorption cross-section and $log_{10}\left(\frac{I_t}{I_0}\right)$ (or $log_{10}\left(\frac{1}{T}\right)$) is defined as the absorbance.

For the quantitative analysis, we have measured the transmittance of a bare c-Si substrate and the transmittance for a film on a similar substrate. The transmittance of the thin film was given by the ratio between the transmittance spectrum of the film on the substrate divided by the transmittance spectrum of the bare substrate.

3.4.2. Hydrogen content and bonding in hydrogenated silicon

As known, pure amorphous silicon has a high density of unterminated silicon bonds known as dangling bonds [55-56].

These dangling bonds create a number of defect densities in the forbidden gap that can amount up to 10^{20} cm^{-3}. Such defects degrade the electronic properties of the material upon long hours of illumination because they act as traps and recombination centres and the recombination energy may create additional dangling bonds (SWE).

The incorporation of hydrogen in the amorphous silicon is beneficial because those dangling bonds are passivated. The infrared absorption spectrum provides a good tool to quantify and assess the nature of the Si-H bonds. In molecular vibration theory, it is convenient to visualize the atoms as rigid spheres connected by springs. The frequency of vibration of the two atoms can be given by applying Hookes's law for elastic expansion[48]:

$$\nu = \frac{1}{2\pi c}[\frac{F_c}{M_0}]^{1/2} \tag{3.64}$$

where c is the speed of light, F_c is the force constant of the oscillating bond in the atom and M_0 is the reduced mass of the system given by

$$M_0 = \frac{M_1 M_2}{M_1 + M_2} \tag{3.65}$$

where M_1, M_2 are the mass of the two atoms namely silicon and hydrogen here. The vibrational frequencies are in the order of the probing infrared light and different modes of vibrations are induced into the molecule. We recall here different modes of vibration observed in complex molecules; The vibrations in the direction of the bond are referred to as stretching modes while those normal to the bond are known as bending or deformation vibrations (see fig. 3.6):

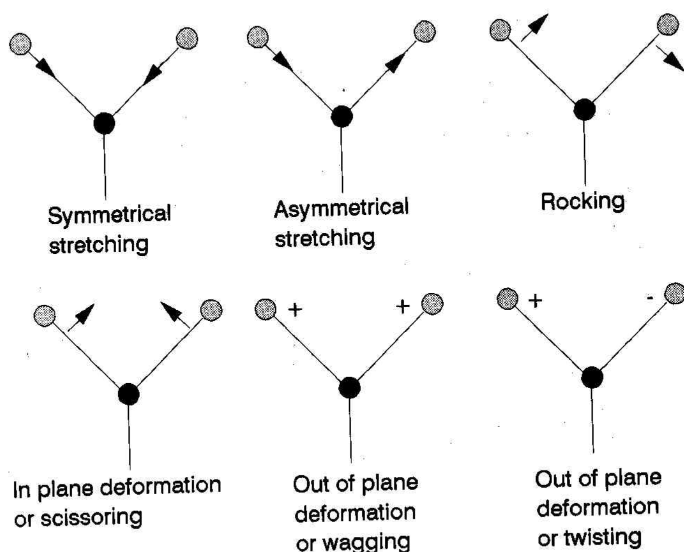

Figure 3.6. Some of the possible molecular vibrations for two identical atoms bonded to a third dissimilar atom. [48]

The integrated absorption of the Si-H rocking/wagging mode at 630 cm^{-1} is a good measure of the total content of bonded hydrogen within the amorphous sample.

The reason is that whatever the nature of the bond Si-H; Si-H_2 etc., all types of vibration will contribute to the 630 cm^{-1} absorption band.

Different vibrational frequencies for SiH_x (x = 1-3) in hydrogenated amorphous Si have been identified as shown in table 3.1.

Group	Stretching	Bending	Rocking/wagging
SiH	2000	…	630
SiH_2	2090	880	630
$(SiH_2)_n$	2090-2100	890,845	630
SiH_3	2140	950,860	630

Table 3.1. Vibrational frequencies of SiH_x (x = 1-3) in a-Si: H. [55]

The integrated absorption band I_w is given in terms of the absorption coefficient $\alpha(w)$ by:

$$I_w = \int \frac{\alpha(w)}{w}\, \mathrm{d}w \qquad (3.66)$$

and the bonded hydrogen density N_H in cm^{-3} is given by

$$N_H = A_w I_w \qquad (3.67)$$

where A_{630} = 2.1 x 10 ^{19} cm^{-2} is the proportionality constant determined by Langford *et al.*[57] and the $A_{2000-2090}$ = 1.1 x 10^{20} cm^{-2} was determined by Beyer and Abo Ghazala [58]. These constants which express the strength of vibration modes have been calculated for a-Si:H. Their application to microcrystalline and polycrystalline Si may include some errors. Applied to a-Si:H, the analysis estimates the integrated strength with a typical error of less than 15% [37].

A closer look on the table above suggests that the stretching band at 2000 cm^{-1} correlates with Si- H groups while the stretching mode at $\cong$ 2100 cm^{-1} correlates with SiH_2 and clustered $(SiH_2)_n$ groups on internal surfaces of voids and / or on grain boundaries [59-60].

The ratio $R^* = \frac{I_{2100}}{I_{2000} + I_{2100}}$ tells empirically about the film inhomogeneties such as microvoids throughout the material. As the 2100 cm^{-1} contribution increases, the ratio R^* increases which is the sign of poor quality material.

3.5. Elastic Recoil Detection

3.5.1.Theoretical background

Elastic recoil detection (ERD) is an ion beam analysis technique in which high energetic heavy ions are used to recoil light target atoms kinematically. The spectrometry of the recoiled atoms is used to obtain depth profiles of the low atomic number ($1< Z < 8$) elements present in the sample [61].
When an incident particle of mass m_1 and energy E_0 hits a target nucleus of mass m_2 initially at rest, the target recoils with energy E_2 at an angle ϕ between 0 and 90°. The energy of the recoiled atom is given in the laboratory system by [62]:

$$E_2 = KE_0 \tag{3.68}$$

where the energy ratio known also as the Rutherford kinematic factor K is given by conservation of both energy and momentum as

$$K = \frac{4m_1 m_2}{(m_1 + m_2)^2}\cos^2 \phi \tag{3.69}$$

Another important parameter in ERD spectrometry is the depth resolution that is defined as the ability of an analytical technique to detect a variation in atomic distribution as a function of depth. An attempt here is done to study its variation in the simple reflection geometry where the incident angle θ_1 is chosen to be equal to the exit angle θ_2 for simplicity (we will refer to those angles as θ in the calculations). Fig. 3.7 gives the set-up schematic. Considering a situation where the recoiled originates from a depth x under the surface, the energy of the recoiled $E(x)$ in the beam direction θ from the sample normal is given by:

$$E(x) = K\,(E_0 - \frac{d\overline{E}_1}{dx} l\,) \tag{3.70}$$

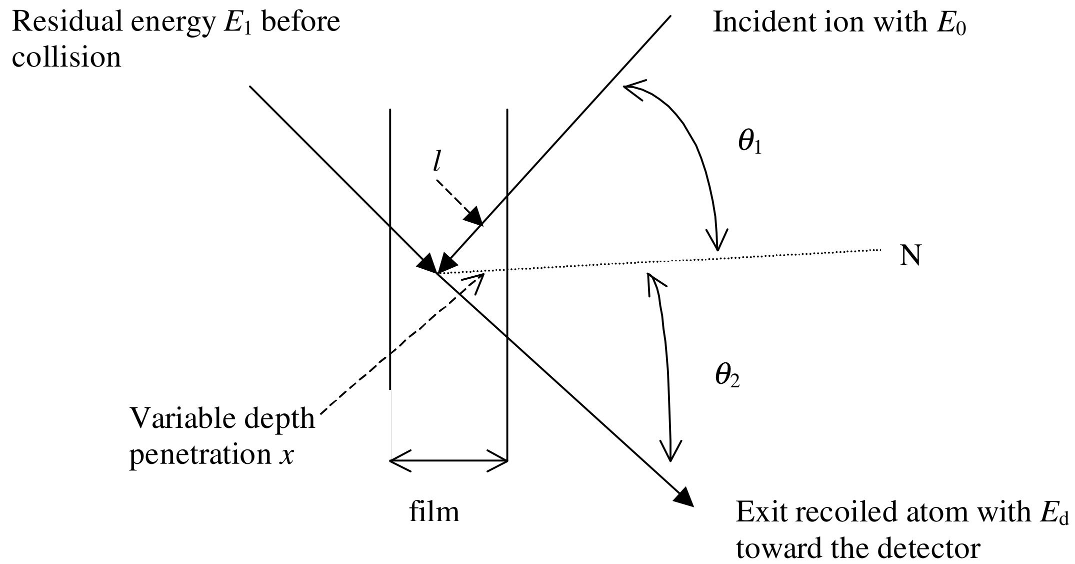

Fig. 3.7. Schematic used for qualitative derivation of the depth resolution. One layer is considered for simplicity.

E_0 is the energy of the projectile; $\frac{d\overline{E}_1}{dx}$ - the mean specific energy loss of the incident beam in x thickness [63] and l is geometrically given by x / cosθ. At any depth, the remaining energy is thus deduced as

$$E_1(x) = E_0 - \frac{d\overline{E}_1}{dx} l \tag{3.71}$$

With the same reasoning the residual energy of the recoiled atom when it exits the sample (after an additional travel of l) is given by

$$E_d(x) = E(x) - \frac{d\overline{E}_2}{dx} l \quad (3.72)$$

where $\frac{d\overline{E}_2}{dx}$ - mean specific energy loss of the recoiled atom after impact. The rearrangement of the equation (3.70) yields

$$E_d(x) = KE_0 - \frac{1}{\cos\theta}\left(K\frac{d\overline{E}_1}{dx} + \frac{d\overline{E}_2}{dx}\right)x. \quad (3.73)$$

Equation (3.73) can be rewritten as

$$E_d(x) = KE_0 - \frac{1}{\cos\theta} cx \quad (3.74)$$

where $c = K\frac{d\overline{E}_1}{dx} + \frac{d\overline{E}_2}{dx}$ (3.75)

From equation (3.73), the depth resolution for a fixed θ is obtained as

$$\Delta x \sim -\frac{\Delta E_d}{\frac{1}{\cos\theta} c} \quad (3.76)$$

Good depth resolutions Δx are then obtained for small detector energy resolutions ΔE_d. The incident angle should moreover be chosen as close as possible to $\pi/2$ for better depth resolutions. The physical meaning of the negative sign is that atoms ejected from deeper in the sample give smaller detected energies. Theoretically the depth resolution is a more complex problem because it is affected by many other factors such as straggling in the range foil and sample, nonuniformities in the range-foil thickness, sample roughness and kinematics [64]. A detailed discussion on depth resolution in ERDA can be found in the references [64] and [65].

In a more general geometry of ERD analysis, the projectile has an angle of incidence θ_1 from the target normal and the recoiled atom is detected at an angle θ_2. Moreover a range foil is placed in front of the detector in order to filter out the high intensity He scattered beam from silicon atoms in the sample; one must account for the stopping power of this foil in the calculation of the detected energy. Since the detected energies are a function of the depth of the scattering atom in the sample for a given element, the atoms extracted from the surface yield higher detected energies because they are not subjected to any stopping power. The knowledge of the yield as function of depth provides the information about the given element depth profile and of course the content of the scattering atoms in the sample.

The link between the number of target atoms N_s and the detected particles or yield Y through a solid angle Ω is given by the scattering cross section $\sigma(\phi)$ [62];

$$Y = \sigma(\phi)\cdot\Omega\cdot Q\cdot N_s \tag{3.77}$$

where ϕ is the scattering angle and Q is the total number of the beam incident particles. The solid angle Ω for small detector areas as the ones considered in this particular experiment is given by the ratio between the detector area A and the square of the distance l from the target to the detector aperture (A / l^2) in steradians. One defines an average differential scattering cross section as

$$\sigma(\phi) = \frac{1}{\Omega}\int_{\Omega}\frac{d\sigma}{d\Omega}d\Omega \cdot \tag{3.78}$$

For Rutherford scattering the recoil production cross section $\sigma(E_0,\phi)$ is given by [66]:

$$\sigma(E,\phi) = \left[\frac{Z_p Z_r e^2 (M_p + M_r)}{2M_r E}\right]^2 (\cos\phi)^{-3} \cdot \tag{3.79}$$

Z_p, Z_r are the atomic number for the projectile and recoil atoms respectively; M_p and M_r their masses while e is the unit charge. Theoretical studies indicate that actual cross-sections can deviate from the Rutherford cross-section at both high and low energies due to the influence of the nuclear force and the partial screening of the nuclear charges respectively [64,67]. As the use of a He projectile beam for ERD above 1 MeV lies in the region where penetration of the Coulomb barrier can occur [64], a non –Rutherford recoil cross-section given by Baglin *et al.* [67] for H (^{4}He,H) ^{4}He was chosen for our simulations. Fig. 3.8 shows how the scattering cross section proposed by Baglin deviates from the Rutherford cross section for He-H in case of a recoiled angle of 30 ° as used in our experiment.

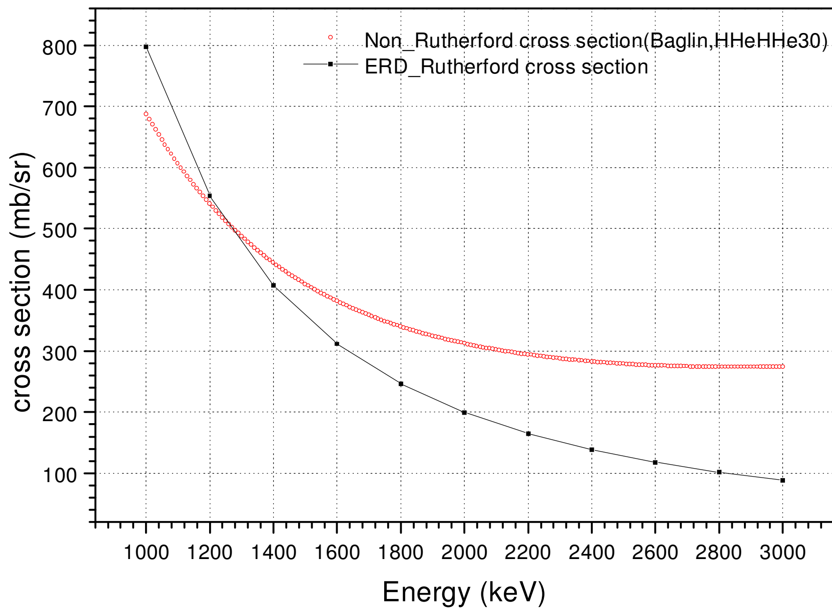

Fig. 3.8. Non-Rutherford cross section of Baglin (HHEHHE30.R33) compared to the one predicted by Rutherford for recoils in the laboratory system. The energy range of the projectile beam is 1-3 MeV and the recoiled angle is 30 °.

The knowledge of the scattering cross section and of the solid angle makes it possible to relate the yield to the concentration of scattering atoms.

3.5.2. The experimental set-up

The experimental set-up used to collecting the data is based at the Materials Research Group of iThemba LABS, Faure. He^+ particles ranging from 2 to 3 MeV were accelerated by a van de Graaff Accelerator through a 1 mm collimator before they hit the sample kept in a chamber evacuated to pressures better than 10^{-4} mbar. The sample was tilted to an angle of 15° with respect to the ion incident beam and a Si detector positioned at a recoil angle of 30° was used to collect the recoiled atoms. Fig. 3.9. gives the experimental set-up for elastic recoil detection using reflection geometry [65] similar to the one used in our experiment. The detector had an active area of 100 mm^2, a depletion depth of 100 μm and a nominal resolution of 13 keV.

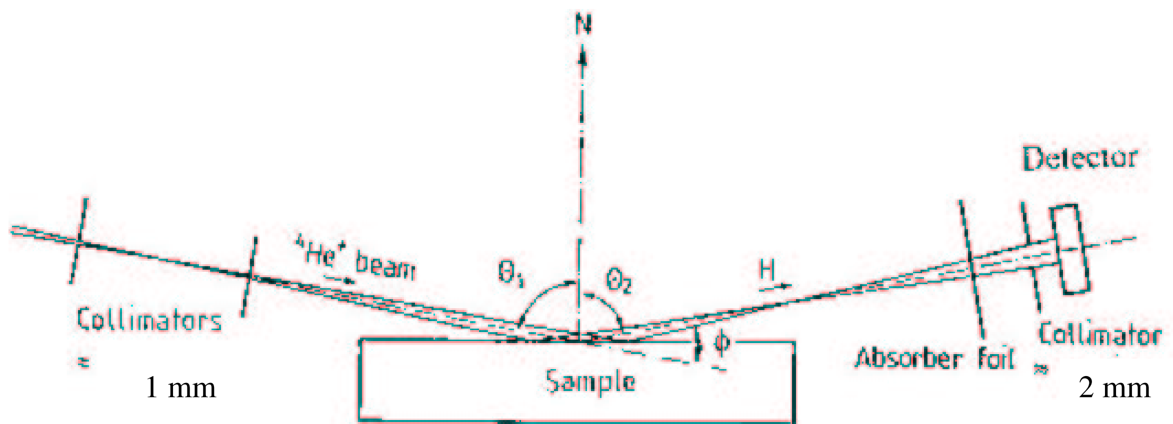

Fig. 3.9. Experimental set-up for elastic recoil detection using reflection geometry.

An aluminum range foil 12.5 µm thick was placed in front of the detector in order to prevent the scattered heavy He ions to enter the detector and overshadow the hydrogen spectrum. The electronic signal obtained from the detector was amplified and processed electronically before it was stored in different band channels corresponding to given energy bands after appropriate calibration.

For channel-energy calibration purpose, a Mylar ($C_{10}H_8O_4$) foil 15 µm thick was bombarded with 3 different beam energies 2, 2.5, and 3 MeV respectively giving 3 erd-spectra. A correlation between the recorded energies and channels was done using a following linear form

$$E \text{ [keV]} = A + B \times channel \tag{3.80}$$

where E is the particle energy, A the calibration offset and B the energy per channel factor. For illustration purposes, fig.3.10. shows how the detected energies are related to the channels. An offset energy of 100.9 keV is obtained in this example.

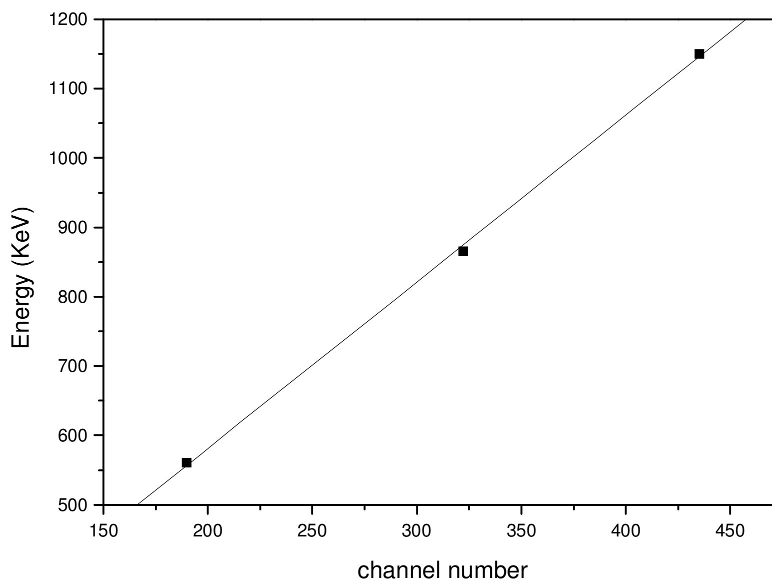

Figure 3.10. Energy-channel calibration experiment; the three shown points on the graph correspond to 3 calculated detected energies from an initial beam of 2, 2.5 and 3 MeV respectively.

A projectile beam of 3 MeV was used to analyse the films grown on c-Si substrates. A total charge of 5000 nC was collected each time with a current varying from 10 to 40 nA. SIMNRA [67], a simulation program for nuclear reactions was used to analyse the spectra.

3.6. Transmission electron microscopy (TEM) Analysis

3.6.1. Theoretical background

In the transmission electron microscope, the image is formed, magnified, inverted or redressed by means of lenses in a transmission arrangement. Theoretically by increasing the number of lenses, one can achieve as high a magnification as possible although practically it is a futile exercise when the instrument resolution limit has been reached. The resolution is defined in terms of the minimum distance between two images points that can just be distinguished as two independent points. In diffraction theory, the resolution limit is given by [68]:

$$r_1 = \frac{0.61\lambda}{n \sin \alpha} \qquad (3.81)$$

where λ is the wavelength of the radiation used; for the electrons it typically depends on the accelerating voltage in an inverse relationship.

n the refractive index of the medium between the object and the objective lens.

α is the semi-angle subtended by the microscope aperture at the point specimen.

From the relation (3.81), it is understood that the resolution is improved by (a) the use of short wavelength beam, (b) an optically dense material like an oil immersion objective lens with high refractive index and (c) large apertures. The efforts to improve the instrument resolution must however take into account another important parameter in

electron microscopy, the depth of field. It is defined as the range in focus between which the specimen is moved without losing the sharpness of the image and is given by [68]:

$$h = \frac{0.61\lambda}{n \sin\alpha \tan\alpha} \qquad (3.82)$$

There is then an inverse relationship between the highest depth of field and lowest resolution limit r_1 in electron microscopy.

Since the angles through which the electrons are deflected are very small, as a good approximation the sine and the tangent can be replaced by the angle. The theoretical resolution and depth of field for an electron microscope can then be written respectively in vacuum as:

$$r_1 = \frac{0.61\lambda}{\alpha} \qquad (3.83)$$

and

$$h = \frac{0.61\lambda}{\alpha^2} \qquad (3.84)$$

A decrease in α then sees the depth of field increasing very rapidly while the resolution is deteriorating and vice versa.

In our analysis, since we are concerned in a material which is mainly amorphous with inclusion of small polycrystallites, both absorption and diffraction contrasts are used. The image contrast is due to the variation in intensities of transmitted and diffracted beams depending on the microstructural features and elemental distribution on the electron path in the specimen. In imaging mode, when the unscattered beam is the only one admitted through the objective aperture and used for imaging, the atomic number, thickness and density of the target sample determine whether few or many electrons will be transmitted; in an amorphous material any defective part of the material will appear dark on a bright background and obviously the amount of scattering will determine the contrast (bright field condition). When another diffracted beam is the one selected through the aperture and the central transmitted beam is blocked, the defect part of the specimen will appear

bright on a dark background (dark field condition). This will be the case for the crystallites and grains embedded in an amorphous network as well. The diffraction method often used in Materials Science allows to measure the size of the unit cell and identify the orientation of the crystals by applying the Bragg law in reciprocal space.

3.6.2. Specimen preparation

Samples used in cross section transmission electron microscopy analysis must be thin enough to be transparent to electrons (in the order of 1 μm for silicon like material).
In the first stage of preparation, 2 cleaned strips of substrates with a deposited thin film to be analysed are glued and sandwiched so that the surfaces of interest face each other. Two dummy substrates may be added on the outside to provide additional strength and width.
The sandwich is sectioned off in cross sections by a diamond saw. One slice is then about 0.4 mm thick. (See fig. 3.11.)

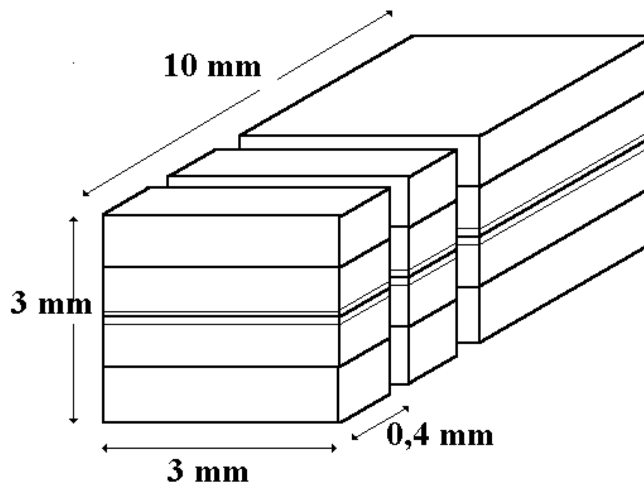

Figure 3.11. Glued sandwiched substrates with the film surfaces facing each other in the centre. Two dummy substrates are placed outside for additional strength.

The specimens are thereafter mounted on a glass block with all the thin film interfaces aligned parallel as shown in fig. 3.12. to allow only one-direction grinding and polishing.

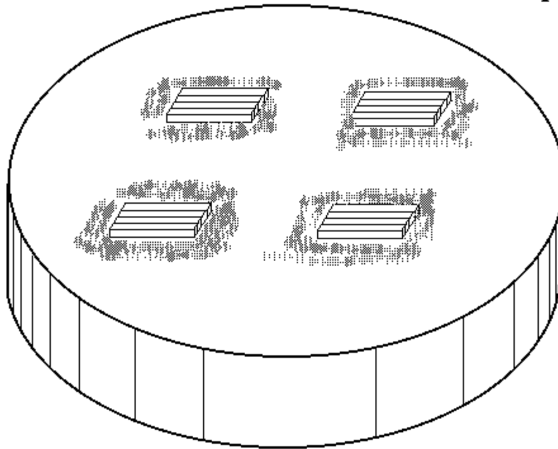

Figure 3.12. Glass block with four XTEM samples mounted with crystal bond wax.

Samples are ground down on the 400 grit polishing paper mounted on a rotating wheel. When the samples are showing a smooth polished surface the rotation process is stopped and with a stationary wheel, a linear polishing parallel to the glue lines is done.
Mylar films of respectively 15, 6, 3, 1, and 0.5 µm on a stationary wheel are used sequentially to remove any scratches from the previous polishing.
The final surface has to be mirror smooth, free from any polishing marks before turning over the specimens to their unpolished sides.
The same procedure as above is followed starting by the 400 grit-rotating wheel and the thickness of the different specimens are progressively checked using a dial micrometer. Once the specimens are around 50 µm thick, the linear polishing is commenced across the grinding paper, which is kept stationary for careful control on the thickness. This step

is stopped when the specimens are smoothly polished, free from any trace of wax and they are less than 30 μm thick.

The following step uses the same Mylar films as above (15, 6, 3, 1 and 0.5 μm) for a smooth mirror finish. Care should be taken with the linear polishing using a light microscope as at this stage the sample is very thin and cannot easily be seen by naked eye.

A copper TEM grid is finally mounted on each XTEM prepared specimen around the interface using a mixture of resin glue. The TEM grid is completely opaque for electrons and its primary purpose is to ease the mechanical handling of the very thin and extreme fragile sample.

Fig. 3.13. shows the mounted XTEM sample on the grid, ready for ion milling from both sides.

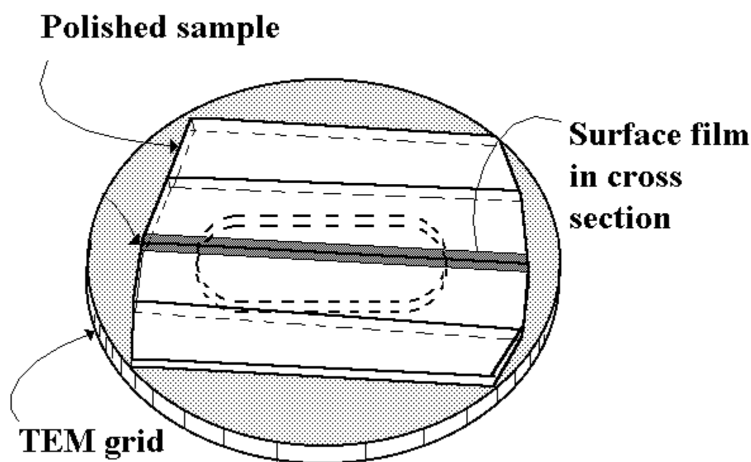

Figure 3.13. Mounted XTEM sample on TEM grid, ready for ion milling.

The ion milling stage is a sputtering process of further thinning the specimen to electron transparency using energetic Argon atoms directed towards the sample at a grazing angle of 7°. Contrary to the polishing process, one never mills the sample parallel to the interface.

Typical currents of 2-3 mA and high voltages between 5-7 kV are used for two different guns (one from the top and another from the bottom) in a chamber evacuated to pressures better than 10^{-4} mbar. The sample is ready to be viewed in the TEM when the first holes start appearing in the sample. The thin interface regions next to the visible hole in the sample are important since they are the only ones transparent to electrons. There the thickness is of the order of 1μm.

3.7. Electrical measurements

3.7.1. Dark and photo-conductivity

The electrical characterization discussed in this thesis consists of measuring the dark and photoconductivity of the film under study.

Practically, 2 silver electrodes with a length l of 20 mm with a distance separation w of 0.5 mm are deposited on the sample.

From the *I-V* characteristic, the conductivity of the material is determined by [49]:

$$\sigma = \frac{Iw}{Vld} \qquad (3.85)$$

Where I is the measured current

V is the applied voltage

d is the thickness of the film

The dark and photoconductivity were measured successively in complete darkness and using a solar simulator from Oriel with a Xe lamp source operating under standard conditions of AM1.5 (i.e. 100 mWcm^{-2}). The reported values in this work were obtained with an applied voltage of 100 V.

3.7.2. Conductivity and Mobility

For a solid in thermal equilibrium, the net motion of a group of electrons n in a cm^3 over any period is nil and thus no net current is flowing.
However when an electric field $\boldsymbol{E}_x$ is applied in the $\boldsymbol{x}$- direction, each electron will experience individually a net force $-q\boldsymbol{E}_x$ so that the group of n electrons will have a net motion along $\boldsymbol{x}$ direction. If we consider $\boldsymbol{P}_x$ as the total momentum of the group in the $\boldsymbol{x}$ direction, we can write

$$-nq\boldsymbol{E}_x = \frac{d\boldsymbol{P}_x}{dt} \tag{3.86}$$

Considering a steady electric field and the fact that the accelerating effect of $\boldsymbol{E}_x$ is balanced by the deceleration process due to the collisions of electrons with the lattice atoms, other electrons, impurities and defects; we may express the current density as [5]

$$\boldsymbol{J}_x = -qn\langle \mathbf{v}_x \rangle \tag{3.87}$$

where $\langle \mathbf{v}_x \rangle$ is the average net velocity for electrons equal to $\frac{\langle \boldsymbol{P}_x \rangle}{m_n *} = -\frac{q\bar{t}}{m_n *}\boldsymbol{E}_x$

with $\bar{t}$ - mean time between scattering events and $m_n *$ -effective mass of the electron[3] [5] which takes into account the interactions of the electron in the lattice.
A simple substitution of the average velocity by its value in the current density expression shows that the current density is proportional to the electric field and the proportional factor is known as conductivity σ $(\Omega\text{-cm})^{-1}$ from Ohm's law:

---

[3] $\langle \boldsymbol{P}_x \rangle = \hbar \boldsymbol{k}_x; E = \frac{1}{2}m\mathbf{v}^2 = \frac{1\boldsymbol{P}^2}{2m} = \frac{\hbar^2\boldsymbol{k}^2}{2m}; \frac{d^2E}{d\boldsymbol{k}^2} = \frac{\hbar^2}{m*} \Rightarrow m^* = \frac{\hbar^2}{d^2E/d\boldsymbol{k}^2}$

$\boldsymbol{J_x} = \sigma \boldsymbol{E_x}$, where $\sigma = \dfrac{nq^2\bar{t}}{m_n^*}$

The conductivity expression can be rearranged as follows

$\sigma = qn\mu_n$, where $\mu_n = \dfrac{q\bar{t}}{m_n^*}$ is known as electron mobility describing the ease with which the electrons drift in the material.

If both electrons and holes participate in the conduction process, the current density is expressed as

$$\boldsymbol{J_x} = q\,(n\mu_n + p\mu_p)\,\boldsymbol{E_x} = \sigma \boldsymbol{E_x} \qquad (3.88)$$

where p is the number of holes in 1 cm^3 and μ_p the mobility for holes.

3.7.3. Activation energy measurements

The conductivity of a-Si:H is thermally activated over a limited temperature range and is described by [69]:

$$\sigma(T) = \sigma_0 \exp(-E_a / kT) \qquad (3.89)$$

where σ_0 is the conductivity prefactor and E_a the conductivity activation energy. The latter is given by the difference between the average energy of the conducting electrons and the Fermi energy. For a practical determination of E_a, a sample placed in a vacuum chamber was heated from room temperature to a final temperature of 160°C at a heating rate of 3°C / min. and subsequently was cooled down to 10°C at a cooling rate of 0.5°C / min. A voltage of 100 V was applied over the sample electrodes and the current through the layer between the electrodes was measured as a function of the temperature. Thereafter an Arrhenius plot of the dark conductivity data versus the reciprocal

temperature (ln (σ) vs. 1000 / T) was done and the activation energy was calculated from the slope of the graph in its cooling region. It is estimated that E_a can be determined in the temperature range 50° < T < 160° C with an accuracy of ≈ 100 meV [19].

Chapter 4. Results and Discussion

The results presented in this chapter were obtained from two different regimes of deposition as summarized in Table 4.1:

- The regime of high substrate temperature where the temperature of the substrate heater was kept at 450°C.
- The regime of moderate substrate temperature where the temperature of the substrate heater was preset at 375°C and 410°C.

In the first quoted regime, the distance filament-substrate ($d_{s\text{-}f}$) was 18 mm while in the second one, it was doubled to 36 mm in order to reduce the substrate irradiation from the filament. In both cases, the filament temperature was always fixed at 1600°C.

Table 4.1. Deposition conditions.

	Moderate temperature regime	High temperature regime
Heater temperature (T_{heater})	375 & 410	450 °C
Substrate to filament distance ($d_{s\text{-}f}$)	36 mm	18 mm
Hydrogen dilution ratio (R_{H2})	60-95%	
Chamber pressure (P)	10-60 μbar	
Filament temperature ($T_{fil.}$)	1600°C	
Deposition time (t)	10-60 min.	

4.1. Layer growth

4.1.1. Influence of hydrogen dilution on the deposition rate

As stipulated in the second chapter, the hydrogen dilution ratio and the deposition pressure increase were used as key parameters to induce crystallinity.

The control of the thickness is problematic in the HWCVD technique since it is greatly influenced by any slight change in the deposition conditions, which dictate the nature of the species contributing to the layer growth. Thin films properties being sensitive to the change in thickness, sometimes-unexpected disparities are observed when one compares samples of different thickness.

Throughout this thesis the deposition rate (r_d) is defined as the ratio between the thickness and the deposition time; in fig. 4.1 the deposition rates are plotted against the hydrogen dilution ratio at different process pressures in different regimes of heater temperature.

It can be seen that the deposition rate has a decreasing trend against the hydrogen dilution ratio for all the graphs. Slight improvement is observed in deposition rates as the process pressure is increased till a point where it eventually saturates. The graph in contrast at the top shows that higher deposition rates are obtained for films deposited with a short distance between the substrate and the filament when the created species arrive on the growing surface without undergoing many secondary reactions. However the greatest value (82.2 nm / min.) obtained for our diluted amorphous samples is still much lower than the reported value of 180 nm / min. obtained from undiluted silane when growing a-Si:H [33].

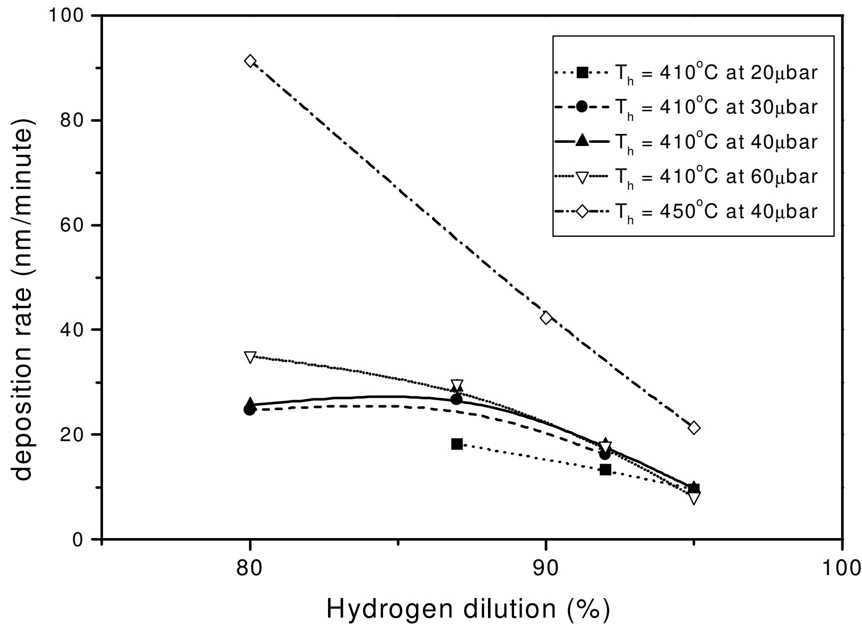

Figure 4.1. Deposition rates against the hydrogen dilution ratio at different process pressure ($d_{s\text{-}f}$ = 36mm). The top plot (with samples deposited at high substrate heater temperature and a shorter distance between the substrate and the filament of 18 mm) is there for comparison purposes.

4.1.2. Influence of the process pressure on the deposition rate

As previously mentioned in section 2.4.4, the deposition rate has an increasing trend with increasing moderate process pressures to a point where it starts to saturate and subsequently to decrease. At low pressure the mean free path length is larger than the substrate-to-filament distance [3]; the generated Si radicals then arrive to the substrate surface without secondary reactions. In this region the deposition rate is controlled by the gas supply thus directly proportional to the pressure. With the increase of the pressure, the mean free path is reduced and secondary reactions occur on the way to the substrate surface; initially at low pressures the deposition rate increases but as the pressure increases and secondary reactions start taking place the deposition rate stabilizes and reaches a maximum as can be seen in figure 4.2. on graphs (a) and (b). The graph 4.2. (c) confirms once more the detrimental effect of the hydrogen dilution on the deposition rate; at high dilution ratio increasing the pressure leads to a reduction in the deposition rate.

The decreasing trend observed is attributed to the silane depletion (H_2 predominance in the mixture) coupled with the increase of the secondary reactions occurrence rate that impede the film growth. The plot in fig. 4.2. (d) is there for comparison to show the case of the improvement of the deposition rate at shorter distance between the substrate and the filament as discussed in the previous section.

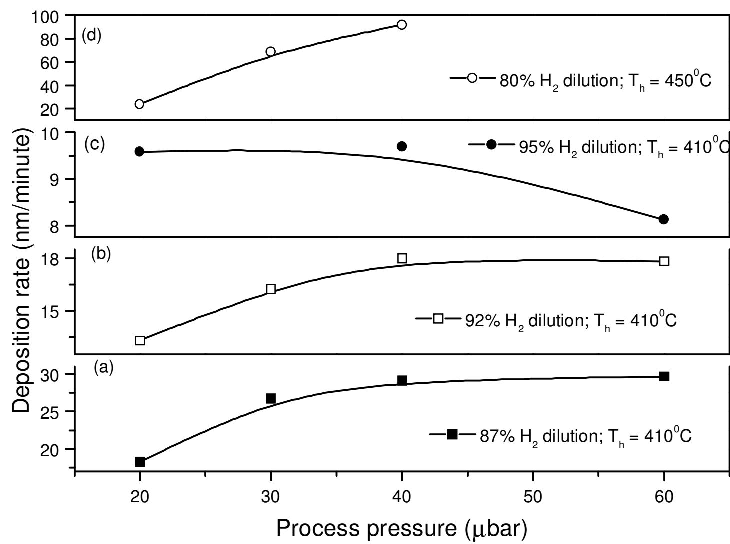

Figure 4.2. Deposition rate against process pressure with different hydrogen dilution ratios. Heater substrate temperature preset at 410°C and $d_{s\text{-}f}$ = 36 mm (The top plot with T_h = 450°C and $d_{s\text{-}f}$ = 18 mm is there for comparison).

4. 2. Optical properties

As discussed in the third chapter, all the optical parameters namely refractive index (n), absorption coefficient (α), and energy gap (E_g) have been calculated from the transmission spectra as obtained from the spectrophotometer. The obtained results have an accuracy of typically ±5%.

4.2.1. Refractive index

The reported values for the refractive index throughout this thesis are those at zero energy (n_0) calculated from a fitting function of the form [45],

$$n(\lambda) = \frac{a}{\lambda^p} + n_0 \qquad (4.1)$$

where a is a constant related to the layer thickness, and p is the order of the best polynomial fit, typically between 2 and 5; in our case a third order was most appropriate. The knowledge of the thickness is then crucial for the accurate determination of n_0. However this procedure based on an iterative calculation with a guessed value of the thickness as input is good enough and yields values with typical errors of ± 5%. The values of the extrema (read from the transmission spectrum) and the order of the extrapolated first extremum for $\lambda = \infty$ are required as input. An illustrative graph of the determination of the first extremum is shown in fig. 4.3. for a 90% hydrogen dilution ratio with a process pressure of 20 µbar.

Practically the first read maximum starting in the long wavelength (smallest wavenumber on the graph) region of the spectrum is assigned an ordinate ($l/2$) equal to zero; the following extrema alternating between minima and maxima will be assigned successive half-integer and integer in step of 0.5 and by means of recurrence the linear extrapolated ordinate corresponding to a wavenumber of zero will give the order of the first extremum, integer for a maximum and half integer for a minimum.

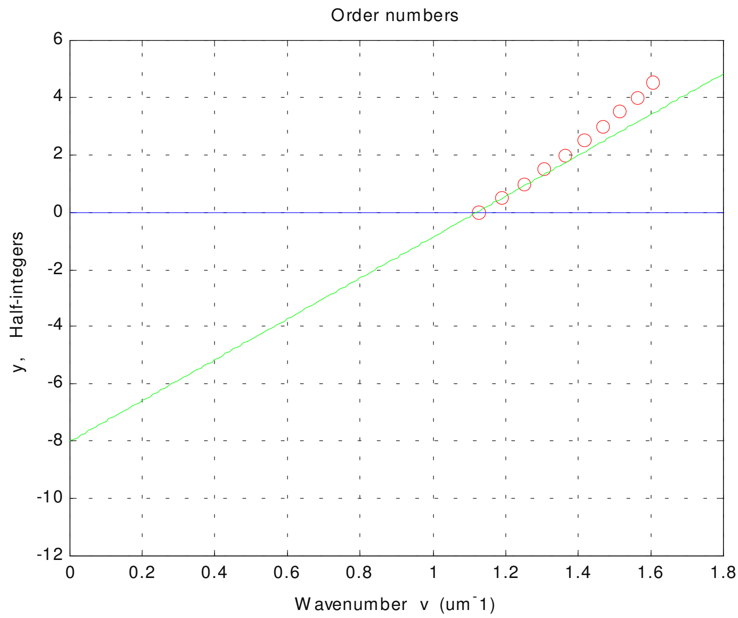

Figure 4.3. Determination of the first order number of the extrema.

Once n_0 and the constant a have been generated, the equation (4.1) above can be used to calculate the refractive index at any wavelength. Typical plots have been obtained as illustrated in fig. 4.4.

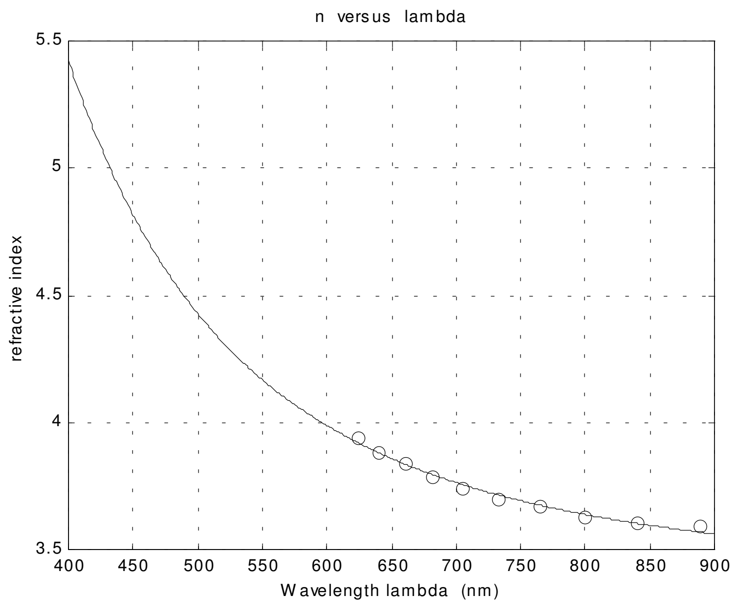

Figure 4.4. Refractive index variation against the light wavelength (90% H_2 diluted sample at 20µbar and a substrate heater temperature of 450°C).

4.2.1.1. Variation of n_0 with hydrogen dilution ratio

It has been previously reported that the refractive index is a measure of the density of the material [3] as the light wave bends more when travelling through a dense material with high values of the refractive index n_0. It has been found that n_0 was decreasing with the increase of the hydrogen dilution ratio. The results in fig. 4.5. suggest that the increase of the hydrogen dilution ratio leads to a void rich material. The n_0 variation range for the deposited material is between 2.9 and 3.4. We recall that n_0 for the c-Si is 3.42.

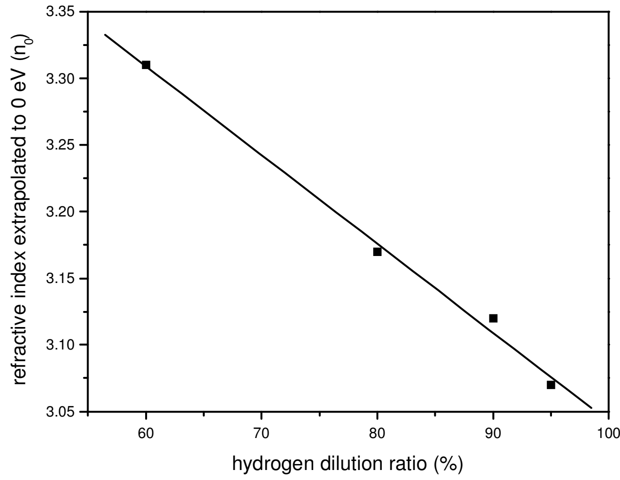

Figure 4.5. Variation of the refractive index (n_0) with hydrogen dilution ratio (samples deposited at T_h = 375°C and a process pressure of 20 μbar).

4.2.1.2. Influence of the pressure on n_0

The plot (a) in figure 4.6 shows that n_0 is increasing when the deposition pressure is increasing when the hydrogen dilution was relatively low (we use high H_2 dilution ratio only for $R_{H2} \geq 90\%$ as convention in this work) at moderate substrate temperature where the films are observed to be amorphous. An increase in the process pressure has then a densification effect as the material gets more ordered. We believe that at this stage, a certain amount of SiH_3 is created through the gas reactions and contributes to the growth. Konagai *et al.* [33] have suggested that a preferential supply of SiH_3 and a sufficient supply of atomic hydrogen contribute to high-quality silicon growth since the SiH_3 radical has a sufficiently long lifetime to diffuse onto the growing surface. It can migrate for long times across the surface until it finds a reactive location such as a dangling bond. As the hydrogen dilution was increased to above the threshold of crystallinity at this same temperature (the threshold point was attained at R_{H2} = 92% with P = 40 μbar as will be

shown in the phase transition section), the film incorporates more voids which reduce the density of the material (as related to n_0) as can be seen on graphs (b) and (c) in fig. 4.6. where the refractive index has a decreasing trend with the increase of the pressure. A sharp decrease is even noted on graph (d) in fig.4.6. at very high hydrogen dilution (95%) and high heater temperature (450°C) where a high crystalline volume fraction has been observed, as will shown later in the Raman analysis.

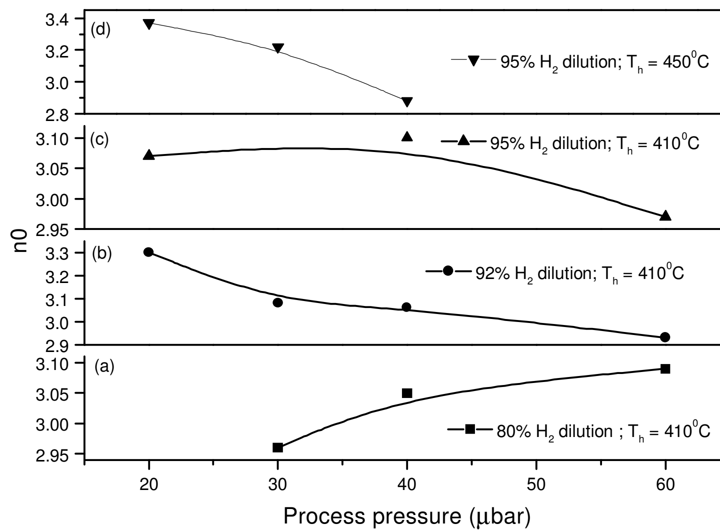

Figure 4.6. Variation of the refractive index with the process pressure at different hydrogen dilution ratios. The heater substrate temperature was maintained fixed at 410°C. The 450°C plot (d) has been included for comparison.

4.2.2. Absorption coefficient

As mentioned in the first section of the third chapter, the absorption coefficient (α) can be related to the absorbance. When plotting it against energy, it shows as expected high values at high energies since the photons have energies above the bandgap and low values on the other side of the spectrum. The absorption profile for this class of materials does not show a sharp extinction when the optical energy gap is approached as observed for c-Si [70], instead low values of the absorption coefficient are observed due to the

presence of intrinsic native defects. The void-associated dangling bonds contribute to the mid-gap density of states while the weak reconstructed Si bonds contribute to the band tails [56]. All the samples deposited during this investigation have been found to have an absorption coefficient of more than 1 x 10^4 cm^{-1} in the useful range of the visible spectrum at 2.0 eV (energy for photons of wavelength around 620 nm).

4.2.2.1. Influence of the hydrogen dilution ratios on α

Fig. 4.7 shows roughly that the absorption coefficient decreases with the increase of the hydrogen dilution ratio. Fig. 4.7. (a) and (b) illustrate a smooth decrease of the α with the decrease of the photon energy over a long range for samples grown with low hydrogen dilution. The "bumps" for energies below 2 eV observed in the highly diluted samples (fig. 4.7. (c) and (d)) are due to the fact that the experimental data are not accurate enough. Indeed small values of α ($< 10^3$ cm^{-1}) cannot accurately be determined with optical methods for very thin samples. They have then no physical significance and must only viewed in a mathematical perspective. This makes uncertain the value read at 2 eV for our 95 % hydrogen diluted sample (fig. 4.7. (d)).

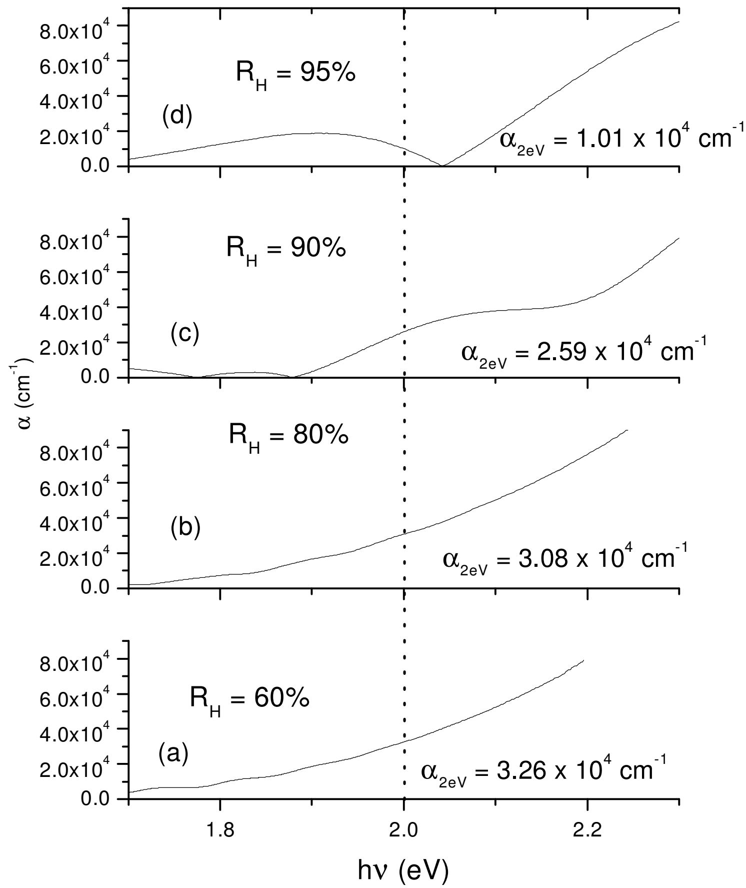

Figure 4.7. Absorption coefficient against the hydrogen dilution ratio. Respective values of α at 2eV are given for illustration purpose. (All the displayed samples were deposited at a fixed substrate heater temperature of 375°C at a fixed pressure of 20μbar).

4.2.2.2. Influence of the pressure on α

Fig.4.8 shows a decreasing pattern of the α values with increasing process pressure (we display calculated α-values at 2 eV photon-energy) although the decrease is not so sharp as in the case of the highly hydrogen diluted samples. The samples in graphs 4.8. (a) and (b) were observed to be amorphous and the smoother pattern in fig. 4.8. (b) suggest an improved order. We believe that the relatively low values in fig. 4.8. (c) and (d) are due to the indirect gap characteristic since these samples had been found to be crystalline.

The irregular shape of the graph observed in fig. 4.8.(d) may be attributed to the presence of small crystallites in the amorphous network that have the effect of optical scattering.

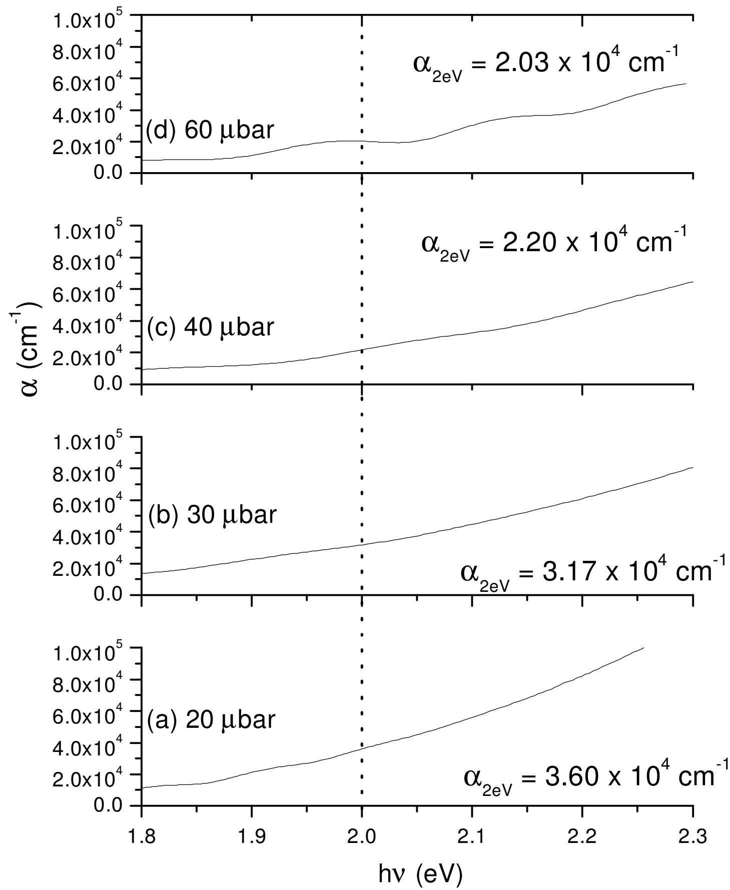

Figure 4.8. Absorption coefficient as function of the process pressure. The analysed samples were deposited with 92% hydrogen dilution ratio at a fixed heater temperature of 410°C.

4.2.3. Optical energy gap

As discussed in the first section of chapter 3 Tauc has deduced in 1974 an empirical relation relating the absorption coefficient and the optical bandgap (E_g) in the region of medium absorption of an amorphous solid:

$$(\alpha(h\nu)h\nu)^{1/2} \approx \text{const. x } (h\nu - E_o) \qquad (4.2)$$

We have used it to estimate the apparent Tauc E_g when a parabolic shape was assumed for the band or mobility edges. In assuming a linear shape of the band edges and then replacing the second order by a third order exponent the so-called cubic E_g was obtained. We have plotted $(\alpha h\nu)^{1/2}$ versus $h\nu$ and determined the cut-off with the energy axis where $\alpha = 0$ for the apparent Tauc values and used the third root for the cubic values. Fig. 4.9. gives both the Tauc and Cubic plot for a typical nanocrystalline sample. There is some controversy about which equation is best to use for the determination of E_o for a-Si:H [71] and some authors [72-73] prefer to define the gap at the energy point where the optical absorption spectrum achieves a certain threshold usually selected to be 10^3 or 10^4 cm^{-1} (E_{03} and E_{04} respectively); Sweenor *et al.* [74] have revisited all these methods and provided a means of relating these disparate measures of the optical gap in a-Si:H. We have plotted in Fig. 4.10 the results of the optical gaps obtained using four different models for comparison. It is seen that the Tauc model yields values lying between E_{03} and E_{04}, which physically represent the departure from the weak towards the medium absorption region. It appears clearly that the cubic E_g are far below both E_{03} and E_{04}.We will thus report the apparent Tauc gap values throughout this work. However it should be noted that for polycrystalline material where the amorphous tissue is almost suppressed, the indirect optical gap is better estimated from a plot of $(\alpha)^{1/2}$ versus energy using the low energy absorption region. Rath *et al.* [75] has achieved an optical gap of 1.1 eV for their optimised polycrystalline film using PDS (photothermal deflection spectroscopy) data. Applied to one of our microcrystalline sample, we have found an indirect gap of 1.12 eV. The result in appendix 4 displays the square root of the absorption coefficient (α) versus energy measured by PDS from one of our microcrystalline sample with a

crystalline volume fraction of 40.2% and a grain size of less than 10 nm. This extrapolated indirect gap value, although comparable to other published data, seems too low for our microcrystalline material that contains a fair amount of amorphous tissue. It may be attributed to the optical scattering in the material as previously observed by N. Beck *et al.* [76] in their microcrystalline material deposited by VHFCVD.

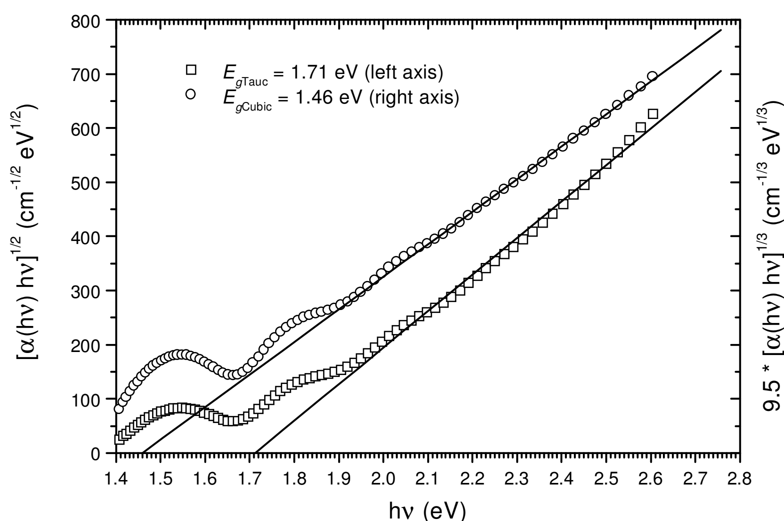

Figure 4.9. Tauc and cubic E_g for a nanocrystalline sample (R_{H2} = 92 %; P = 40μbar; T_h =410°C; d = 540 nm). Apparent Tauc E_g = 1.71 eV and Cubic E_g = 1.46 eV.

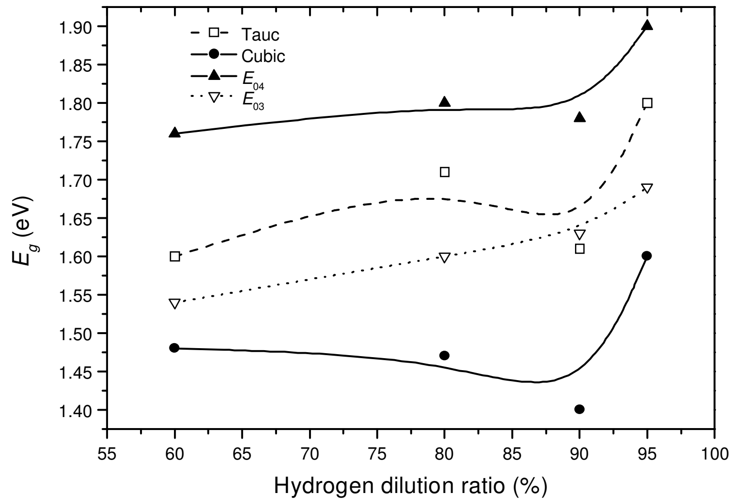

Figure 4.10. Optical energy gaps determined by four different models. E_{04} and E_{03} are read where $\alpha = 10^4$ and 10^3 cm^{-1} respectively (the increasing trend observed from 90% hydrogen dilution ratio is discussed in the next section).

4.2.3.1. Influence of the hydrogen dilution on the energy gap E_g

The hydrogen dilution, as discussed in the introductory part of this work, has a prominent influence on the structure of the deposited material and on the content of the incorporated hydrogen. Since the energy gap is related to both of them, it is understood that the hydrogen dilution will influence the gap values.

The figure 4.11. illustrates the dependence of E_g on the hydrogen dilution in different regimes of heater temperature. The process pressure was kept at 20 μbar.

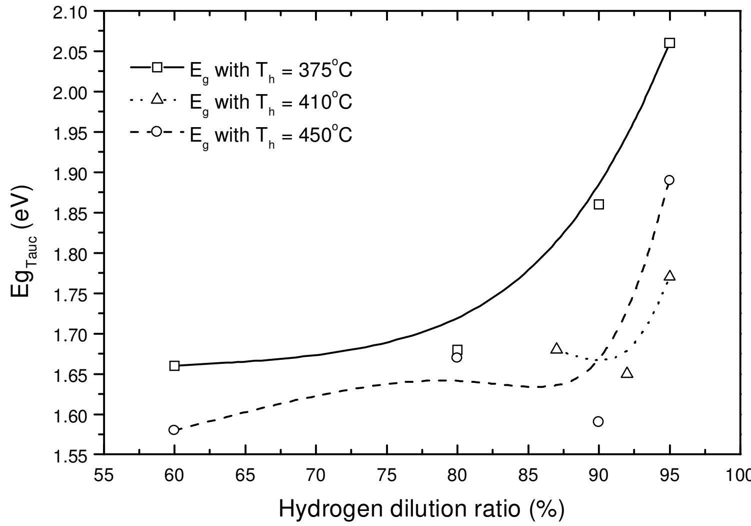

Figure 4.11. Tauc E_g versus R_{H2} in 3 different regimes of substrate temperature. The process pressure was preset at 20 μbar for all these samples.

It has been observed as reported in the coming section that the content of bonded hydrogen in the sample decreases as the hydrogen dilution ratio increases. A relationship between the optical energy gap as a function of hydrogen fraction C_H had been derived for a-Si:H grown using the conventional PECVD [38]:

$$E_{opt} = 1.50 + 1.47\, C_H \tag{4.3}$$

That seems not to be the case in HWCVD for films grown near the threshold of crystallinity from our results. We propose that E_g increases, as the density of the material is decreasing. M. J van den Boogaard and Meiling *et al.* [77-78] had reported a correlation between E_g and the average distance between neighbouring silicon atoms, $\langle d_{Si} \rangle$. Since n_0 is a measure of the density of the material, low values of n_0 correspond to higher values of $\langle d_{Si} \rangle$ and thus an increase in E_g should be expected. We have plotted in fig. 4.12. both E_g and n_0 against the hydrogen dilution ratio. In the first stage of dilution the material tends to be ordered with a densification of the film, but higher dilutions have

been observed to lead to films incorporating voids. This may lead to the observed slight decrease in refractive index values over $R_H = 90\%$ and thus corresponding apparent high-energy gaps (see fig.4.10 as well).

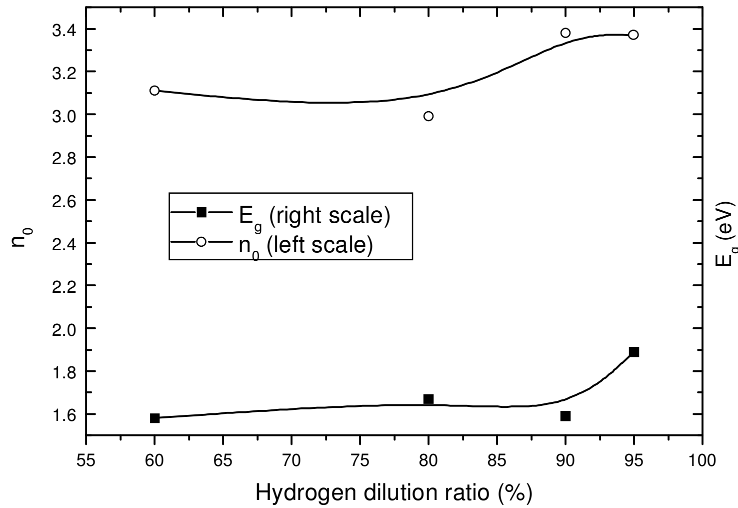

Figure 4.12. E_g (bottom graph) and n_0 (top graph) against hydrogen dilution ratio.

4.2.3.2. Influence of the process pressure on the energy gap

In fig. 4.13. we are displaying the observed trends of the Tauc energy gaps against the deposition pressure. They were taken from the data on films deposited with two different preset heater temperatures. The films deposited with T_{heater} = 375°C and a hydrogen dilution ratio of 80% have all of them been observed to be amorphous by XRD and Raman scattering. Those deposited with T_{heater} = 410°C and a hydrogen dilution ratio of 92% were showing sign of nucleation starting from a process pressure of 40 μbar. It can be seen in figure 4.13. (a) that E_g is not sensibly influenced by the deposition pressure in the amorphous phase regime while a different trend is observed in fig. 4.13. (b) where we believe that the observed increasing trend from 40μbar (threshold of crystallinity) is more

likely to be induced by the structural changes inherent to nucleation than by the process pressure.

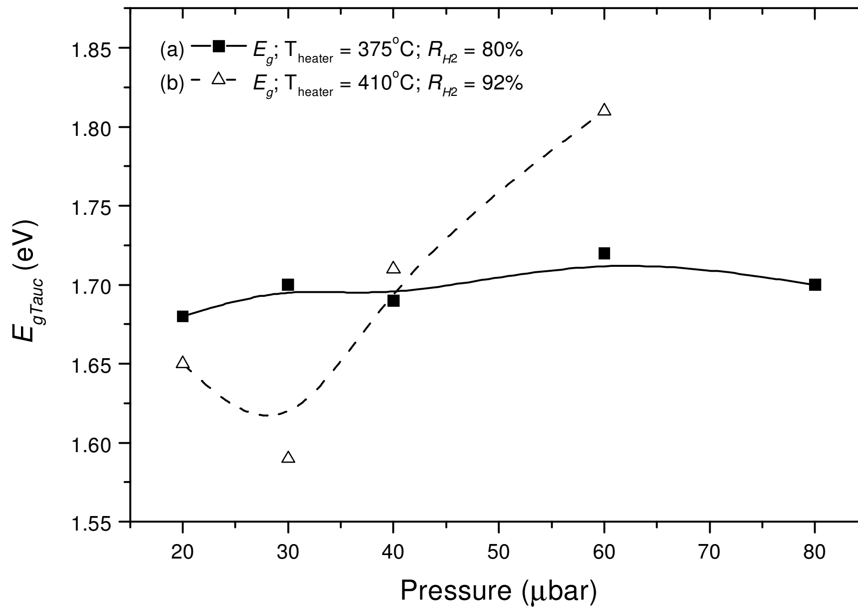

Figure 4.13. Tauc optical gaps against the process pressure in two different regimes of deposition.

4.3. Phase transitions

Depending on the technological parameters during the film deposition and thus the species created, thin films silicon can have different microstructures; Schropp *et al.* [19] distinguish 3 various morphologies: hydrogenated amorphous silicon with a single amorphous phase, hydrogenated microcrystalline silicon with two-phases (amorphous and crystalline) incorporating crystals of size less than 20 nm and hydrogenated poly-crystalline silicon with a single phase crystalline containing grain boundaries between crystals of dimensions above 20 nm. As discussed earlier, we have used the increases of hydrogen dilution ratio and deposition pressure to yield crystallinity. The dilution of the silane gas by a certain flow of hydrogen is beneficial provided that optimum conditions

are met for its decomposition into atomic hydrogen. It etches silicon from disordered or strained bonds leading to a transition from amorphous to crystalline phase [79]. The process pressure plays also an important role into the quality of the material obtained; very high pressures however lead to poor quality material because heavy silane radicals obtained from numerous secondary reactions will contribute to the film growth while very low pressures promote a rich void material since the Si obtained from the primary reactions will be the main precursors. It is known that Si has a high sticking coefficient [19,32]. Although not intended at the start of this project, we have probed as well into the effect of the substrate temperature and found evidence of its influence on the threshold of crystallinity. The phase transition point was monitored using XRD diffraction, Raman scattering spectroscopy and UV reflection spectroscopy.

4.3.1. Results of films grown at low substrate heater temperature

The deposition methodology was to take the hydrogen dilution as the changing parameter, in three different regimes of substrate temperature, and keep all other parameters fixed in one set of samples and the deposition pressure as the only changing parameter in the second. No trace of crystallinity has been observed by XRD studies in all the samples grown at the low substrate heater temperature of 375°C. Figure 4.14 shows the typical XRD- patterns of those samples on glass substrate. The deconvolution of the Raman spectra (fig. 4.15.) has shown a predominant TO peak centred around 480 cm^{-1} with only a small noticeable signal at around 505 cm^{-1} in one sample which had been deposited using a very high hydrogen dilution ratio of 95% and a pressure of 20 μbar (graph 4.15. (d) in the figure). A crystalline volume fraction of less than 5% was estimated suggesting that the films headed to phase change only at very high hydrogen dilution. It is believed that the abundance of the atomic hydrogen on or near the growing surface is the key factor to yield crystallinity in the growing film [18,50,80]; the reaction kinetics at low substrate temperature are reduced and so is the production rate of atomic hydrogen, which favours the deposition of an amorphous film.

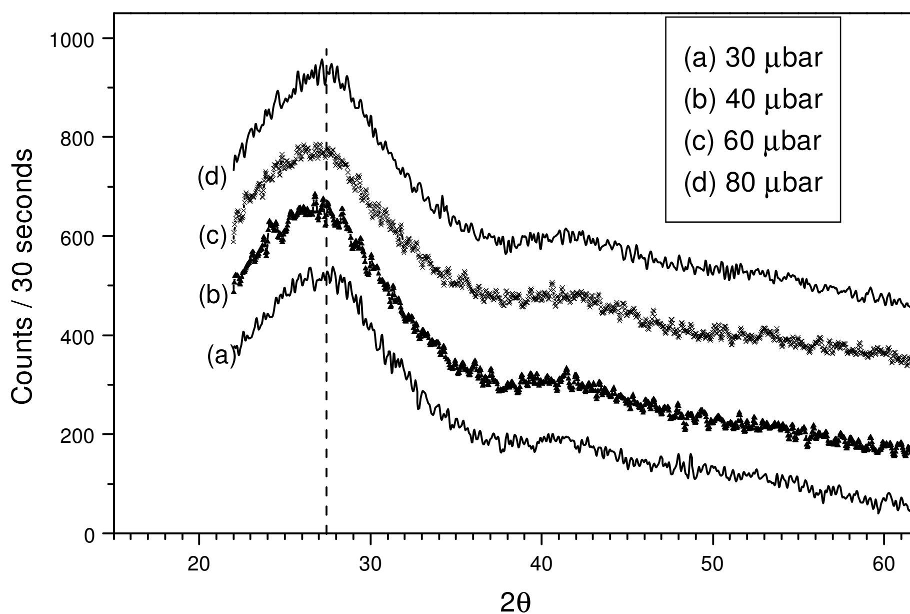

Figure 4.14. XRD- patterns of amorphous films grown with 80% H_2 dilution ratio at a substrate heater of 375°C ($d_{s\text{-}f}$ = 3.6 cm). (The graphs have been translated along the y-axis for visibility).

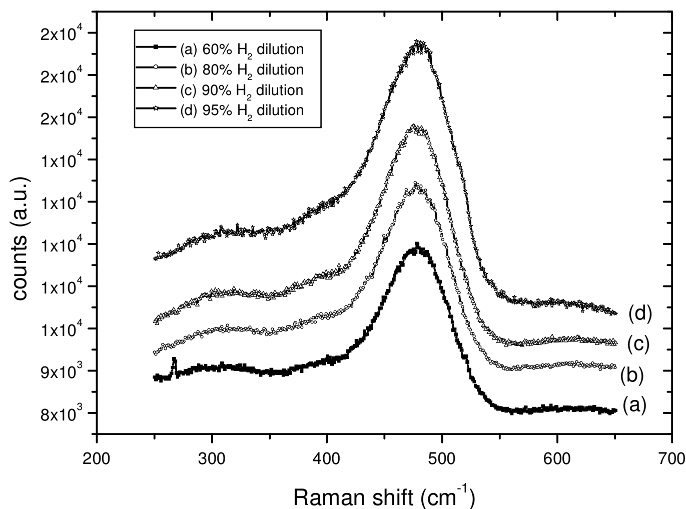

Figure 4.15. As taken Raman spectra of films grown at varied H_2 dilution ratio with a fixed deposition pressure of 20 μbar and a substrate heater temperature of 375°C.

4.3.2. Results of the material grown at moderate substrate temperature

When the substrate heater temperature was raised to a value of 410°C, XRD data have shown that the films remained amorphous up to 87% hydrogen dilution ratio in the range of pressure values used in this study; the figure 4.16. is showing clearly that a broad peak centred between 27 and 28 in units of 2θ can only be observed.

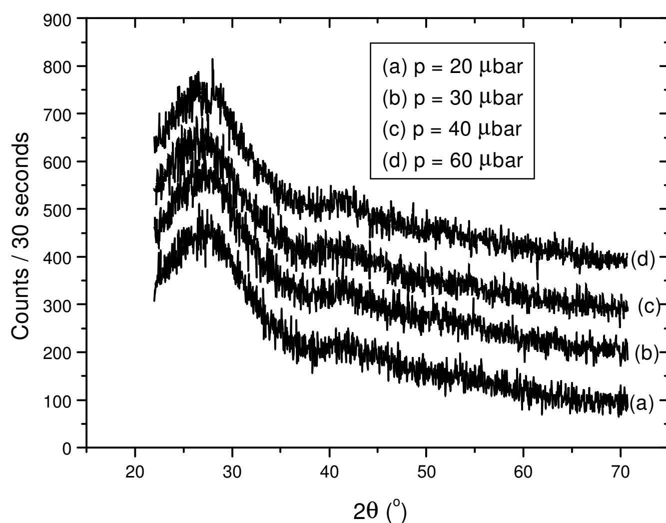

Figure 4.16. XRD-amorphous patterns of films prepared using 87% H_2 dilution with a heater substrate temperature of 410°C. (The graphs have been translated along the Y-axis).

As Raman spectroscopy is more sensitive to small changes in the amorphous network, a phase change transition could be observed in the film with label (d) in the above graph. In figure 4.17 are displayed the corresponding Raman shift spectra where a small asymmetry in the last plot (d) is observable.

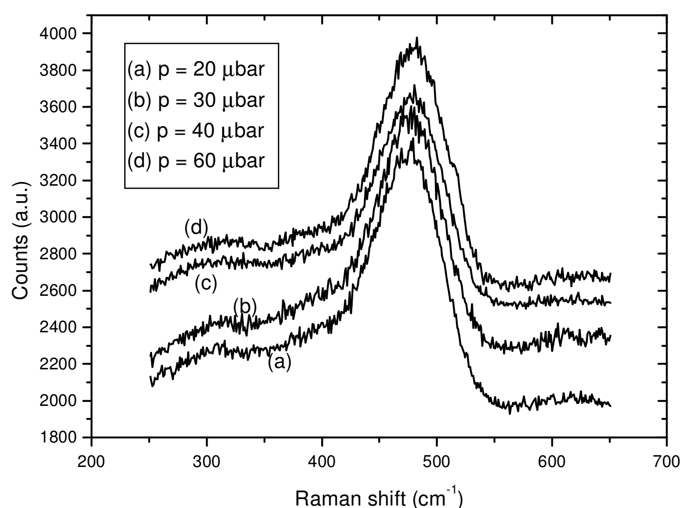

Figure 4.17. Raman shift spectra of films grown at a substrate heater of 410°C with a hydrogen dilution ratio of 87% at different process pressures.

This start of change in shape has been interpreted as the start of nucleation of small crystals in the largely amorphous network. Indeed a crystalline volume fraction of 6% could be calculated (as can be seen in appendix 5). Further, a small increase in the dilution was accompanied with both the increase of the size and the number of the crystals. This is shown by the figure 4.18. that displays the Raman shift spectra of 2 films 90% H_2 diluted at two fixed process pressures of 40 and 60 µbar. A clear peak of crystallinity emerges from the amorphous *TO* peak and it was observed to increase in intensity, narrowing and moving towards higher wavenumbers with the pressure increase. On the other hand the 480 cm^{-1} *TO* amorphous peak was at the same time shrinking in intensity.

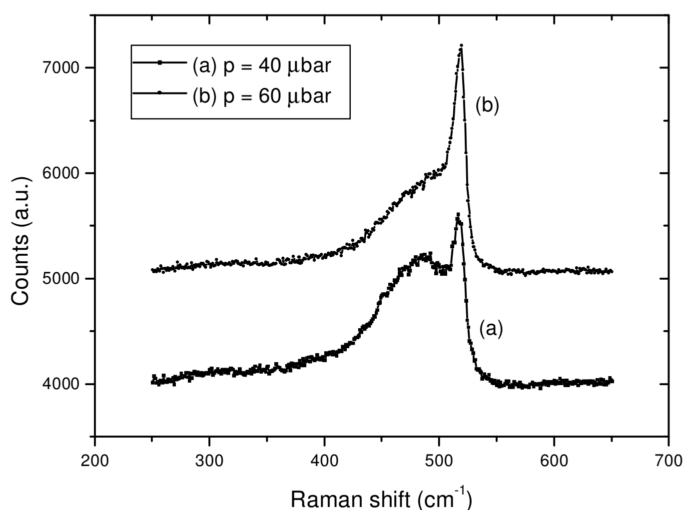

Figure 4.18. Raman shift spectra of 2 samples grown with 90% hydrogen dilution ratio at 2 different pressures. The substrate heater temperature was maintained at 410°C.

The X-ray diffraction has been used to probe into the orientation of the crystals. Samples ranging from amorphous to microcrystalline deposited with 92% hydrogen dilution ratio have been used for this effect. In figure 4.19. (a) and (b), a broad peak centred around 27.5° is only clearly visible suggesting that the films remained amorphous. In sample 4.19. (c) this first scattering peak shifts from its position towards 29° as it becomes narrower. The identification routine done using the PDF database search [81] has assigned it to silicon (111). Two additional peaks centred around 48 and 57 ° have been obtained as well. They have been assigned to silicon (220) and (311) respectively. A further increase of the deposition pressure sees a slight increase of the (111) peak in intensity as it was narrowing as well, which can be interpreted as the improvement of both the crystallinity and the crystal size (fig.4.19. (d)).

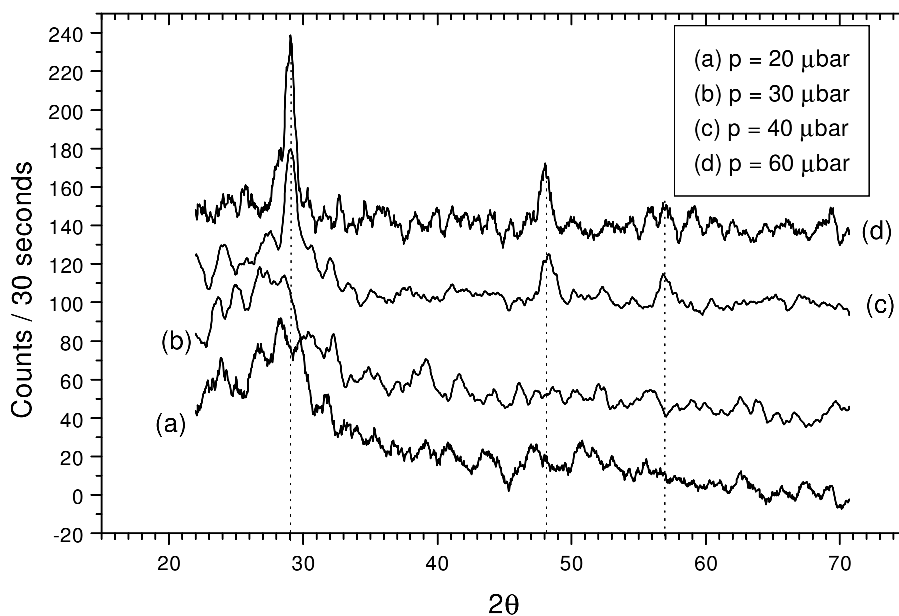

Figure 4.19. Smoothed XRD patterns of films ranging from amorphous to microcrystalline phase deposited with 92% H_2 dilution ratio at varied process pressures and a substrate heater temperature of 410°C. The graphs have been translated along the Y-axis for better visibility.

It is interesting to note that the sample represented by graph 4.19 (b) without any distinctive sign of crystallinity in XRD in the figure above has been observed to include some degree of crystallinity when Raman scattering was used. In figure 4.20, the corresponding spectrum 4.20 (b) shows a shoulder at around 515 cm^{-1}; this may be interpreted as a crystalline phase contribution superimposing on the amorphous one. A conclusion may then be drawn that Raman scattering is more sensitive to structural changes than XRD (what is also the case is that the depth dependence of the sensitivity for the two methods is completely different due to the large difference in their photon wavelengths, a higher surface sensitivity is observed for Raman scattering). As concluded in the previous heading, it is noted here also in plots 4.20 (c) and (d) that further increase in the pressure yield more crystallinity in the films.

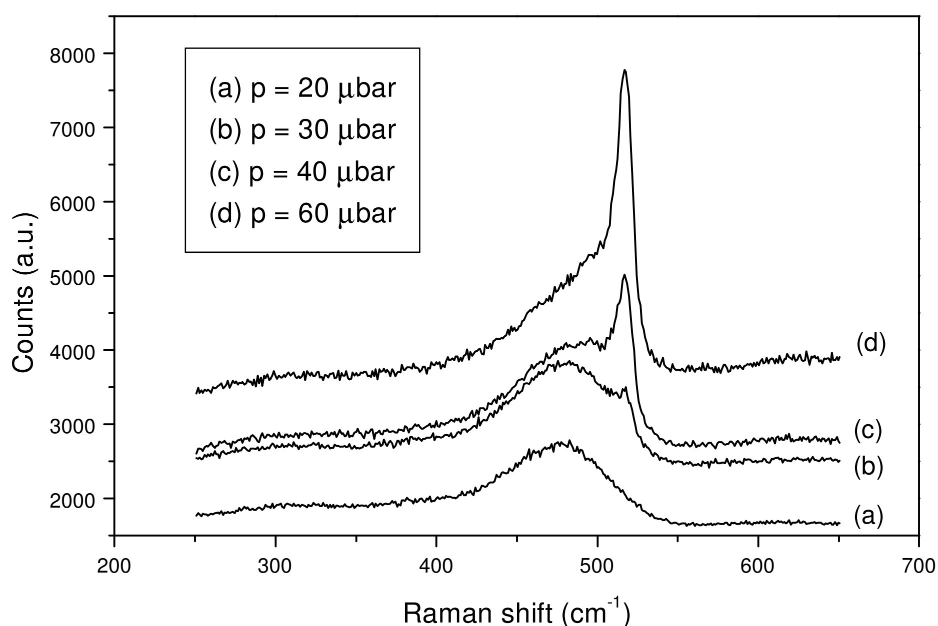

Figure 4.20. Raman shift spectra of the films grown at R_{H2} = 92% with varied process pressure; T_h = 410°C. (The graphs have been translated along the y-axis for visibility).

4.3.3. Results of the material grown at high substrate temperature.

The films studied under this heading have been deposited at a substrate heater temperature of 450°C. The substrate was placed at a distance of 1.8 cm from the filament catalyser. The methodology was the same: i.e. increase of the hydrogen dilution ratio keeping other deposition conditions fixed and increase of the deposition pressure keeping other parameters unchanged. Due to the increased reactions kinetics at high temperature, the growth and microstructure of the films deposited were observed to be different from those of the films deposited in the two previous regimes discussed above. Indeed the crystallization threshold occurred at much lower values of hydrogen dilution ratio and no or very little bonded hydrogen content has been observed in these films, as will be shown in later sections. Figure 4.21. shows the XRD patterns of samples grown at 20 μbar for

which the hydrogen dilution ratio was increased gradually from 60 to 90%. No trace of crystallinity was noted as testified by the broadening of the first diffraction peak for all the samples.

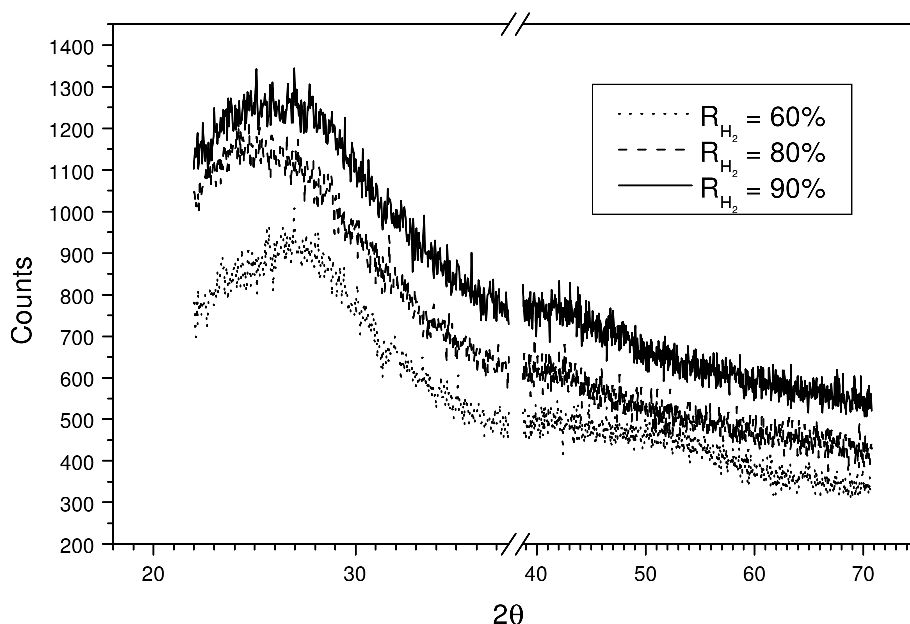

Figure 4.21. XRD patterns (raw data) of samples grown with different H_2 dilution ratios. The process pressure was kept at 20 μbar. (The graphs have been translated along y-axis for visibility).

The Raman spectra of the 60 and 80% diluted samples were well fitted by 3 gaussians peaked at around 480, 445 and 330 cm^{-1} (fig. 4.22.). These peaks correspond to the complete amorphous contribution due respectively to the phonon modes of the transverse optic (*TO*), longitudinal optic (*LO*) and longitudinal acoustic (*LA*). However the deconvolution of the Raman spectrum for the 90% diluted sample has shown an additional small peak at around 515 cm^{-1} (see appendix 6 for a detailed deconvolution step by step). This suggests a start of nucleation with inclusion of small crystals in the amorphous tissue. From these observations in both figures 4.21. and 4.22., it is clear again that XRD analysis are not sufficient to conclude on the start of nucleation, a complementary characterisation technique must be applied as far as the threshold of

crystallinity is concerned. Raman scattering is the most appropriate because it is more sensitive to small changes in the short-range order of a-Si [82]. The procedure used to evaluate the crystalline contribution was to subtract the amorphous contribution from the as taken spectrum and fit the remaining peak by two gaussians at around 510 and 520 cm^{-1} [83]. These peaks correspond to the grains boundaries and / or grains smaller than 10 nm for the first; and to large grains for the second [84].

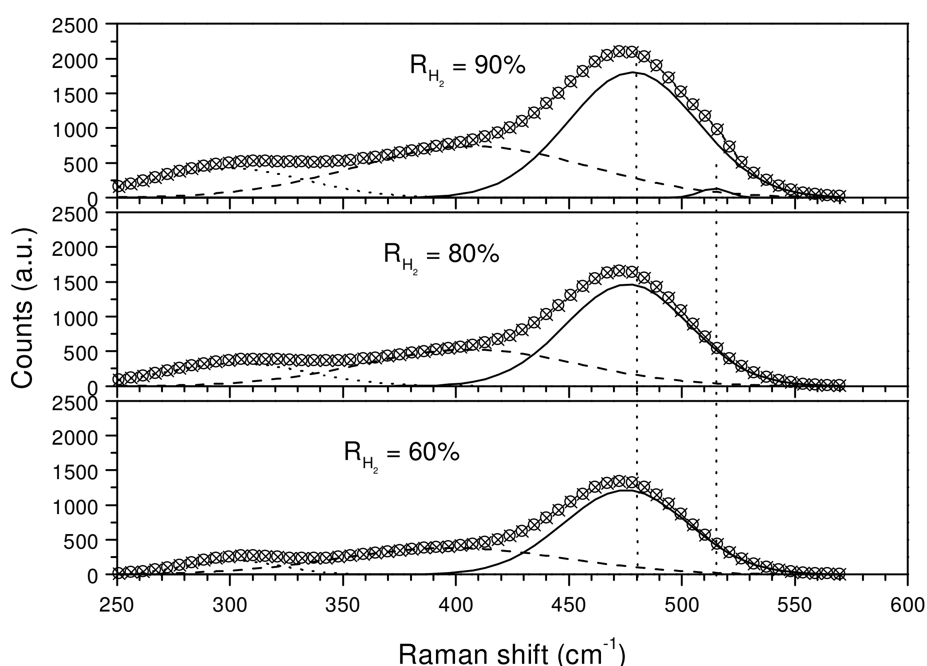

Figure 4.22. Raman shift spectra of samples grown at different hydrogen dilution ratios. The process pressure was kept at 20 μbar.

When the deposition condition was raised to 30 μbar, the threshold of crystallinity was achieved at a much lower hydrogen dilution ratio value as observed by both XRD and Raman studies; an optimum process pressure is beneficial to crystallinity since the mean free path is decreased and the subsequent secondary reaction of the atomic hydrogen (product of gas molecules on the surface catalyser) with the silane present in the chamber give more mobile radicals such as SiH_3 suitable for a crystalline phase nucleation.

Figure 4.23 shows that at this pressure a crystalline material was obtained with a dilution as low as 80%. The unexpected behaviour of the 90% hydrogen diluted grown sample (the fact that it remains amorphous despite the H_2 dilution ratio increase) could be explained by its small thickness of 640 nm while the other two samples were of the order of 1 μm. The effect of the thickness on crystallinity had been studied by J.Koh *et al.*[85]. As the hydrogen dilution is increased further, the intensity of the peaks increases which means that the amorphous tissue disappears in favour of a crystalline phase; it is also noticed from the figure that the crystals become preferentially oriented in the (111) direction. A narrowing of the FWHM of the diffraction peaks is observed as well; this fact suggests a growth of bigger crystals.

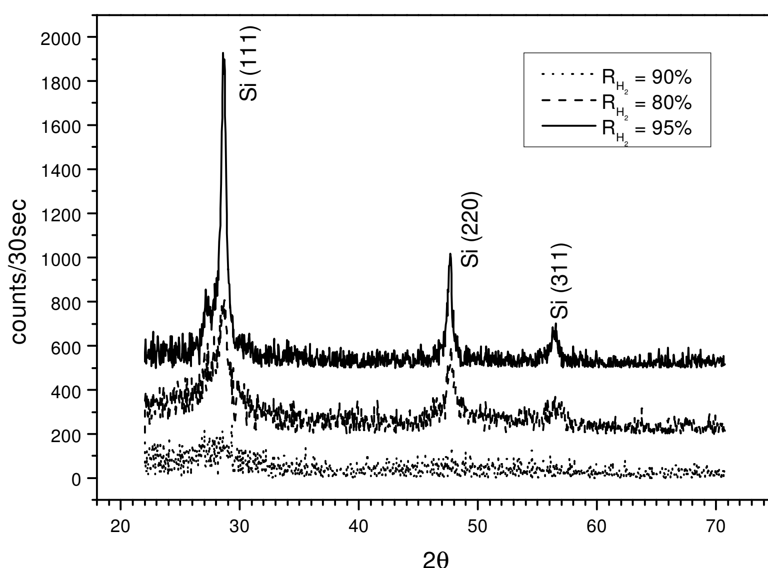

Figure 4.23. XRD diffraction of samples grown on glass substrate at varied hydrogen dilution ratio. The deposition pressure was kept fixed at 30 μbar. (The substrate contribution has been subtracted). (The graphs have been translated along the y-axis for visibility).

The Raman data agree well with these XRD results: As the hydrogen dilution was increased, the intensity of the *TO* peaked at around 480 cm^{-1} was decreasing and shifting towards higher wavenumbers while the signal due to crystallinity was improving in intensity but narrowing in width (see appendix 7). For c-Si, the Raman spectrum consists

of a sharp peak centred at 520 cm^{-1}. However our material being a mixture of different phases (amorphous, crystalline, grain boundaries), the gaussian fit of the upper section of the spectrum (> 500 cm^{-1}) shows a shift of the crystalline peak from 520 to around 517 cm^{-1}. An additional small but broader peak was obtained at around 508 cm^{-1}. This shift is explained by the small size of the incorporated crystals (table 4.2.) while the additional peak is due to the contribution of the grain boundaries. This conclusion is consistent with other published results [86-87]. Moreover the intensity of the peaks gives an estimate of the crystalline volume fraction according to [88]:

$$V_f = (I_c + I_{gb}) / [I_c + I_{gb} + y(L)\, I_a], \qquad (4.4)$$

where I_c, I_{gb} and I_a are the integrated intensities of the c-Si, intermediate and amorphous peaks respectively; $y(L)$ is the ratio of the scattering cross section for the amorphous-to-crystalline phase and has been given by Bustarret *et al.*[20] using a laser excitation wavelength of 514 nm as

$$y(L) = 0.1 + \exp[-(L/250)]. \qquad (4.5)$$

Table 4.2. Crystal sizes as calculated by the Scherrer formula from XRD

T_h (°C)	R_{H2} (%)	Pressure (μbar)	Peak position (°)	Crystal size (nm)
		40	29.1	28.8
			29.2	29.0
	92	60	48.2	14.0
			28.7	10.0
			47.7	13.0
		20	56.6	13.0
		40	29.0	40.0
410	95	60	28.8	14.0
			28.5	7.4
			47.7	13.9
		30	55.2	7.5
			28.5	9.8
			47.7	2.7
	80	40	56.4	1.6
			28.4	8.0
			47.3	4.4
	90	40	56.1	9.4
			28.5	10.0
			47.4	13.0
		20	55.9	18.0
			28.3	17.5
			47.7	11.6
		30	56.2	12.9
			28.2	8.3
			47.3	17.7
450	95	40	56.1	36.9

The calculated crystalline volume fractions are given in table 4.3. In the range of the crystals size values given in table 4.2, *y (L)* varies between 1 and 0.95 and can then be rounded off to 1 in the calculations. However these results should be taken in the context that the Scherrer formula used to estimate the crystals size is most accurate for spherical

shaped crystals. In our case they were observed to be columnar in the films with improved crystallinity. Fig. 4.24 displays two micrographs for a film at the edge of crystallinity with small crystals embedded in a large amorphous tissue (fig. 4.24(a)) and another with improved crystallinity where elongated columnar growth can clearly be observed (fig. 4.24(b)). Neththeless due to the generally small size of the crystals, this method (the use of the Scherrer formula) yields acceptable results in the present context.

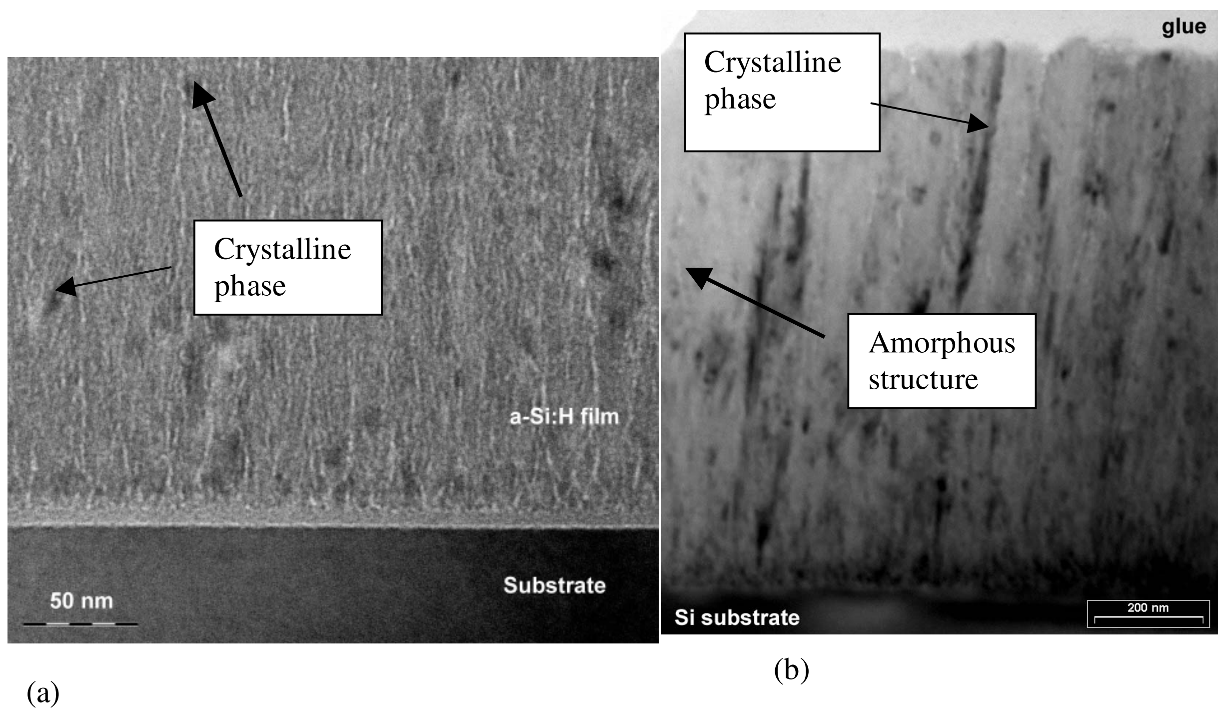

Figure 4.24. XTEM micrographs of 2 microcrystalline films on silicon substrates: (a) R_{H2} = 90 %; P = 40 µbar and V_f = 8.9 % (b) R_{H2} = 95 %; P = 20 µbar and V_f = 69.2 %. (In both cases the substrate heater temperature was set at 450°C).

Table 4.3. Crystalline volume fractions as function of the deposition conditions calculated from Raman data (results obtained from films on glass substrates).

T_h (°C)	R_{H2} (%)	Pressure (μbar)	V_f (%)
375	60-90	20	0
	95	20	< 5
410	87	20	0
		40	0
		60	6
	92	20	0
		30	15
		40	31
		60	51
	95	20	35
		40	49
		60	51
450	80	40	35
	90	20	5
		40	7
	95	10	5
		20	52
		30	60
		40	63

4.3.4. UV reflection probe on microcrystallinity

As for the UV-VIS transmission, reflection spectroscopy is a very fast and non-destructive technique widely used for optical parameter determination. Some groups [84,89-91] have used it to study crystallinity in semiconductor materials. The UV reflection spectra show peaks corresponding to the electronic transitions of crystalline silicon in the Brillouin zone at E_1 = 365 nm and E_2 = 275 nm [91]. Fig. 4.25 shows the

results obtained on a c-Si (100) wafer used in our group as a substrate reference. The details of the reflection set up used by our group have been given by Arendse [11].

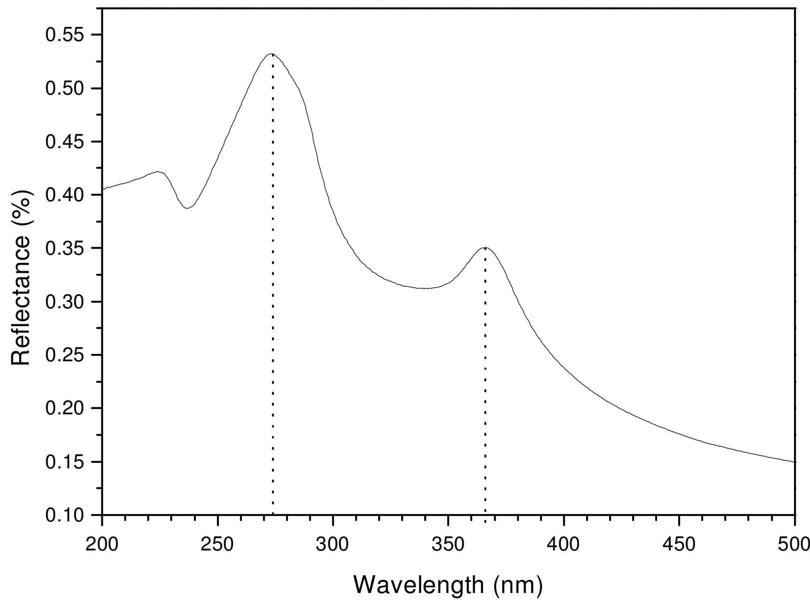

Figure 4.25. UV reflection spectrum of a c-Si substrate with the 2 electronic transition peaks.

Figure 4.26. shows the UV reflection spectra of samples grown in the amorphous to crystalline transition regime. They can be identified in table 4.3. in the series of the 410°C substrate heater temperature with a hydrogen dilution ratio of 92%. The sample deposited at 20 μbar (bottom) with a crystalline volume fraction of 0% shows only a broad peak in the region of interest while the ones with improved crystallinity (31% and 51% respectively) display a relatively sharper peak at around 280 nm. Furthermore as the crystalline volume fraction decreases, the peak amplitudes are reduced. It is observed as well that the 365 nm signals are not very well resolved for films in the transition regime.

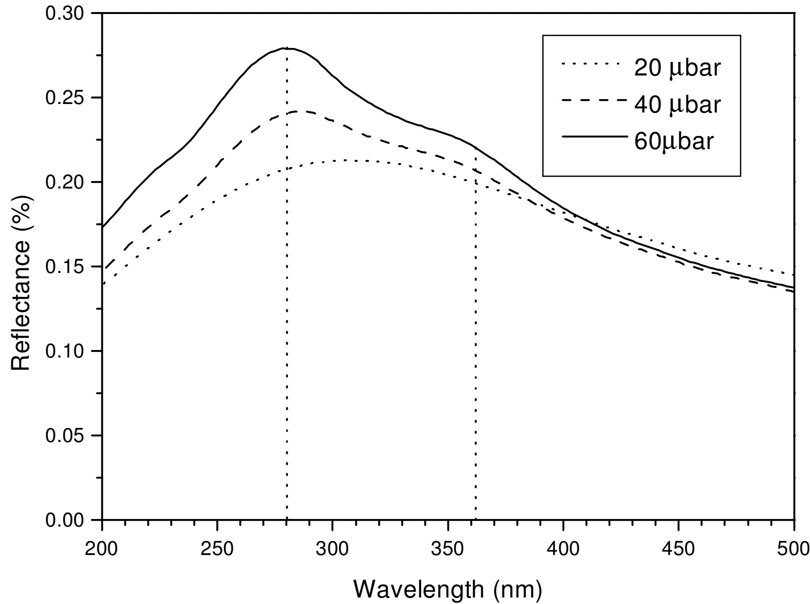

Figure 4.26. UV spectra of samples in the transition regime from amorphous to crystalline. R_{H2} = 92% and $T_{substrate\ heater}$ = 410°C.

4.3.5. Phase diagram

Given the multiplicity of the changing technological parameters in the chemical vapour deposition in general and in the HWCVD in particular, it is difficult to control the quality and the phase of the deposited layer. It is therefore useful to draw a phase diagram in order to predict both the phase and the expected opto-electrical of the material. Of course the reproducibility in HWCVD remains a big issue because, as already discussed, a slight change in the deposition conditions influences the species available for growth in the deposition chamber and therefore the subsequent produced thin film. An attempt has been made during this study to establish a phase diagram enabling us to identify where the threshold of crystallinity is occurring for specific used fixed parameters in our group.

For a preset filament temperature of 1600°C (which has been kept fixed for all deposited samples) and a distance from filament to substrate of 18 and 36 mm, a 3-step variation of

the substrate heater temperature from 375 to 450°C has been done. In this substrate temperature regime, a previous study on substrate temperature calibration ($d_{s\text{-}f}$=18 mm) [11] had found that the heater contribution to the substrate temperature was well described in the range between 100 and 600°C by the following polynomial fit:

$$T_{sub} = 4.07 \times 10^{-4} T^2_{heater} + 0.514 T_{heater} + 103.68 \quad (4.6).$$

A plot of the crystalline volume fraction against the substrate heater temperature at a fixed process pressure of 20 μbar with varied hydrogen dilution ratio (fig. 4.27.) had shown that crystallinity in the films can be induced at any of the three temperatures considered in this study but the technological deposition parameters for this effect are different; for these given three working temperatures it can deduced that:

- A hydrogen dilution ratio as low as 80 % was not enough to induce crystallinity at any of the three-substrate temperatures.
- 90% hydrogen dilution ratio was good enough to see the start of nucleation at a substrate heater temperature of 450 °C.
- Very high dilution (95%) was necessary at a low substrate heater temperature of 375 °C in order to notice the threshold of crystallinity.

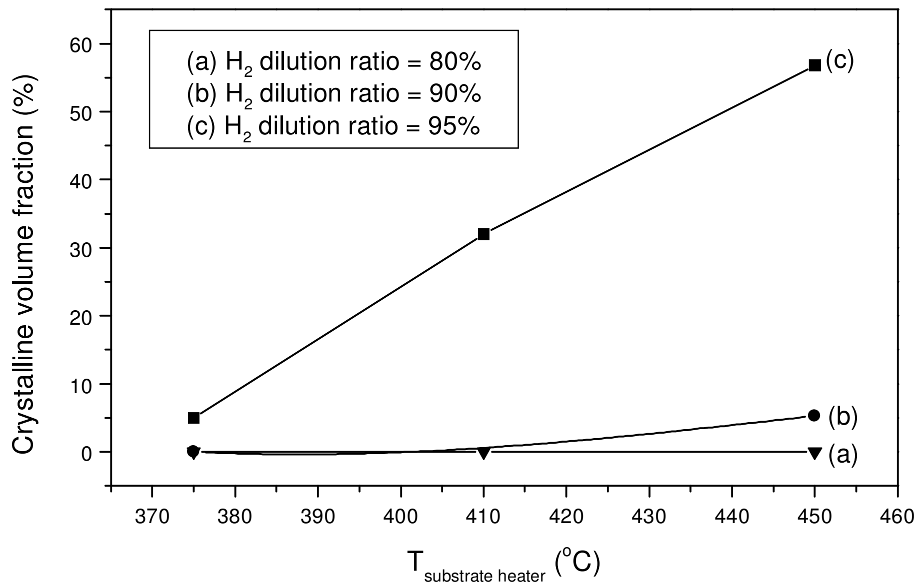

Figure 4.27. Crystalline volume fractions (from films on glass substrate) plotted against the substrate heater temperature at varied hydrogen dilution ratio. The deposition pressure was maintained at 20 μbar. (The lines are there only as guide to the eye).

We have thereafter monitored the crystalline volume fractions in the film as function of the hydrogen dilution ratio at the intermediate regime of a substrate heater temperature of 410°C. A ratio of less than 90% was good enough to yield crystallinity in the optimum pressure range from 30 – 60 μbar; the figure 4.28. below illustrates our claims.

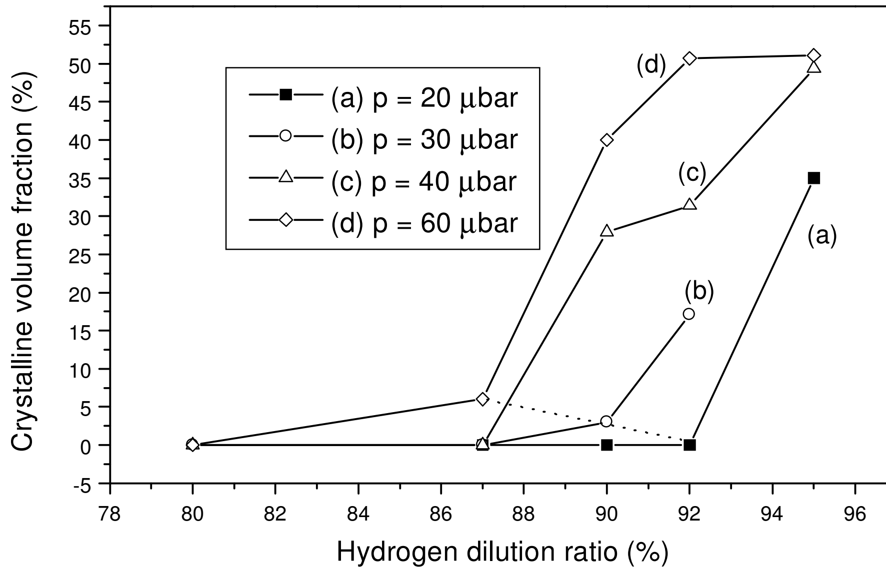

Figure 4.28. Crystalline volume fractions (from films on glass substrates) plotted against hydrogen dilution ratio with varied deposition pressure. The dotted line approximates the phase transition region. (The lines joining the data points are guide to the eye).

To complete our investigation into the threshold of crystallinity, we have plotted the crystalline volume fractions versus the process pressure at varied hydrogen dilution ratio but keeping fixed the substrate heater temperature. Our results suggest that provided a hydrogen dilution ratio of 87% and a process pressure of 60 μbar, a film on the edge of crystallinity (V_f = 6%) could be obtained. As this ratio was increased, much lower chamber pressure values were needed to see the threshold of crystallinity. The influence of the process pressure on crystallinity at different hydrogen dilution ratios can be observed on figure 4.29. At very high hydrogen dilution ratio the pressure effect seems to be not significant as it can be noticed on the trend of the upper graph displaying the data from samples deposited with 95% hydrogen dilution ratio.

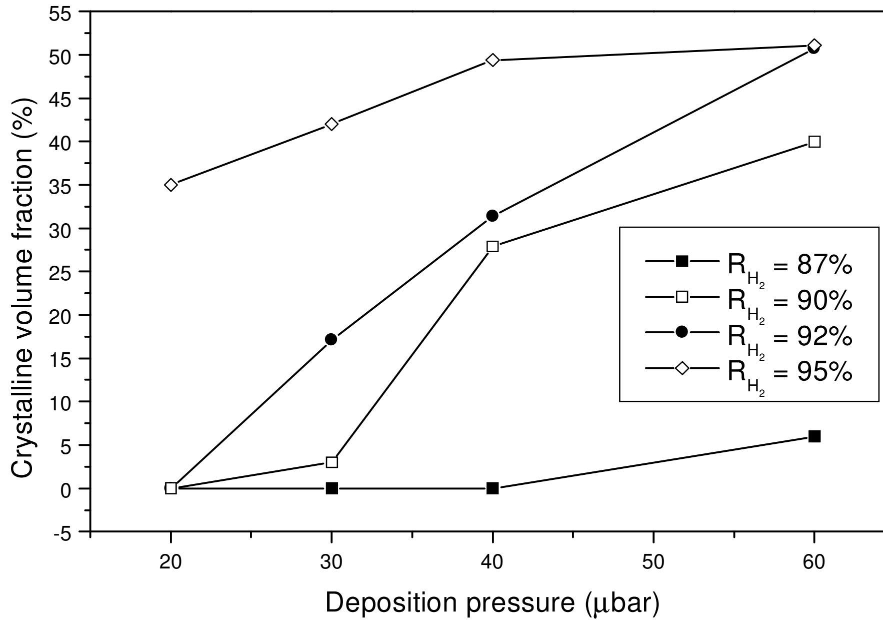

Figure 4.29. Influence of the deposition pressure on crystallinity at varied hydrogen dilution ratio and T_{heater} fixed at 410°C. (The lines joining the data points are guide to the eye).

The combination of the figures 4.28. and 4.29. leads then to the conclusion that for a Ta filament temperature of 1600°C, with a distance from the filament to the substrate of 36 mm, the threshold of crystallinity is achieved at a substrate heater temperature of 410°C with a hydrogen dilution of 87% and a process pressure of at least 60 µbar. This does not mean that the best intrinsic material is obtained at this point but it is a good reference for future depositions.

4.4. Hydrogen content and order in the material

The hydrogen content and its bonding modes in thin films have been linked to the metastability [92-93], the optoelectronic properties [94] as well as the structural ordering [95] of the non-doped layer in CVD. The hydrogen incorporation in the films has then become an important feature in a-Si: H based devices. We have studied the incorporation

and content of hydrogen in the films using Fourier transform infrared spectroscopy (FTIR) and elastic recoil detection (ERD).

4.4.1. Hydrogen content in films grown at high substrate temperature

As in the previous sections, by high substrate temperature we refer to the films grown at a heater substrate temperature of 450°C. The films have been deposited with pressures ranging from 10 to 60 µbar using a mixture of hydrogen into silane with dilutions ranging from R_{H2} = 60 to 95%. The flow of hydrogen was fixed at 30 sccm (standard cubic centimetre per minute) and the silane flow was varied according to the required dilution. The distance from the filament to the substrate was 18 mm. Studies done by FTIR on the samples deposited in this regime have detected little or no bonded hydrogen. Instead excessive oxygen has been noted especially in the films deposited with high hydrogen dilution ratio. Figure 4.30 displays the FTIR spectra of films deposited at this temperature with in fig. 4.30 (a) a fixed pressure of 20 µbar and varied hydrogen dilution ratio, and in fig.4.30 (b) a fixed hydrogen dilution ratio of 90% with the deposition pressure as the changing parameter. Regardless of the technological process parameters it appears clearly that oxygen has been incorporated suggesting a porous material. From fig.4.30 (a) it is moreover observed that samples with higher hydrogen dilution contain less bonded hydrogen but the oxidation peak is enhanced; as it has been shown above those films contain more crystalline regions. From fig.4.30 (b) we notice that the bonded hydrogen content is reduced to zero with the increase of the pressure but the oxidation peak subsists. This result is in disagreement with the usual increasing trend of the hydrogen concentration with the pressure in a-Si: H growth; Raman studies has shown that those samples were in the phase transition which presumably, with the appearance and growth of the crystallites, induces nano-voids where atomic hydrogen will be trapped and combine in molecular form [3].

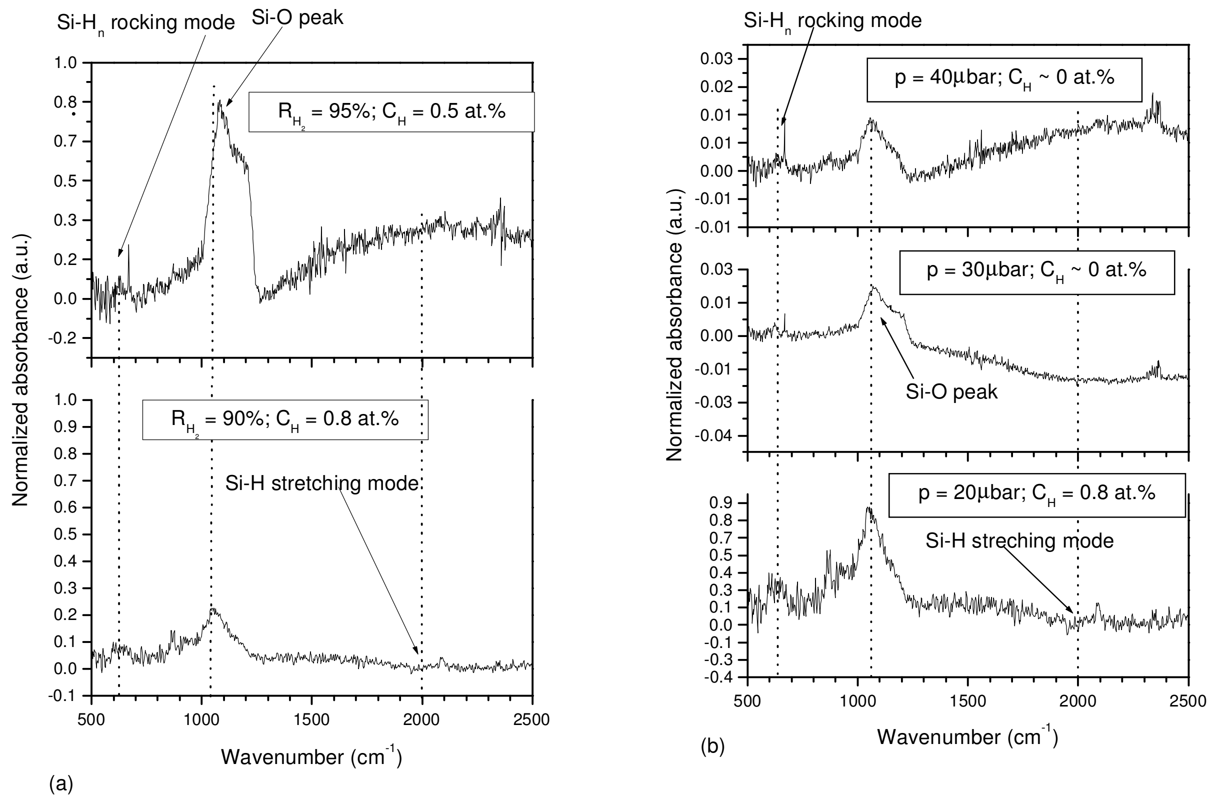

Figure 4.30. FTIR spectra of films grown at the substrate heater temperature of 450°C with filament –substrate spacing of 18mm. (a) pressure fixed at 20 µbar; (b) hydrogen dilution ratio maintained at 90% and the pressure taken as a changing parameter. The dotted lines indicate the position of the expected main molecular vibration modes for silicon.

The lack of or little bonded hydrogen in the films grown in this regime may be attributed to the combination of three factors:

1) the closeness between the substrate and the filament which might have amplified the hot wire radiation effect,
2) the high temperature of the substrate which enhanced the desorption process, and
3) the depletion of the silane gas in the chamber.

To test the possibility of the first hypothesis, a test sample has been prepared at the same heater substrate temperature of 450°C with a filament-substrate distance doubled to 36mm and indeed an increased bonded hydrogen content was obtained as it can be seen on fig. 4.31. The reduced spread of the oxidation peak is seen here as an indication of the improvement of the microstructure of the film corresponding to the upper graph (b) in fig.4.31. We postulate that by increasing the distance from the filament to substrate while keeping constant the same high substrate temperature, the surface reaction rate of adsorbed H-atoms remains the same but the influx of growth precursors is reduced. This prevents the trapping effect of H-atoms in voids where they group in molecular form. Heintze *et al.* [96] had proposed that in order to avoid the trapping of H-atoms in voids, the surface reaction rate of adsorbed H-atoms has to be faster than the influx of growth precursors. The evidence of the reduction of the precursors in the film represented by graph (b) in the figure is given by the drastic drop of the growth rate from 31-nm/min.for samples 4.31. (a) to 12 nm/min in sample 4.31. (b).

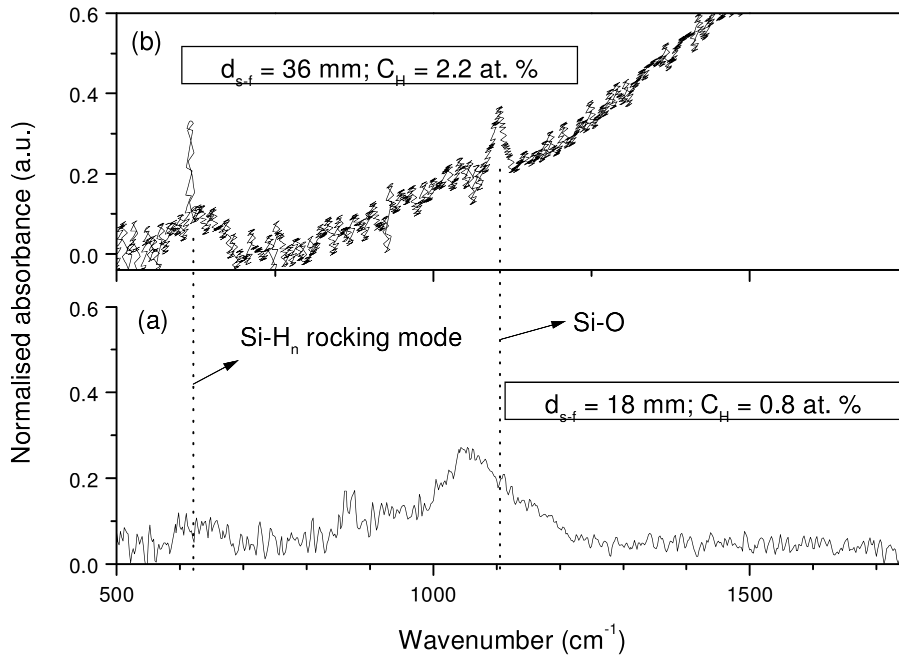

Figure 4.31. FTIR spectra of two films grown at the same T_h = 450°C and same hydrogen dilution of 90% with different spacing filament-substrate. (a) $d_{s\text{-}f}$ = 18 mm and total flow rate of 60 sccm (b) $d_{s\text{-}f}$ = 36 mm and total flow rate of 33sccm.

The second postulate is in agreement with the results of Feenstra [3] and the hydrogen density-of-states model proposed by Santos *et al.* [93]. We recall that the hydrogen chemical potential in both the gas phase and in the film should be equal, and since the chemical potential increases in the film with the substrate temperature, it is obvious that the ratio in the second term of the right hand of the equation (2.9) must decrease. The occupancy of the traps (N_H in the formula) is decreased at higher substrate temperature. It seems however that this only applies to the hydrogen in shallow interstitial traps and on deep dangling bonds but not to the less mobile molecular hydrogen, which might reside in the voids. We have performed ERD studies using a 3 MeV He beam. The light hydrogen in the sample was recoiled and detected as explained in section 3.5. Our investigations have detected hydrogen throughout the samples thickness. For illustration purpose, we present in fig.4.32 the hydrogen profile as function of depth in 3 samples deposited at 30 µbar with varied hydrogen dilution ratios.

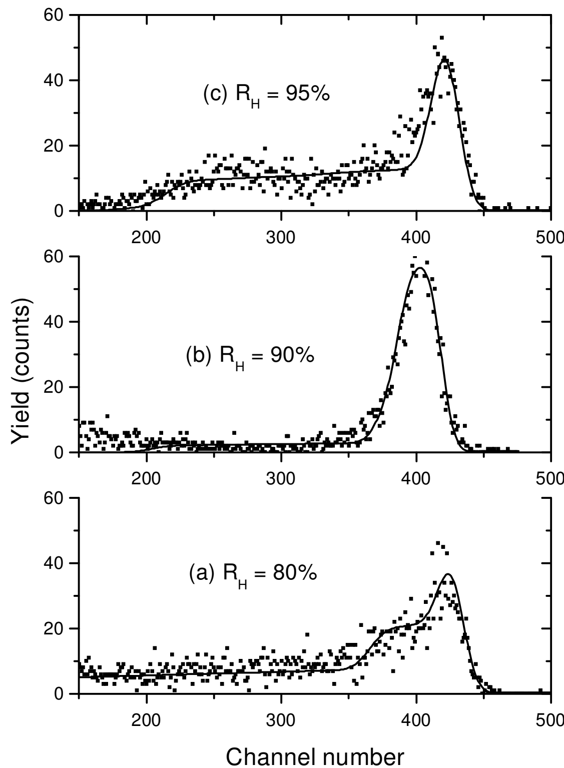

Figure 4.32. ERD spectra of films deposited at 30 μbar with varied hydrogen dilution ratios. The data points represent the as taken spectrum while the solid line gives the simulated spectrum.

It is noticed on the graphs that there is an appreciable amount of hydrogen in the regions near the surface. This may suggest that the material is highly porous and leaves a path to water vapour molecules. In order to estimate the hydrogen content detected in ERD, the films have been divided in different layers depending on the hydrogen profile throughout the thickness. The reported hydrogen content values from ERD data are the average of all the contributing layers in the films. In the averaging process however a same amount of surface hydrogen has been ignored for all the spectra; it was calibrated using a bare c-Si spectrum. An average percentage of 0.81 and 0.97% has been calculated for sample 4.32.

(a) and (c) respectively. For sample 4.32. (b) (the thinnest of the three) only 0.74 % has been noted and the useful statistics above zero on the y-axis have been mainly observed in the near-surface regions. For films grown in the same regime but at an increased deposition pressure the same profile has been observed. Taking into account however that they comprise more crystalline structures, it is expected that more hydrogen molecules will be trapped between grain boundaries and within voids. Fig. 4.33 displays ERD spectra of such samples deposited at 40 μbar with 3 varied hydrogen dilution ratios.

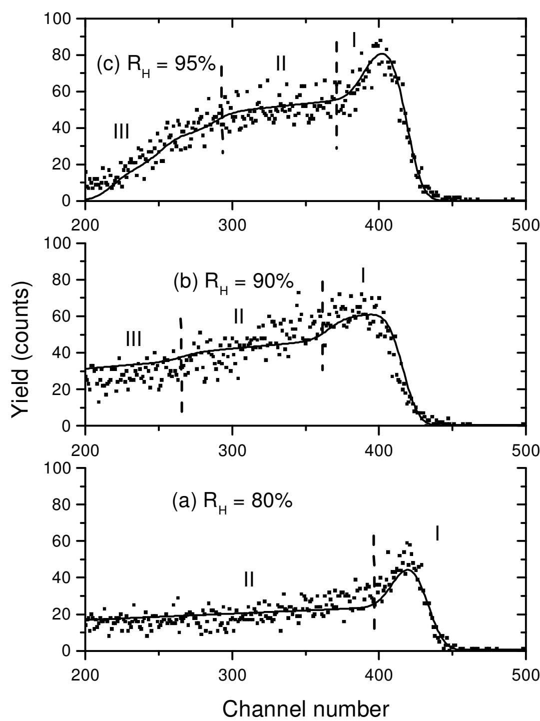

Figure 4.33. ERD spectra of samples deposited at 40 μbar with varied hydrogen dilution ratios. The solid lines represent the simulated spectra.

The average hydrogen content has been calculated to be 1.14; 2.99 and 3.35 % for the samples in fig. 4.33 (a), (b) and (c) respectively. While the hydrogen is evenly distributed in the bulk of sample 4.33. (a), it is noticed that samples 4.33 (b) and (c) can be subdivided into 3 main regions according to the hydrogen profile as detected in ERD: the near-surface region I and two other regions II and III with different slopes where the uniformity of hydrogen distribution is observed. Since the hydrogen is linked to the order in the films, it is expected that different patterns in microstructure will be observed in regions with different hydrogen content. This is an indirect evidence of the non-uniformity in the crystalline phase distribution in nanocrystalline material. Fig. 4.24 (a) had shown the XTEM micrograph of the film whose ERD pattern is given by fig. 4.33 (b). In fig. 4.24. (b) a micrograph of a film deposited at very high dilution and containing up to 69% of crystalline fraction was displayed (the same micrograph is reproduced in fig.4.34). The non-uniformity in crystalline regions is evident: The selective dark columnar growth regions (sign of crystallinity) are observed towards the surface; the dark regions near the interface with the c-Si substrate are due to the influence of the underlying c-Si substrate. Its ERD spectrum is shown in fig. 4.34. Our data have not however deduced any clear quantitative relationship between the crystalline volume fraction and the hydrogen content detected in ERD. This will be more unlikely if one takes into account the fact that the crystalline volume fractions data are obtained from Raman spectroscopy which probes into the first 100 nm thickness while the ERD hydrogen content is averaged over the whole thickness. The present analysis can then only be qualitative in correlating the respective information obtained from ERD and XTEM. This correlation becomes even clearer if one compares the ERD-hydrogen profile of fully amorphous films to the profile in films with large amounts of crystallinity, as is shown in figure 4.35. It is seen from the graphs that, moving from samples (a) to (d), the hydrogen is first observed uniformly distributed throughout the bulk, but becomes progressively unevenly incorporated from the surface layer to the substrate interface. The near-surface hydrogen component is also more clearly distinguishable from the one in the bulk with the increase of crystallinity. We postulate that it is due to the surface roughness as the films have been found to crystallize more moving from (a) to (d).

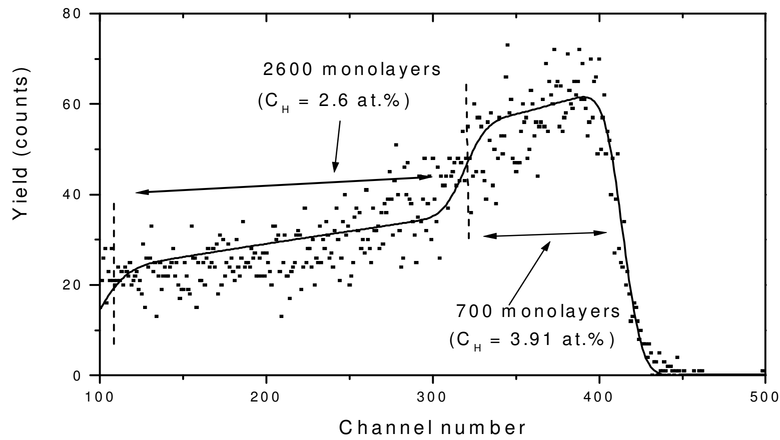

(a)

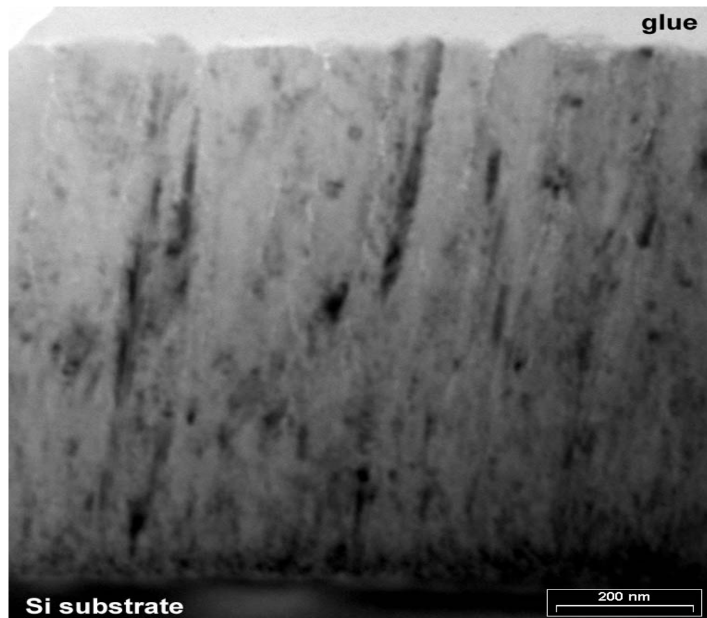

(b)

Figure 4.34. (a) ERD spectrum of a 95% hydrogen diluted film ≈ 0.6 µm thick; P = 20 µbar with a crystalline volume fraction of 69.2% and ERD-hydrogen content of 3.06%. The solid line represent the simulated spectrum while the dashed lines estimate the boundaries of different regions where the hydrogen detected in ERD is unevenly distributed. (One monolayer approximates an areal density of 10^{15} atoms/cm^2; We are assuming here a mainly Si network and for Si, 1E15 at.cm^{-2} ≈ 0.2009 nm).
(b) The 4.24. (b) micrograph is reproduced.

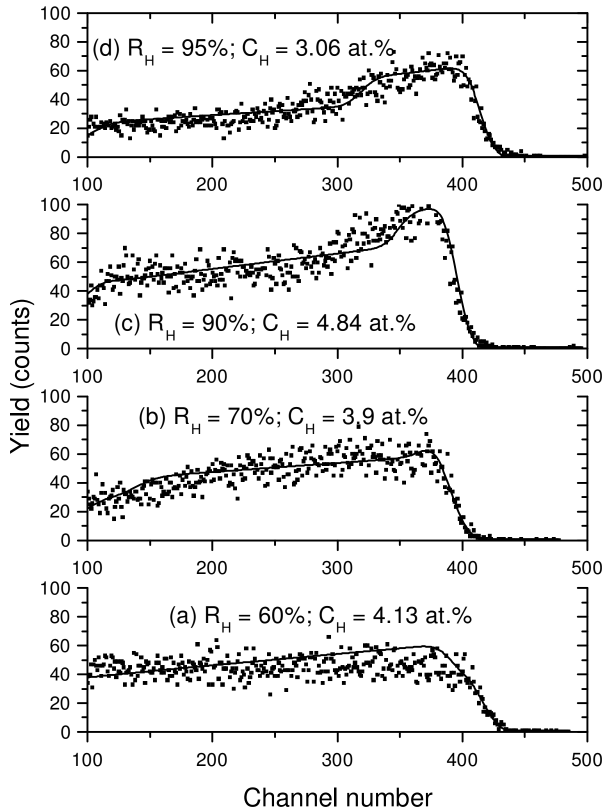

Figure 4.35. ERD spectra for films ranging from amorphous to microcrystalline phase on c-Si substrate. The deposition pressure was 20 µbar. (a) V_f = 0%; (b) V_f = 0%; (c) V_f = 4.7%; (d) V_f = 69.2%. The solid lines show the simulated spectra.

4.4.2. Hydrogen content in films grown at moderate substrate temperature

The failure to obtain bonded hydrogen in most of the films processed at high substrate temperature and the high oxygen incorporated in them had prompted us to lower the deposition substrate temperature. As mentioned earlier in table 4.1, the substrate heater temperature was set at 375 and 410°C and in order to minimise the filament radiation, the distance between the substrate and the Ta wire was increased to 36 mm. With these

deposition conditions, bonded hydrogen content up to 7 at. % has been calculated in FTIR spectroscopy. Fig. 4.36 displays the FTIR spectra of samples prepared at the substrate heater temperature maintained at 375°C, the pressure at 20μbar and the hydrogen dilution ratio was taken as a changing parameter.

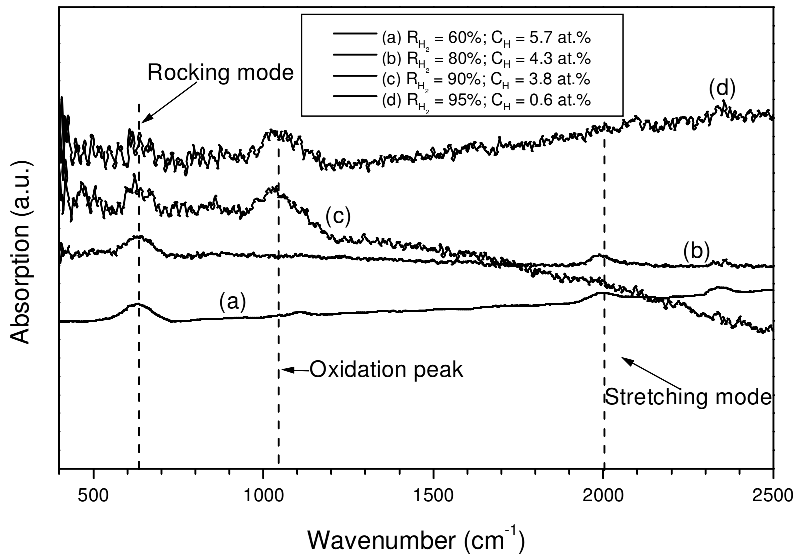

Figure 4.36. FTIR spectra of films grown with T_h = 375°C; P = 20 μbar at different values of hydrogen dilution ratio. (The graphs have been translated along the y-axis for visibility).

It transpires from the figure that both the stretching and rocking mode are obtained in samples 4.36 (a) and (b) deposited with moderate hydrogen dilution (60 and 80% respectively). As the dilution was increased above 90% (samples 4.36 (c) and (d)), the stretching peak at 2000 cm^{-1} disappeared and the 630 peaks remained, but attenuated. This implies that the monohydride coordination was almost completely suppressed in the bulk and only dangling bonds on the grains boundaries are thus passivated. The microstructure parameter R^* which is a measure of the inhomogeneity in the film was found to increase (see table 4.4). Furthermore a new peak was observed at around 1040 cm^{-1}. We have assigned it to the post oxidation process. Although both XRD and Raman

spectroscopy have failed to notice the start of nucleation in the film 4.36 (c), we believe that in samples 4.36 (c) and (d) this redistribution of hydrogen reveals that important changes in microstructure are occurring. The ERD studies of the same samples in fig.4.37 have shown that the hydrogen was uniformly spread throughout the thickness; in films (c) and (d) of fig.4.37 it is noticed that the shape of the spectra is strongly influenced by the hydrogen detected in the regions close to the surface due to the fact that the films themselves were grown very thin (208 and 113 nm respectively).

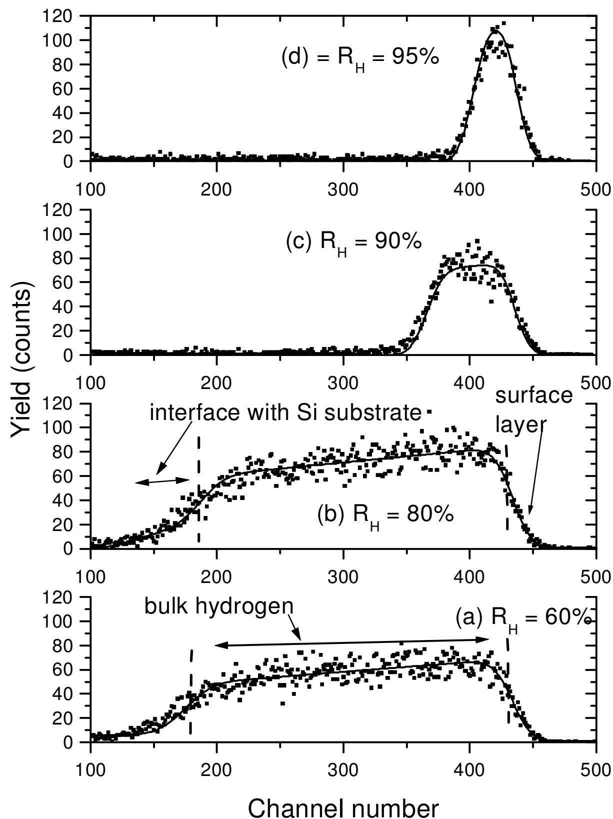

Figure 4.37. ERD simulated spectra of films grown with T_h = 375°C; p = 20 µbar at different values of hydrogen dilution ratio.

Table 4.4 gives the hydrogen content values calculated in both ERD and FTIR alongside with the microstructure values for the samples. The ERD values are obtained from the simulation process in SIMNRA, which has an accuracy of 1% provided that the input data are exact. The 95% hydrogen diluted sample displays an R^* approaching 1; this may indicate that the sample is at the threshold of crystallinity and the start of nucleation has a detrimental effect on the microstructure. This sample, as it will appear in section 4.5.2, has poor electronic properties.

Another fact to highlight from this table is the huge disparities between the bonded hydrogen content calculated from FTIR and the average values calculated from the hydrogen detected in ERD for the samples (a) and (d). The ERD spectrum of sample (a) as displayed in fig.4.37 above shows that the hydrogen has been detected in the bulk without any near - surface component; this makes us believe that the hydrogen might have evolved from the sample given the fact that this measurement was done some time after the FTIR. In sample (d) as mentioned above, the sample is at the edge of crystallinity and with the appearance of nanocrystals in the amorphous network, molecular hydrogen (non detectable by FTIR) might have been trapped within the grains boundaries and / or within voids. This might explain the higher value given by the recoiled hydrogen in ERD.

Table 4.4. Hydrogen content calculated in ERD of the samples labelled in fig.4.36.

H_2 dilution	(a) R_{H2} = 60%	(b) R_{H2} = 80%	(c) R_{H2} = 90%	(d) R_{H2} = 95%
C_H (ERD) (at.%)	2.16	3.29	3.4	4.8
C_H (FTIR) (at.%)	5.7	4.3	3.8	0.6
R^* (a.u.)	0.21	0.13	0.19	0.79

The deposition at a substrate heater temperature of 410°C has yielded films ranging from amorphous to microcrystalline phase. This wide range provides a much broader view of the influence of phase changes on the hydrogen content in the films as it has been

observed in FTIR. Table 4.5 gives an overall summary of the results obtained in this regime.

Table 4.5. Bonded hydrogen content (C_H –FTIR) versus crystallinity.

Pressure(μbar)	R_H (%)	V_f(%)	C_H (at.%)	R^* (a.u.)
20	87	0	4.7	0.4
	92	< 2.5	2.2	0.7
	95	35	1.8	1
30	80	0	5.5	0.1
	87	0	4.1	0.35
	92	15	1.4	0.72
40	80	0	6.7	0.14
	87	0	4.1	
	92	31	2.8	0.49
	95	49	1.3	1
60	80	0	7.0	0.4
	87	6	4.3	0.25
	92	50	3.3	0.57
	95	51	1.9	1

It transpires from the table above that the bonded hydrogen content decreases with the increase of crystallinity in the films while the microstructure value R^* is increasing. This means that with the increase of crystallinity, the bonding of hydrogen shifts from mono to polyhydrides situated mainly on grain boundaries. Moreover, as previously concluded that the hydrogen dilution influences the crystallinity, a direct correlation here also was noticed between the hydrogen dilution ratio and the bonded hydrogen content. The combination of the results given by the table in one graph yields a phase change diagram similar to the one displayed in figure 4.28. Figure 4.38 extracts the phase transition region from the graph-plots of the bonded hydrogen content against the hydrogen dilution at varied deposition pressures.

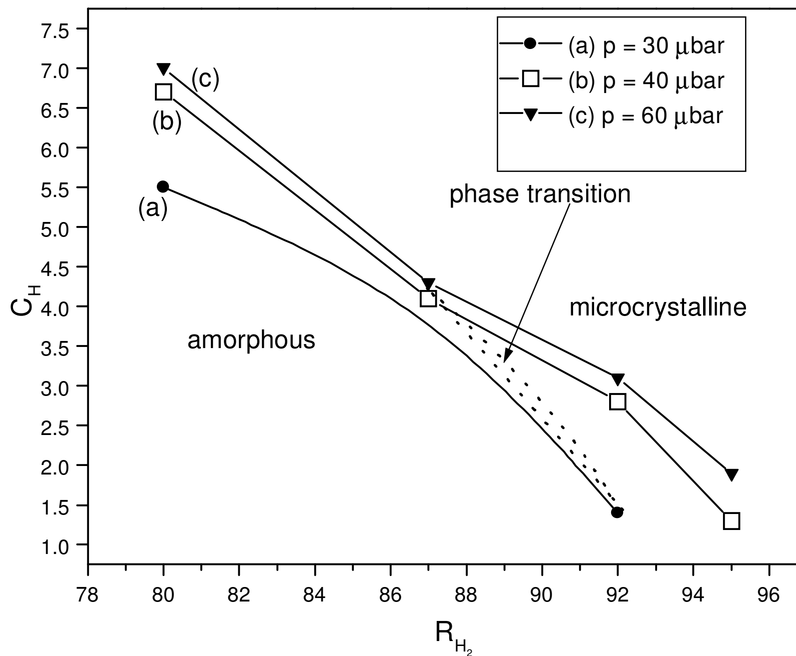

Figure 4.38. Bonded hydrogen content (from FTIR) versus the hydrogen dilution ratios at varied process pressure. The substrate heater temperature was maintained at 410°C and the distance from the filament to the substrate was fixed to 36 mm. (The lines joining the data are guide to the eye).

From the phase diagram above it is observed that the passage from a disordered amorphous (lack of long-range order) to an ordered crystalline phase is accompanied by a sharp decrease in the content of bonded hydrogen. This can be explained by the beneficial effect of the hydrogen dilution in the reactant gases; the growing surface is etched from the defective weak Si bonds and the rearrangement of the network is achieved due to the interaction between the atomic hydrogen and the surface either by breaking or inserting into the weak Si-Si bonds as earlier reported by Mahan *et al.* [18].

4.4.3. Ordering in amorphous Si films

It is known that, unlike in c-Si, the Si-Si-Si bond angle takes in the case of amorphous silicon a distribution of values described by a spread $\Delta\theta$ of about 9° from the tetrahedral value of θ equal to 109° [56]. The minimum elastic potential energy corresponding to the relaxed structure is achieved when $\Delta\theta$ is about 7° with the relative spread in bond length ($\Delta r / r$) of about 1 % [56]. From the Raman spectrum the bond angle variation can be estimated using the results of numerically constructed empirical models: Beeman *et al.* [53] have proposed a linear relationship between the width of the *TO* mode (Γ) and the angular disorder $\Delta\theta_b$ which increases as the Raman intensity spreads over a wider range.

$$\Gamma = 15 + 6\Delta\theta_b \qquad (4.7)$$

The Beeman model has a limitation in the range $0° < \Delta\theta_b \leq 6.6°$ corresponding to the phase transition region from crystalline to amorphous because of the discontinuous change in topology, it was not possible for the authors to construct homogeneous models in this region.

R.L.C. Vink *et al.* [97], using a 1000-atom configuration, have arrived to a similar linear relation

$$\Gamma = 18.4 + 6.6\,\Delta\theta \qquad (4.8)$$

and they succeeded also to link the *TO* mode frequency ω_{TO} (in cm^{-1}) to the spread in mean bond angle $\Delta\theta$.

$$\omega_{TO} = -2.5\,\Delta\theta + 505.5 \qquad (4.9)$$

While for the Beeman model the $\Delta\theta_b$ range variation is between 7.7 and 11°, The Vink calculations yield values between 10 and 13° for the specimens they have respectively used. Experimental values of $\Delta\theta$ based on the radial distribution function (RDF) of a-Si,

obtained in neutron diffraction studies, range from 9.9 to 11.0°. All these considerations taken into account show that the topic is still open for improvement and the reported results should be assessed only based on the model used by the experimentalist.

The two first models (equations (4.7) and (4.9)) have been applied to our Raman data in order to assess the order in the films found to be amorphous by both Raman and XRD. Illustrative results of films deposited at a fixed pressure of 20 μbar in different regimes are given in table 4.6. It is clear from the table that our data are respectively close to the lowest edges proposed by the 2 models. The result agrees well with the material under examination since the films lie on the threshold of crystallinity and thus the medium range order (MRO) is enhanced. However due the uncertainties attributed mainly to the fitting and deconvolution procedure of the Raman peak, some of the calculated values have been found below the lowest minimum of the proposed ranges for a-Si:H.

Table 4.6. Calculated bond angle variations for films on the edge of crystallinity by the models proposed respectively by Beeman and Vink.

T_h (°C)	R_{H2} (%)	$\Delta\theta_{Beeman}$ (°)	$\Delta\theta_{Vink}$ (°)
375	60	7.5	10.0
	80	6.4	10.0
	90	6.4	10.0
	95	6.8	9.6
410	87	7.2	10.0
	92	7.2	10.0
450	60	7.3	9.7
	80	6.6	11.3
	90	7.05	10.3

4.5. Electrical properties

The films have been characterized by dark and photoconductivity (σ_d and σ_{ph} respectively) in order to probe their response to AM1.5 light. A detailed solar spectrum – Air Mass 1.5 can be found in [98] in the range of wavelengths 0.295 – 2.537 μm. The

samples under investigation have been observed to have different photoresponse in different regimes of deposition.

4.5.1. Photoresponse of the films grown at high temperature

As in the previous sections, by high temperature, we refer to the films deposited at a substrate heater temperature of 450°C. A summary of the results obtained on the films grown in this regime is given in table 4.7 where the photosensitivity is the ratio between the photo- and dark conductivity (σ_{ph} / σ_d).

Table 4.7. Dark and photoconductivity of films deposited at a substrate heater temperature of 450°C. The applied voltage = 100 V; the evaporated Ag contacts were separated by 0.5 mm and 20 mm in width and length respectively.

R_{H2} (%)	Pressure (μbar)	Dark current (A)	Light current (A)	Photosensitivity
90	10	6.68E-06	7.62E-06	1.14
95	10	3.30E-05	3.61E-05	1.09
60	20	1.14E-07	3.51E-07	3.08
80	20	6.68E-10	1.25E-07	187.13
90	20	1.03E-06	1.21E-06	1.17
95	20	1.14E-06	1.66E-06	1.46
90	40	1.72E-07	3.01E-07	1.75
95	40	1.66E-04	1.78E-04	1.07

The results in the table above show that the values of the current are relatively high in dark and low under illumination when compared to the published ones for an intrinsic device quality; the subsequent photosensitivity values are very low. As explained in the previous section, these films are characterized by a lack of bonded hydrogen coupled with a high content of oxygen. The excessive content of oxygen may explain the high value of the dark current because the oxygen impurities are known to act as *n*-type dopant

[99]. The lack of bonded hydrogen may explain moreover the observed low values of the photocurrent as the dangling bonds are not fully passivated and act as efficient recombination centres in the forbidden band. The highest photoresponse in this series has been obtained for the 80 % hydrogen diluted film laying just before the threshold of crystallinity. The figure 4.39. shows the profile of the two types of current as function of the hydrogen dilution ratio at a fixed deposition pressure of 20 μbar.

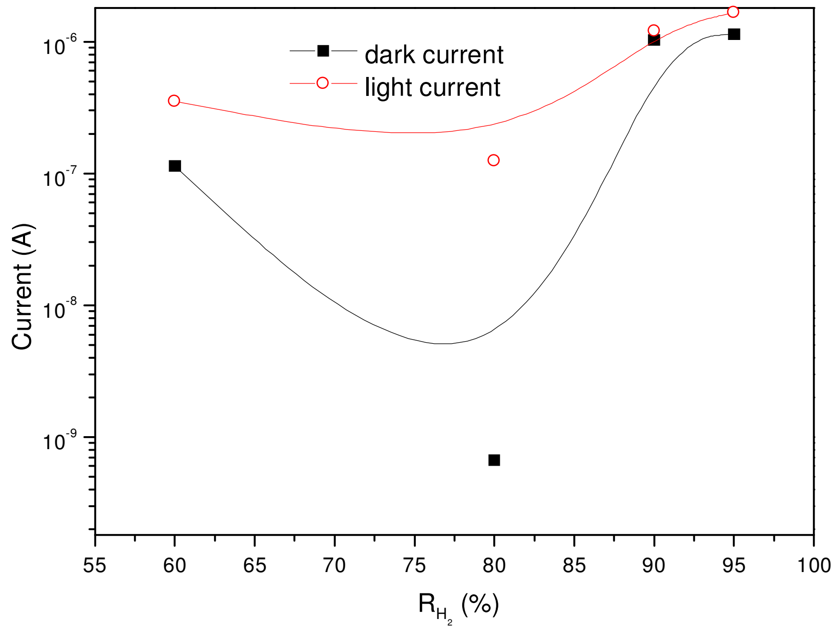

Figure 4.39. Dark and photocurrent vs. hydrogen dilution ratio in logarithmic scale for films deposited in the high T_h regime with a short $d_{s\text{-}f}$ of 18 mm. The B-Splines are there only for eye guide.

The highest dark currents are observed in case of the films grown at very high dilution ratios, consistent with the most defective material as these films were observed in the previous sections to incorporate more crystalline regions (table 4.3.) and high oxygen content (fig. 4.30. (a)). The poor electronic response in this regime of deposition has driven us to lower the substrate temperature and to increase the distance between the substrate and the filament.

4.5.2. Photoresponse at low substrate temperature

The films discussed under this heading have been deposited at a substrate heater temperature of 375°C and the distance between the substrate and the filament was fixed at 36 mm. As it has been pointed out by table 4.3., from Raman spectra a detectable crystalline fraction was only present in the layers deposited using very high hydrogen dilution ratio. Furthermore on figure 4.36, FTIR studies have revealed an appreciable amount of bonded hydrogen. Their microstructure is then different from the 450°C series described above. Table 4.8. displays the typical dark and photocurrents obtained in this regime at a chamber pressure of 20 µbar with varied hydrogen dilution ratio.

Table 4.8. Electrical characteristics for films deposited at a substrate heater temperature of 375°C and a chamber pressure of 20 µbar.

R_{H2} (%)	Dark current (A)	Photocurrent (A)	Photosensitivity
60	2.00 E-11	6.32 E-07	31600
80	5.63 E-10	8.71 E-06	15471
90	2.97 E-08	7.52 E-07	25.3
95	1.26 E-08	3.92 E-08	3.11

It clearly appears from these results that the material deposited at low substrate temperature displays better electronic properties. Moreover we observe that the dark- and photoconductivity (and thus the photoresponse) show a trend that is consistent with the H_2 dilution [100-101]: the increase of the H_2 dilution leads to:

- higher dark conductivity
- smaller photoconductivity
- decreasing photoresponse

The combination of the information contained in figure 4.36. and table 4.8. correlate the photoresponse to the hydrogen content measured by FTIR (see fig. 4.40.). The electronic properties thus generally degrade with the decrease in hydrogen content.

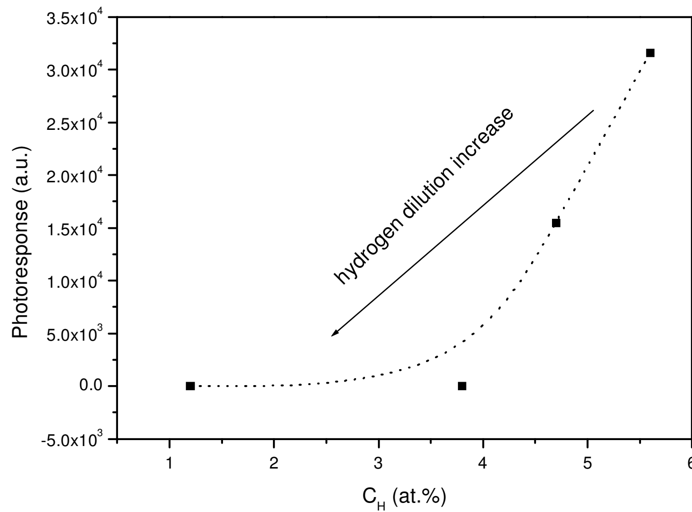

Figure 4.40. Photoresponse versus bonded hydrogen content for films deposited at a substrate heater temperature of 375°C.

A dramatic drop of the photoresponse towards very low values is however observed for films prepared with high hydrogen dilution ratio (R_{H2} = 90% and onwards) with a hydrogen content (C_H) of less than 3.8 at. %. Since it had been previously demonstrated that a material of good quality could be obtained with hydrogen content less than 1 at. % [18], the low content in hydrogen cannot be accounted for this shrinkage; we attribute it instead to the oxygen incorporation in the films (see graphs (c) and (d) in fig. 4.36.). We suspect also that small microcrystals are forming as this process is usually accompanied with a deterioration of the electronic properties; they recover eventually when the crystalline ratio exceeds 40% for microcrystalline silicon provided that the material is compact and does not contain excessive amounts of oxygen.

4.5.3. Electronic properties at moderate substrate temperature

4.5.3.1 Photoresponse

The optimum substrate heater temperature in this study has been identified in between those two extreme deposition regimes described in the above sections. Indeed with a substrate heater temperature fixed at 410 °C and keeping the substrate-filament distance at 36mm, improved electronic properties have been attained. These films, as already mentioned in the phase transition section, cover a large range from amorphous to microcrystalline material. Table 4.9 displays the typical dark and photoconductivity values obtained in case of an applied voltage of 100 V at room temperature.

Table 4.9. Dark – photoconductivity and photoresponse data for two sets of samples deposited at 40 and 60 μbar with varied hydrogen dilution ratio (T_h = 410°C).

Pressure (μbar)	H_2 dilution ratio (%)	σ_{dark} $(\Omega cm)^{-1}$	σ_{photo} $(\Omega cm)^{-1}$	σ_d / σ_p
40	80	1.12E–11	1.81E-06	1.61E+05
	87	7.50E–12	3.68E-07	4.90E+04
	90	4.22E–09	2.34E-07	5.53E+01
	92	4.23E–07	2.58E-05	6.11E+01
	95	8.19E–06	1.96E-05	2.40E+00
60	87	1.13E–10	6.88E-07	6.08E+03
	90	1.43E–08	1.49E-06	1.04E+02
	92	3.82E–08	2.57E-07	6.74E+00
	95	1.06E–05	8.99E-05	8.47E+00

It can be noted from table 4.9 that the films dark conductivity values are in the expected range for a material in the phase transition regime; those grown with a low hydrogen dilution ratio (amorphous) have dark conductivity values close to that reported for an amorphous silicon 'device quality' film ($< 1 \times 10^{-10}\ \Omega^{-1}cm^{-1}$), those grown with moderate hydrogen dilution ratio show values approaching the reported value for a polycrystalline silicon 'device quality' film ($< 1.5 \times 10^{-7}\ \Omega^{-1}cm^{-1}$) [19]. An exception has however to be singled out for films grown with very high hydrogen dilution ratio (95%) where the recorded values were very high ($> 1 \times 10^{-6}\ \Omega^{-1}\ cm^{-1}$). We believe that such films are

porous and include a noticeable amount of oxygen as has been observed in their FTIR spectra, which show a peak of oxidation at around 1100 cm^{-1} (see figure 4.41.).

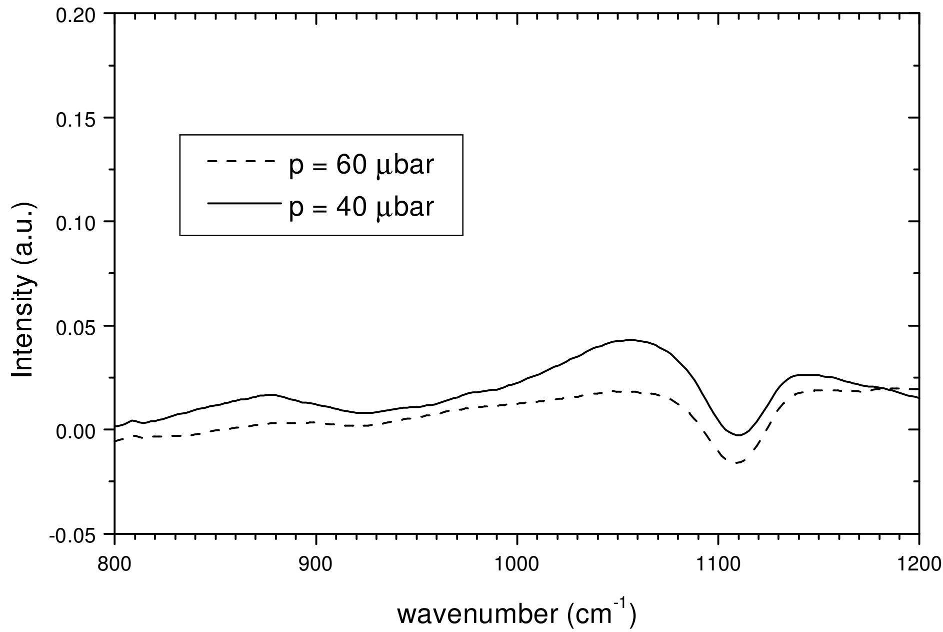

Figure 4.41. Infrared Transmittance spectra of two microcrystalline films deposited with 95% hydrogen dilution ratio showing peaks of oxidation. For both cases the substrate heater temperature was fixed at 410 °C.

Following table 4.9., the photoresponse has been observed to be strongly influenced by the hydrogen dilution ratio. For low dilution, when the films were still amorphous, a high value better than 10^4 has been observed, they compare well with the proposed value of 10^5 for an amorphous silicon 'device quality' sample [19]. With medium dilution ratios where the phase transition had been observed in our study, a sharp drop in photosensitivity values has been noted until eventually they stabilized just below 10^2. This sharp decrease can be attributed to the inclusion of defects such as grain boundaries and / or unwanted dopants in the films. Very high dilutions have even seen the photosensitivity to drop further; this regime corresponds to the growth of films with a crystalline volume fraction up to 50 % and an appreciable amount of oxygen. Figure 4.42

shows the trend variation of the photoresponse versus hydrogen dilution ratio for a fixed pressure of 40 μbar.

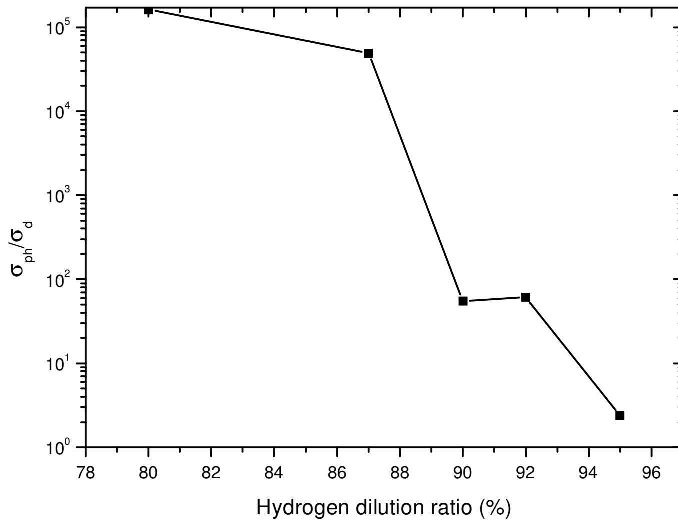

Figure 4.42. Photoresponse versus H_2 dilution ratios for films made at P = 40 μbar and T_h = 410°C.

4.5.3.2. Activation energy

The films have also been characterized for activation energy; the range variation of this parameter has been found between 0.9 and 0.3 eV. It describes well the material studied, which is ranging from amorphous to microcrystalline. An illustrative example of how they have been obtained from the slope of the plot $\sigma \sim 1 / T$ in its cooling part is shown in appendix 8. The displayed data are those of a microcrystalline sample with a crystalline volume fraction of ± 40% made at 90% hydrogen dilution ratio with a process pressure of 60 μbar and a substrate heater temperature of 410 °C. The closeness of the heating and the cooling parts in the graph is an indication of the quality of the studied intrinsic film.

In general for those comprising impurities such as oxygen, the cooling and the heating plots were observed apart due the improvement of the dark current with the annealing of the defects. This fact is shown in appendix 9 that displays the Arrhenius plot of the conductivity vs. the reciprocal temperature of a film 92% H_2 diluted with a deposition pressure of 40 µbar and a substrate heater temperature of 410 °C. The FTIR spectrum of this film (containing a crystalline volume fraction of 31.4%) had shown sign of oxidation as can be observed in figure 4.43.

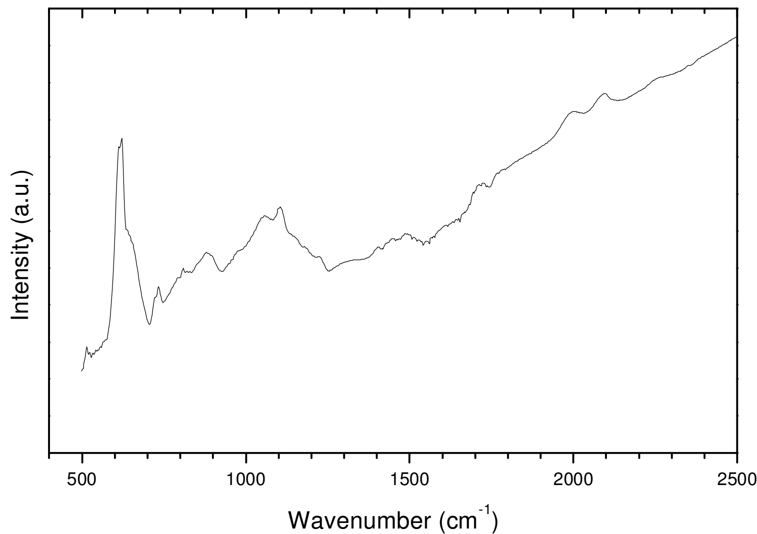

Figure 4.43. IR absorption spectrum of a microcrystalline film (V_f = 31%) showing a sign of oxidation at around 1100 cm^{-1}. The film was made at p = 40 µbar with 92% hydrogen dilution ratio.

As expected a decreasing trend of the activation energy values against the increase of the hydrogen dilution ratio was obtained (it was shown earlier that the crystallinity increases with the increase of the H_2 dilution ratio). This is a direct consequence of the reduction of the optical gap as the material heads towards crystallinity, and thus the separation between the Fermi level and the conduction band reduces subsequently. Figure 4.44 shows the decreasing trend of the activation energy with the increase of the hydrogen dilution ratio. It was noticed from our results that all the samples not showing any peak of crystallinity in Raman had an activation energy value greater than 0.8 eV, those at the

edge of crystallinity and / or microcrystalline had a range values $0.6 \leq E_a < 0.8$ eV provided that they were deposited with a hydrogen dilution ratio below 95%. Those made at this dilution all showed values below 0.5 eV. A good intrinsic and stable intrinsic material for solar cell purpose is expected to be in the second category if it shows at the same time a reasonable photosensitivity ($\geq 1 \times 10^2$). In this regard, three samples, from the studied set, have been identified as our best intrinsic films pending the results of the degradation studies; Table 4.10. gives the summary of their characteristics. All the three samples have a good absorption above 1×10^4 as measured at 2 eV; the first sample which is amorphous (the volume crystalline fraction = 0%) although photosensitive may suffer from the SWE while the second and the third (at the edge of crystallinity and clearly microcrystalline respectively) are expected to degrade little keeping at the same time a reasonable photosensitivity better than 1×10^2. Das *et al.* has done an extensive study of the degradation rate versus the material phase on samples prepared in PECVD [10].

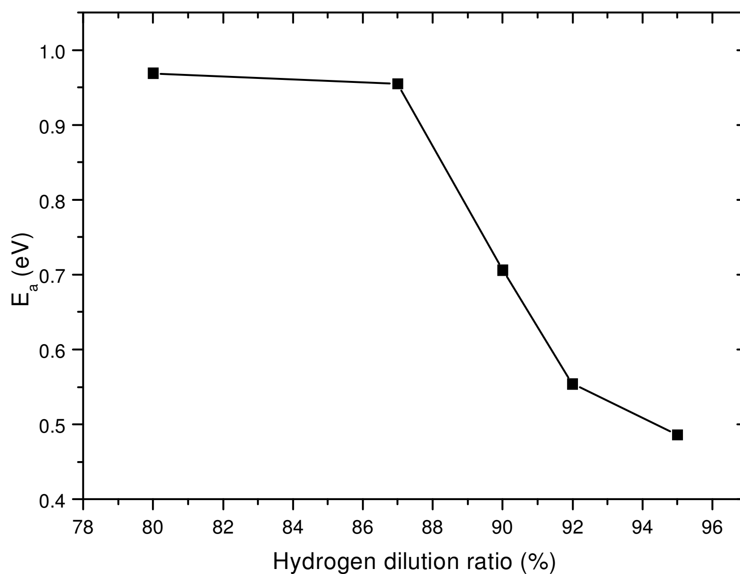

Figure 4.44. Activation energy vs. hydrogen dilution ratio. The films were prepared at T_h = 410°C with a fixed chamber pressure of 40 μbar.

Table 4.10. Summary of the characteristics of the best identified intrinsic material from this study.

R_{H2} (%)	P (µbar)	V_f(%)	R^* (a.u.)	α_{2eV} (cm^{-1})	$\sigma_{photo} / \sigma_{dark}$	E_a (eV)
80	40	0	0.14	2.00E+04	1.61E+05	0.96
87	60	6	0.25	2.58E+04	6.08E+03	0.78
90	60	40	0.35	1.99E+04	1.04E+02	0.68

4.5.3.3. Degradation of the films

The degradation of the samples is driven by an increased rate recombination process, which results in the creation of SW-defects [3]; it is characterised by a reduction in dark and photoconductivity. The process is however reversible after annealing although other structural related defects do not recover [102]. In practice two methods are used in degradation experiments: the excess photocarriers are injected in the material (electrons on the *n*-side and holes in the *p*-side in case of a solar cell) and recombine in the bulk of the device. The second method is via light soaking where the material is exposed to prolonged illumination and the excess photocarriers are induced by optical absorption. The latter approach has been used in our experiment. The light soaking experiment was performed using the same set up as the one used by Britton *et al.* [103]. The samples were illuminated nearly 300 hours and the photocurrents corresponding to an applied voltage of 50V were measured at different time intervals. The illumination was at times interrupted in order to read the dark currents. The two last rows in table 4.10. give the details of the nanocrystalline samples used in this study. They will be referred to as samples (a) and (b) respectively in the following discussion. They are compared to an amorphous film with the following characteristics: it was grown using a gas ratio R_H of 80% at a process pressure of 30 µbar. It was characterised for its amorphousness using both XRD and Raman scattering; its hydrogen content was found to be 5.7 at.% in FTIR whereas the absorption coefficient was calculated as 3.27 x 10^4 cm^{-1} from the UV-VIS transmission data. Its photoresponse and activation energy were respectively 4.4 E+03 and 0.81 eV. It will be referred to as sample (c).

Although the dark currents were too small to be detected in the case of the samples (a) and (c), it was successfully monitored in the case of the microcrystalline sample (b) and was observed to be little influenced by the soaking effect. In contrast the photocurrents have shown different deviations from the initial values depending on the phase of the probed material and will thus be our main focus in the following comparative discussions. As illustrated in figure 4.45., for the a-Si:H film (c) a sharp drop of 2 orders of magnitude has been noted during the first 20 hours. The sample stabilized afterward before experiencing a new minor decrease past the 100 hours of illumination. This new negative gradient extended however only over 20 hours before to observe a relatively stable trend during the remaining soaking period. It is thus observed that our HW hydrogen diluted a-Si:H deposited sample has a relatively good stability compared to PECVD amorphous films, which have been reported to degrade to a great extent and do not attain a stable value [10]. This good performance is attributed to an improved order in the material as it was previously proven by the obtained low values of bond angle variations $\Delta\theta$ in section 4.4.3. We believe that such improved order is due to the beneficial effect of the hydrogen dilution. The stability of the nanocrystalline film (a) was even better as the change in photocurrent after more than 200 hours of illumination was observed to be less than one order of magnitude. Furthermore the studied microcrystalline film (b) with a crystalline volume fraction of 45 % has shown no sign of degradation after several hours of illumination (around 300 hours). Although similar material had been previously reported to degrade very little, the lack of any observable degradation in this case coupled with a relative good photosensitivity ($> 10^2$) has however exceeded our expectations.

In the light of these degradation preliminary results, we believe that we have found a very promising regime of deposition where intrinsic films of high quality can be obtained.

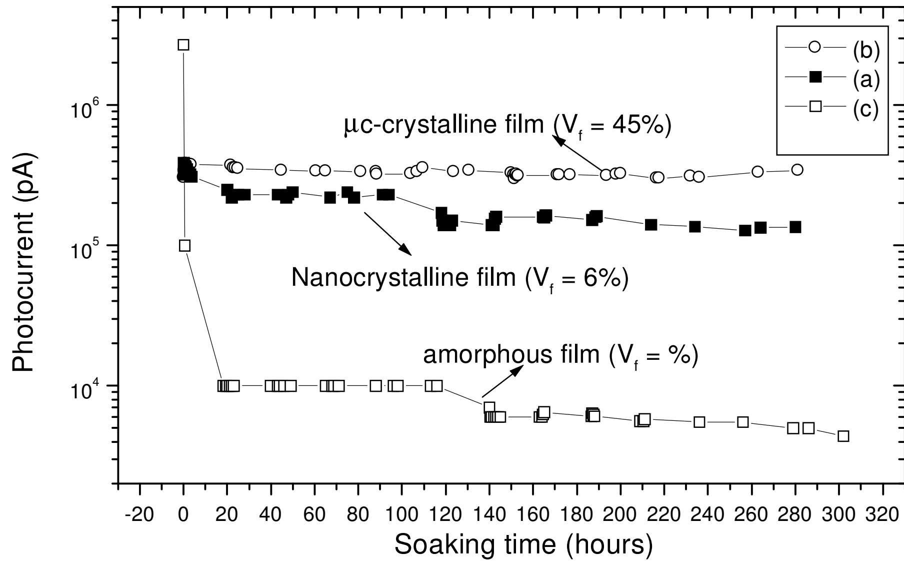

Figure 4. 45. Photocurrents plotted against soaking time for films with different phases.

Summary and conclusions

This study has focused on the deposition and characterisation of hydrogenated silicon films in the transition and microcrystalline phases.

In the introductory part, the basic theory of a *p-n* junction underlying the principle used by a solar cell for photons conversion into electric power has been given.

The second chapter has introduced the HWCVD technique, which has been used to deposit the material under study. Several issues pertaining the deposition process in HWCVD have been discussed.

The third chapter was dedicated to the background on the analytical techniques used in this investigation namely optical spectroscopy, FTIR, ERDA, XRD, Raman scattering and electrical conductivity.

The last chapter has highlighted the results of our investigation. It was found that the optical characteristics are strongly influenced by the amorphous network still remaining in the material. The refractive index, the absorption coefficient and the apparent Tauc E_g were comparable to those of amorphous films; absorption coefficient values better than 1 x 10^4 cm^{-1} were obtained in the visible region at a photon energy of 2 eV, and refractive indices in the range 2.9 - 3.4 were calculated. Both characteristics were observed to be decreasing when the crystallinity was increasing. The apparent E_g was found in the range 1.5 – 1.9 eV from the transmission data obtained by means of UV-visible spectroscopy. A measurement done on a microcrystalline sample using PDS down to near Infrared region has yielded an indirect E_g of 1.12 eV. This result, when related to the activation energy values found around 0.6 eV for such kind of material suggests that the last method is most appropriate given the fact that the Fermi level should lie in the middle of the forbidden gap for an intrinsic material. A sensitive technique covering a large spectrum range must then be used for the accurate extrapolation of the indirect optical gap for a µc.Si:H, as the so called Tauc edge [56] known for amorphous solids in their upper portion of the absorption plot against energy is not clearly occurring in crystals.

Although dependent on other technological parameters like the pressure and the substrate temperature, the phase transition from amorphous to crystalline has been observed to be strongly influenced by the hydrogen dilution ratio in the silane gas. Conclusive evidences

however from our FTIR results and from those on electrical conductivity have shown that very high dilutions are detrimental to the quality of the deposited intrinsic films.

In order to monitor the phase transition point, it was shown that a sensitive probing technique (e.g. Raman) was necessary to complement the XRD, since the latter was unable to show any Bragg diffraction peak in case of protocrystalline films. As a reference to future depositions in our chamber, for a Ta filament catalyser temperature of 1600°C at a moderate heater substrate temperature of 410°C in the optimum pressure range between 20 and 60 µbar, an hydrogen dilution ratio of 87% was good enough to observe the start of nucleation. We have shown that both the hydrogen dilution and the deposition pressure increase were instrumental in the increase of crystallinity, R_{H2} being the most influential.

The bonded hydrogen content for which the role has been discussed in the second chapter has been observed to decrease with the increase of crystallinity; it was even depleting to zero in samples made above substrate temperatures above 400 °C. As a consequence we have seen that the material grown in this regime was electronically poor. The microstructure parameter R^* has been noted to deteriorate as the hydrogen dilution was increasing, the phenomenon was attributed to the inclusion of crystallites that saw the hydrogen bonding change from mono to polyhydride.

The study on the electrical properties has shown that a moderate substrate heater temperature was most appropriate in yielding films with better photoresponse that compare well with the reported values. The characterisation for activation energy has produced values (in the range 0.9-0.3 eV) corresponding to the gradual departure from amorphous toward polycrystalline intrinsic Si films, as the hydrogen dilution ratio in the monosilane gas was increased. The degradation experiments have confirmed our claims that the inclusion of a certain volume fraction of crystals is beneficial to the stability of the intrinsic deposited film. It is worthy to highlight here that even the probed amorphous film seemed to stabilize during the first 300 hours of illumination in these preliminary investigations. We attribute this performance to the beneficial effect of hydrogen dilution. A systematic study will be dedicated to this important topic in the future for more conclusive results.

References

[1] D.E. Carlson, C.R. Wronski, Appl. Phys. Lett. **28**, (1976) 671.

[2] Wilfried G.J.H.M Sark, *Thin Films and Nanostructures*, Academic Press, San Diego, **30,** (2002) 1-125.

[3] K.F. Feenstra, *Hot-wire chemical vapour deposition of amorphous silicon and the application in solar cells*, Ph.D. thesis, Utrecht University, 1998.

[4] G. Munyeme, *Experimental and computer modelling studies of metastability of amorphous silicon based solar cells*, Ph.D. thesis, Utrecht University, 2003.

[5] B.G. Streetman, *Solid State electronic devices*, Fourth edition, Prentice Hall, Inc. (1995).

[6] W.E. Spear and P.G. Lecomber, Solid State Comm.**17**, (1975) 1193.

[7] K.N. Tu, J.W.Mayer and L.C. Feldman, *Electronic thin films Science for Electrical Engineers and Materials Scientists*, Mackmillan Publishing Company (1992).

[8] T. Markvat, *Solar Electricity*, Second Edition (2000).

[9] D.L. Staebler and C.R. Wronski, Appl.Phys. Lett. **31**, (1977) 292.

[10] C. Das, S.Ray, Thin Solid Films **403-404,** (2002) 81-85.

[11] C.J. Arendse, *Hydrogenated amorphous silicon: Optical properties and hydrogen concentration*, M.Sc. thesis, University of the Western Cape (1998).

[12] H.Wiesmann, A.K. Ghosh, T. McMahon, and M. Strongin, J. Appl. Phys. **50** (5), (1979) 3752-3754.

[13] H.L. Duan, G.A.Zaharias, S.F.Bent, MRS Symp. Proc. **715,** 2002.

[14] S. Tange, K. Inouie, K.Konokura, M.Koshi, Thin Solid Films **395,** (2001) 42.

[15] H. Matsumura, Japanese Journal of Applied Physics, **25** (12), (1986) L949-L951.

[16] J. Doyle, R. Robertson, G.H. Lin, M.Z. He and A. Gallagher, J. Appl. Phys. **64** (6), (1988) 3215-3223.

[17] J. Perrin, O. Leroy and M.C. Bordage, Contrib. Plasma Phys.**36**, (1996) 3.

[18] A.H. Mahan, J. Carapella, B.P. Nelson, R.S. Crandall, I. Balberg, J. Appl. Phys. **69,** (1991) 6728.

[19] R. E. I. Schropp and M. Zeman, *Amorphous and microcrystalline silicon solar cells: Modelling, Materials and Device Technology*, Kluwer Academic Publishers (1998).

[20] E. Bustarret, M.A. Hachida and M. Brunel, Appl. Phys. Lett. **52**, (1988) 1675.

[21] S. Baver, W. Herbst, B. Schröder, H. Oeschsner, 26th PVSC IEEE (1997) 719.

[22] S. Ray, C. Das, S. Mukhopadhyay, S.C.Saha, Solar Energy Materials and Solar Cells **74,** (2002) 393-400.

[23] M. Zhu, X. Guo, G. Chen, H. Han, M.He, K.Sun, Thin Solid Films (2000) 205-212.

[24] D. Soler, M. Fonrodona, C.Voz, J. Bertomeu, J. Andreu, Thin Solid Films **383,** (2001) 189-191.

[25] S. Klein, F. Finger, R. Carius, H. Wagner, M. Stutzmann, Thin Solid Films **395,** (2001) 305-309.

[26] A.H. Mahan, R.C. Reedy Jr., E. Iwaniczko, Q. Wang, B.P. Nelson, Y. Xu, A.C. Gallagher, H.M. Branz, R.S. Crandall, J.Yang, S. Guha, MRS Symp. Proc. **507,** (1998) 119.

[27] A.H.Mahan, Y. Xu, E. Iwaniczko, D.L Williamson, B.P. Nelson, Q. Wang, Journal of Non – Crystalline Solids **299-302,** (2002) 2-8.

[28] S.J. Jones, X. Deng, T. Liu, M. Izu, MRS Symp. Proc. **504,** (1998) 113.

[29] H. Matsumura, A, Masuda and A. Izumi, Mat. Res. Symp. Proc. **557,** (1999) 67-78.

[30] S. Morrison, U. Das, A. Madan, Solar energy materials and Solar cells **76,** (2003) 381-291.

[31] J.K. Rath, F.D. Tichelaar, H. Meiling and R.E.I. Schropp, Mat. Res. Soc. Symp. Proc. **507**, (1998) 879.

[32] H. Matsumura, Thin Solid Films **395,** (2001) 1-11.

[33] M. Konagai, T. Tsushima, M.K. Kim, K. Asakusa, A. Yamada, Y. Kudriavtsev, A. Villegas, R. Asomoza, Thin Solid Films **395,** (2001) 152-156

[34] S. M. Pietruszko, J. Jang, Solar Energy Materials & Solar Cells **71,** (2000) 459-464.

[35] R.A. Street, Physica B **170**, (1991) 69.

[36] D. Kwon and J. D. Cohen, Mat. Res. Soc. Symp. Proc., **377** (1995).

[37] J. D. Ouwens, *Characterization and application of wide band gap amorphous silicon*, Ph.D. thesis, Utrecht University, 1995.

[38] D.R. Penn, Physical Review, **128**, (1962) 2093-2097.

[39] P.V. Santos, W.B. Jackson, Phys.Rev. B**46**, (1992) 4595.

[40] M. Vanecek, Z. Remos, J. Fric, R.S. Crandal and A. H. Mahan, in proceedings of the 12th European Photovoltaic Solar Energy Conference, Amsterdam, the Netherlands (1994) 354-357.

[41] K.J. Laidler, J.H. Meiser, *Physical Chemistry*, second edition (1995).

[42] J. Tauc, in *Optical Properties of Solids*, edited by F. Abelès (North-Holland, Amsterdam, the Netherlands) (1972) 277.

[43] R.H. Klazes, M.H.L. van der Broek, J.Bezemer and Radelaar, Philos. Mag. B**45**, (1982) 377.

[44] K.D. Mackenzie, J.R. Eggert, D.J. Leoplod, Y.M. Li, S. Lin, W. Paul, Phys. Rev. B**31**, (1985) 2198.

[45] R. Swanepoel, J. Phys.E: Sci. Instrum., **17**, (1984) 896-903.

[46] R. Swanepoel, Journal of Physics E: Scientific Instruments, **16**, (1983) 1214-1222.

[47] B.D. Cullity, *Elements of X-ray Diffraction*, Addison-Wesley, Reading, MA (1978).

[48] P.E.J. Flewitt and R.K. Wild, *Physical methods for materials characterization*, IOP Publishing Ltd. (1994).

[49] P. van Veenendaal, *Hot-wire chemical vapor deposition of polycrystalline silicon From gas molecule to solar cell*, Ph.D. thesis, Utrecht University, 2002.

[50] P. Brogueira, J.P. Conde, S. Arekat, V. Chu, J. Appl. Phys. **79**(11), (1996) 8748.

[51] S.R. Jadkar, J.V. Sali, D.V. Musale, S.T. Kshirsagar, and M.G. Takwale, Solar Energy Materials & Solar Cells **71,** (2002) 153-167.

[52] A.J.M. Berntsen, W.G.J.H.M. van Sark and W.F. van de Weg, J. Appl. Phys. **78**(3), (1995).

[53] D. Beeman, R. Tsu, M.F. Thorpe, Physical Review B, **32**(2), (1995).

[54] J.C. Vickerman, *Surface analysis – the principal techniques*, John Wiley & Sons (1997).

[55] W.S. Lau, *Infrared characterisation of microelectronics*, World Scientific, Singapore (1999).

[56] R. Zallen, *The physics of amorphous solids*, John Wiley & Sons (1983).

[57] A.A. Langford, M.L. Fleet, B.P. Nelson, W.A. Lanford and N.Maley, Phys.Rev. B**45**, (1992) 13367.

[58] W. Beyer and M.S. Abo Ghazala, Mat. Res. Symp. Proc. **507**, (1998) 601.

[59] A.H. Mahan, *Properties of Amorphous Silicon and its Alloys*, INSPEC, The Institution of Electrical Engineers, (London, UK), (1998) 39-46.

[60] A.H. Mahan, P. Raboisson, R. Tsu, Appl.Phys.Lett. **50**, (1997) 335.

[61] B.L. Doyle and D.K. Brice, Nuclear Instruments and Methods in Physics Research B**35,** (1988) 301-308.

[62] L.C. Feldman and J.W. Mayer, *Fundamentals of surface and thin film analysis*, Elsevier Science Publishers B.V., Amsterdam (1986).

[63] J. L'Ecuyer, C. Brassard, C. Cardinal, J. Chabbal, L. Deschênes, J.P.Labrie, B. Terreault, J. G. Martel and R.St. Jacques, Journal of Applied Physics, **47** (1), (1976) 381-382.

[64] J.R. Tesmer, M. Nastasi, J.C. Barbour, C.J.Maggiore and J.W. Mayer, *Handbook of modern ion beam materials analysis*, Materials Research Society, 1995.

[65] J. Tirira, Y. Serruys and P. Trocellier, *Forward Recoil Spectrometry, Application to Hydrogen Determination in Solids*, Plenum Press, New York, 1996.

[66] J. B. Marion and F.C. Young, Nuclear Reaction Analysis (North –Holland, Amsterdam), (1968) 142.

[67] M. Mayer, *SIMNRA user's guide, Technical report IPP 9/113*, Max-Planck-Institut für Plasmaphysik, Garching, Germany, 1997.

[68] P.J.Goodhew and F.J. Humphreys, *Electron microscopy and analysis* (second edition), (1988).

[69] R.A. Street, *Hydrogenated amorphous silicon*, Cambridge University Press (1991).

[70] Zdeněk Remĕs, *Study of defects and microstructure of amorphous and microcrystalline silicon thin films and polycrystalline diamond using optical methods*, PhD. Thesis, Institute of Physics of the Academy of Sciences of the Czech Republic (1999) 2.

[71] Swanepoel, *Properties of amorphous silicon and its alloys*-ed.Tim Searle, Emis data-review series, University of Sheffield, U.K. (1998).

[72] E.C. Freeman and W. Paul, Phys. Rev. B**20**, (1979) 716.

[73] P.D. Persans, A. F. Ruppert, S.S. Chan, and G.D. Cody, Solid State Commun. **51**, (1984) 203.

[74] D.E Sweenor, S.K. O'Leary, and B.E. Foutz, Mat.Res. Soc. Symp. Proc. **557,** (1999) 55-60.

[75] J.K.Rath, H. Meiling and R.E.I. Schropp, Jpn.J.Appl. Phys. **36,** (1997) 5436-5443.

[76] N. Beck, J. Meier, J. Fric, Z. Remes, A. Poruba, R. Fluckiger, J. Pohl, A. Shah and M. Vanecek, J. Non-Cryst. Solids **198-200**, (1996) 903.

[77] M.J. van den Boogaard, *Microvoids and hydrogen diffusion in hydrogenated amorphous silicon*, Ph.D. thesis, Utrecht University, the Netherlands, 1992.

[78] H. Meiling, M.J. van den Boogard, R.E.I. Schropp, J. Bezemer, and W.F. van der Weg, Mater. Res. Soc. Symp. Proc. **192**, 645 (1990).

[79] S.R Jadkar, J.V. Sali, S.T. Kshrisagar, M.G. Takwale, Thin Solids Films **437,** (2003) 18-24.

[80] J. Yang and Guha, Mat. Res. Soc. Symp. Proc. **557,** (1999) 239-250.

[81] User's manual, PDFMaint Powder Diffraction Datab ase Version 4.0, Bruker Analytical X-Ray Systems (1997).

[82] R.L.C Vink, G.T. Barkema, W. F. van der Weg, Phys.Rev. B **63**, (2001) 115210.

[83] A. Gordijn, J. Löffler, W.M. Arnolbik, F.D. Tichelaar, J.K. Rath, R.E.I. Schropp, Solar Energy Materials & Solar Cells **87,** (2005) 445-455.

[84] Qi Wang, Guozhen Yue, Jing Li, Daxing Han, Solid State Communications **113**, (2000) 175-178

[85] Joohyun Koh, H. Fujiwara, Yeeheng Lee, C.R. Wronski, R.W. Collins, Mat.Res.Soc.Symp.Proc. **536**, (1999)

[86] Guozhen Yue, J.D. Lorentzen, Jing Lin, Qi Wang, Daxing Han, Appl. Phys. Lett. **75**, (1999) 492.

[87] S. Veprek, Z. Iqbal, and F.A. Sarott, Philos. Mag. B **45**, (1982) 137.

[88] T. Taneko, M. Wakagi, K. Onisawa and T. Minemura, Appl. Phys. Lett. **64** (14), (1994) 1865.

[89] D.L. Greenway, G.Harbeke, *Optical Properties of Semiconductors*, Pregamon, New York, 1968.

[90] H. Richter and L Ley, J. Appl. Phys. **52**, (1981) 7281.

[91] A.H. Jayatissa, Y. Hatanaka, Y. Nakanishi and K. Ishikawa, J. Phys. D: Phys. **29**, (1996) 1636-1640.

[92] Paulo V. Santos, J. Phys.: Condens. Matter **5**, (1993) A335-A336.

[93] Paulo V. Santos and Warren B.Jackson, Physical Review B **46** (8), (1992) 4595-4606.

[94] R.E. Norberg, D.J. Leopold, P.A. Fedders, Journal of Non-Crystalline Solids **227 – 230,** (1998) 124-127.

[95] A.H. Mahan, D.L. Williamson and T. E. Furtak, Mat. Res. Soc. Symp.Proc. **467**, (1997) 657-661.

[96] M.Heintze, R. Zedlitz, H.N. Wanka, M.B. Schubert, J. Appl. Phys. **79**, (1996) 2699.

[97] R.L.C. Vink, G.T. Barkema, W.F. van der Weg, Phys. Rev.B **63**, (2001) 115210.

[98] M. A. Green, *Solar Cells, Operating Principles, Technology and System Applications*, Prentice-Hall, Inc., Englewood Cliffs, N.J. 07632, (1982) 7.

[99] M. Kondo, T. Matsui, Y. Nasuno, H. Sonobe, S. Shimizu, *Extended abstract of the 3rd International Conference on Hot-Wire CVD (Cat-CVD) Process*, Utrecht, The Netherlands. (2004) 243-245.

[100] J. Guillet, C. Niikura, J.E. Bourée, J. P. Kleider, C. Longeaud, R. Brüggemann, Materials Science and Engineering B**69-70** (2000) 284-288

[101] Daxing Han, Guozhen Yue, J. D. Lorentzen, and Jing Lin, J. Appl. Phys. **87**(4), (2000) 1882-1888

[102] X. Zou, Y.C. Chan, D.P. Webb, Y.W. Lam, Y. F. Hu, C. D. Beling, S. Fung, H.M. Weng, Phys. Rev. Lett. **84** (2000) 769-772.

[103] D.T. Britton, Z. Sigcau, C.M. Comrie, D.F. Kanguwe, E. Minani, D. Knoesen, M. Härting, Thin Solid Films **430,** (2003) 149-152.

[104] S.Halindintwali, *Etude de l'Evolution des Paramètres Electriques caractéristiques d'une Photopile au Silicium avec la Température*, M.Sc. thesis, National University of Rwanda (1989).

[105] M. Bashahu et S. Halindintwali, *Variation de paramètres d'une cellule solaire avec la température*, Revue Rwandaise des Sciences **5**(2), (1992) D-87-D-111.

Appendices

Appendix 1: Urbach edge

In a-Si:H, the conduction and valence bands have tail-states where the absorption coefficient is above zero. This form of absorption occurs typically for α-values between 1 and $3x10^3$ cm^{-1} in a-Si:H [69]. The shape of the curve α *(E)* has an exponential form usually fitted to $\alpha = \alpha_0 \exp(E / E_u)$ where E_u is known as *Urbach energy* [37]. E_u can thus be calculated from the slope of the function $\ln \alpha = \ln \alpha_0 + \frac{E}{E_u}$. As the slope reflects the shape of the band tails, it follows that E_u varies with structural disorder. E_u is usually found between 50 and 100 meV departing from a device quality to a disordered a-Si:H material. In this thesis we have used other parameters to estimate the degree of order in the material (see section 4.4.3).

Appendix 2: Void fraction v_f

Voids are volume defects occurring in crystals growth. The void volume fraction (v_f) can be defined in a-Si:H as the ratio of the volume where Si atoms are missing to the total volume of the material if it is assumed that the bulk consists only of silicon atoms. This assumption arises from the fact that in SAXS (Small– Angle X-Ray Scattering) experiments (as effectively used for the calculation of v_f), the contributions by hydrogen in the bulk to the scattering and the absorption of X-rays are negligible compared to those of silicon [77]. We refer the interested reader to reference 77 for ample discussions on microvoids and the relation between clustered hydrogen and void surfaces.

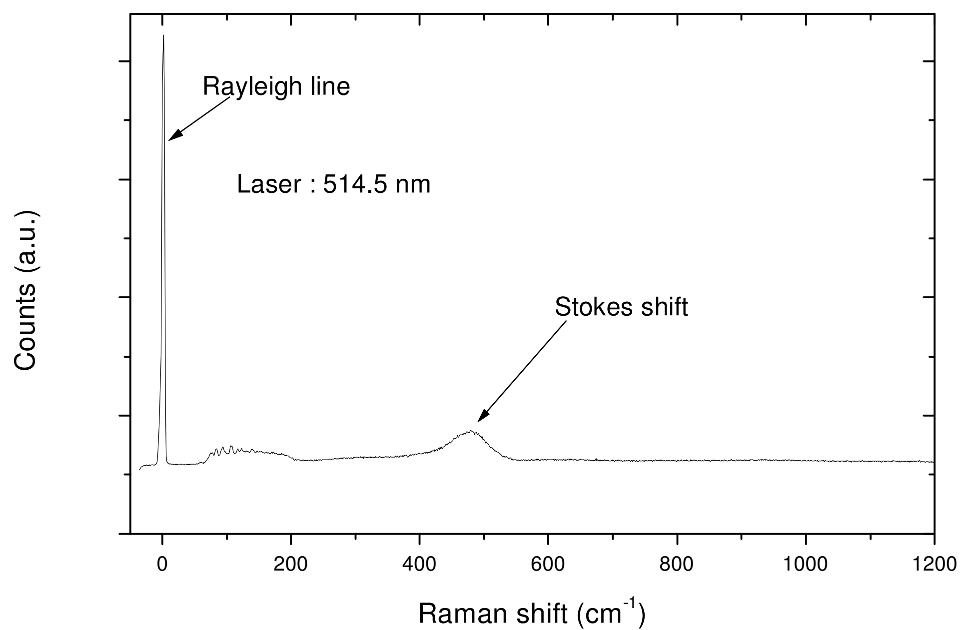

Appendix 3 Raman scattering from amorphous silicon deposited on a glass substrate.

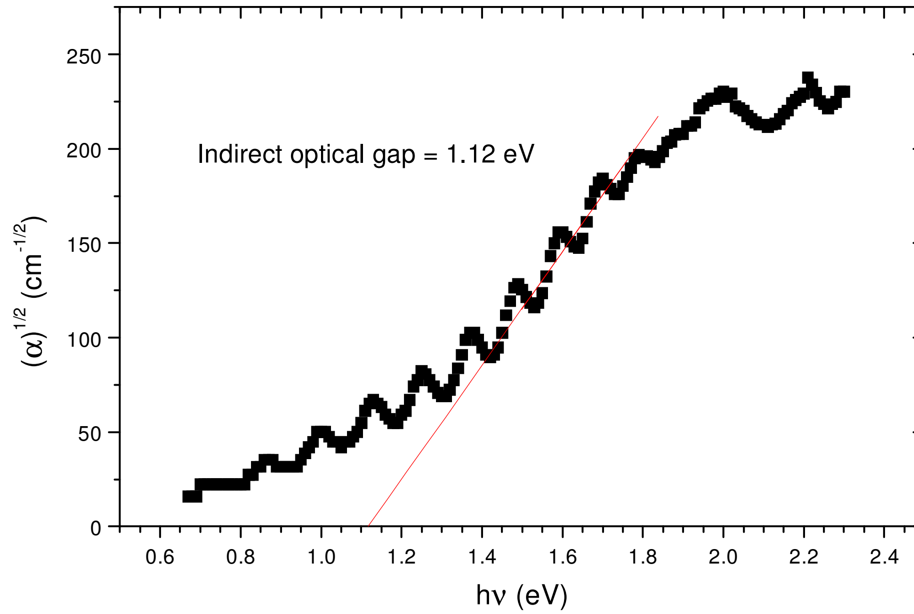

Appendix 4 Square root of the absorption coefficient (α) versus energy plot for indirect E_g extrapolation in PDS.

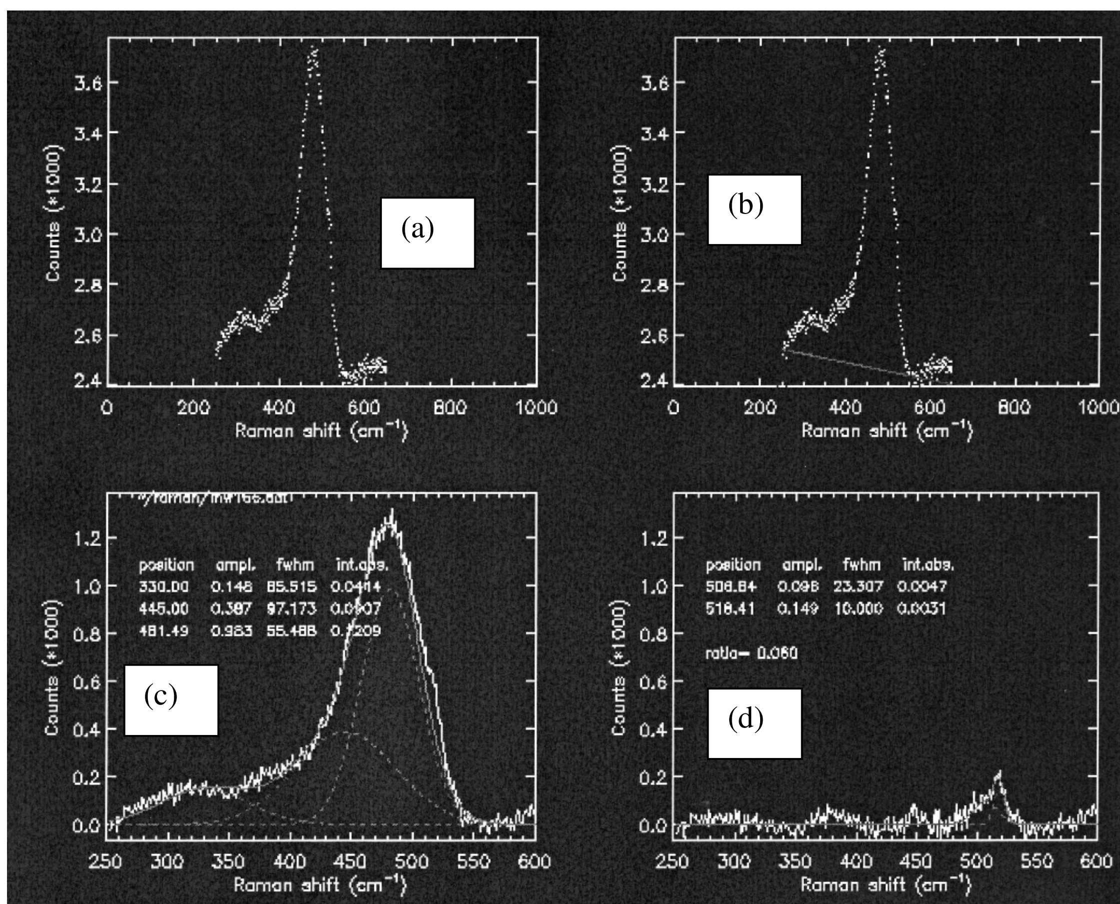

Appendix 5 Raman deconvolution spectra of a film deposited at the edge of crystallinity (R_{H2} = 87%; P = 60 µbar and T_h = 410°C). The crystalline volume fraction is calculated to be 6%. (a) The spectrum as taken; (b) The background subtraction; (c) The amorphous contribution fitting (The fitting range is chosen in such way that the crystalline contribution is not influencing the fit); (d) The crystalline contribution fitting (The amorphous contribution is subtracted before the fitting procedure).

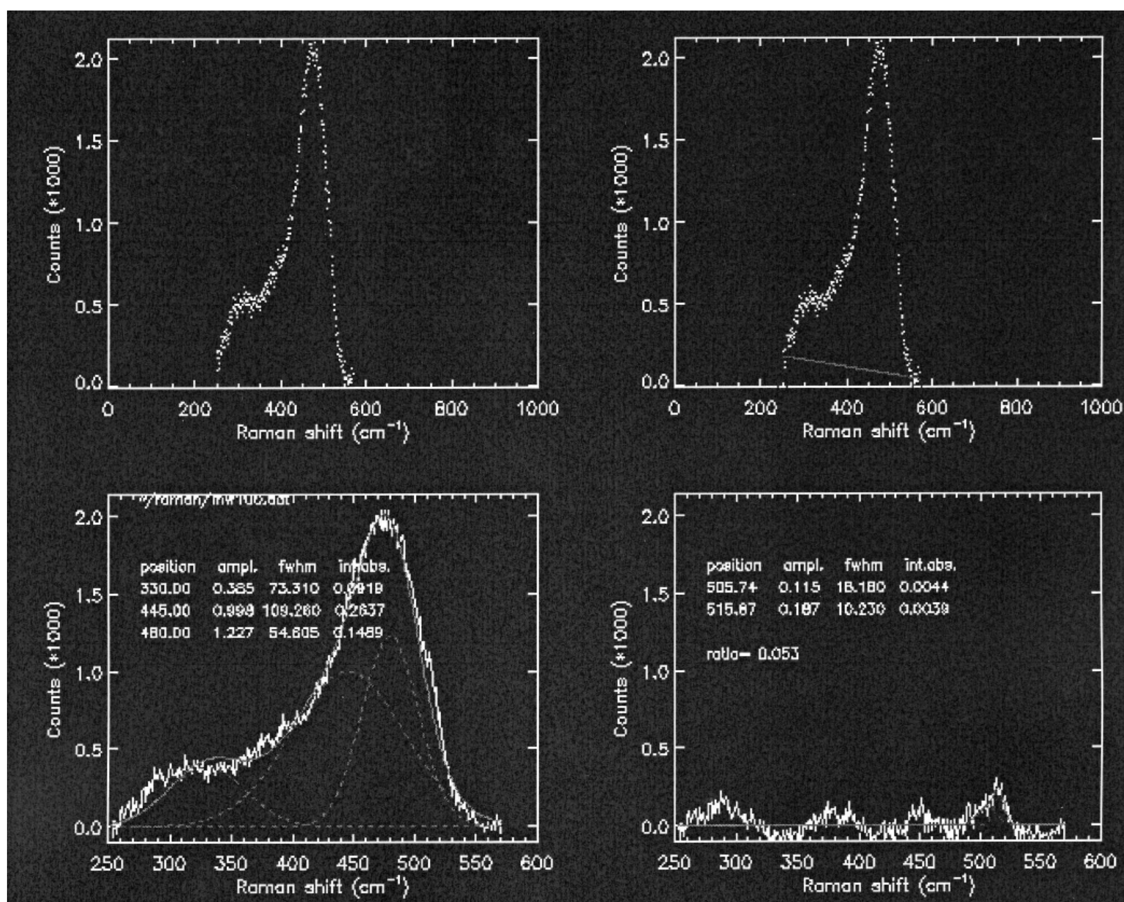

Appendix 6 Raman deconvolution spectra for a film at the edge of crystallinity deposited on a glass substrate with the following parameters: R_H = 90%; P = 20μbar; T_h = 450°C and d_{s-f} = 18 mm. The calculated crystalline volume fraction is 5%.

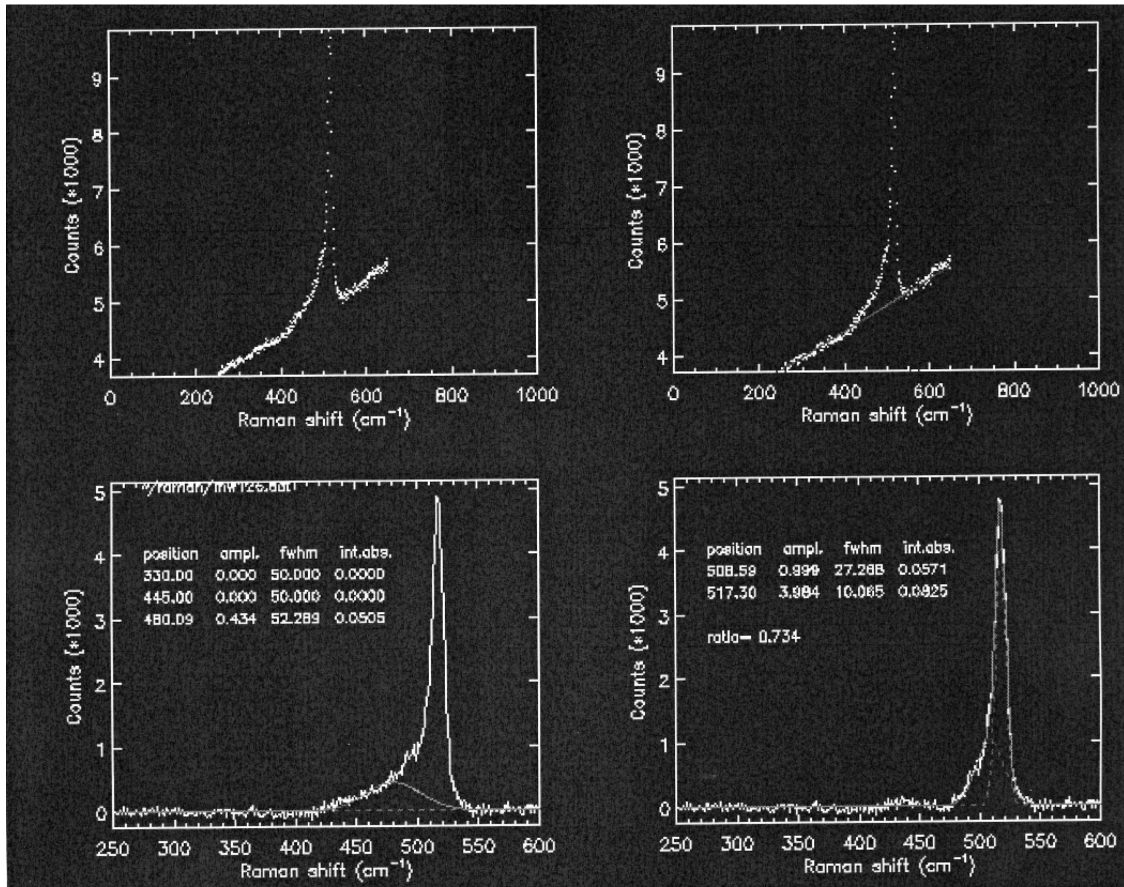

Appendix 7 Raman deconvolution spectra of a highly H_2 diluted film (R_{H2} = 95%) with 73% calculated crystalline volume fraction; the sample was deposited at T_h = 450°C with a process pressure of 30 µbar.

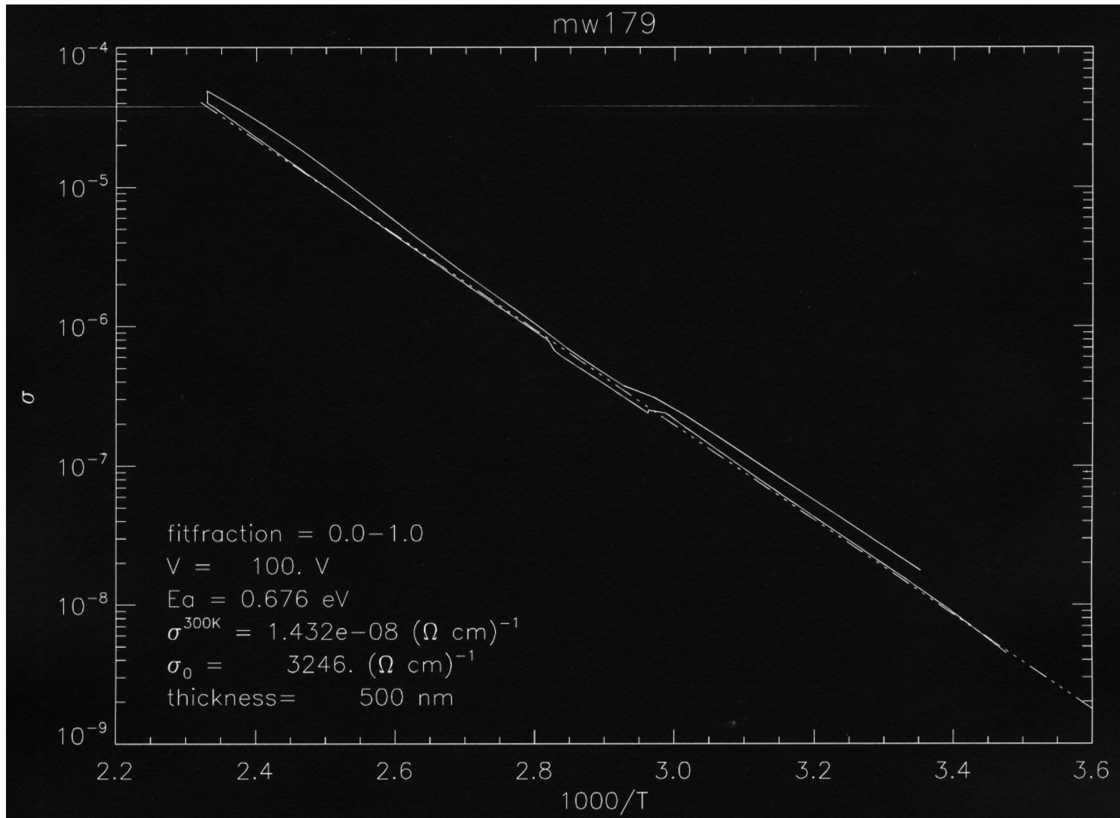

Appendix 8 Arrhenius plot displaying the conductivity for both heating and cooling steps for activation energy calculation of a film 90% H_2 dilution diluted deposited at a process pressure of 60 μbar and a substrate heater temperature of 410°C. Note how the two graphs are close to one another.

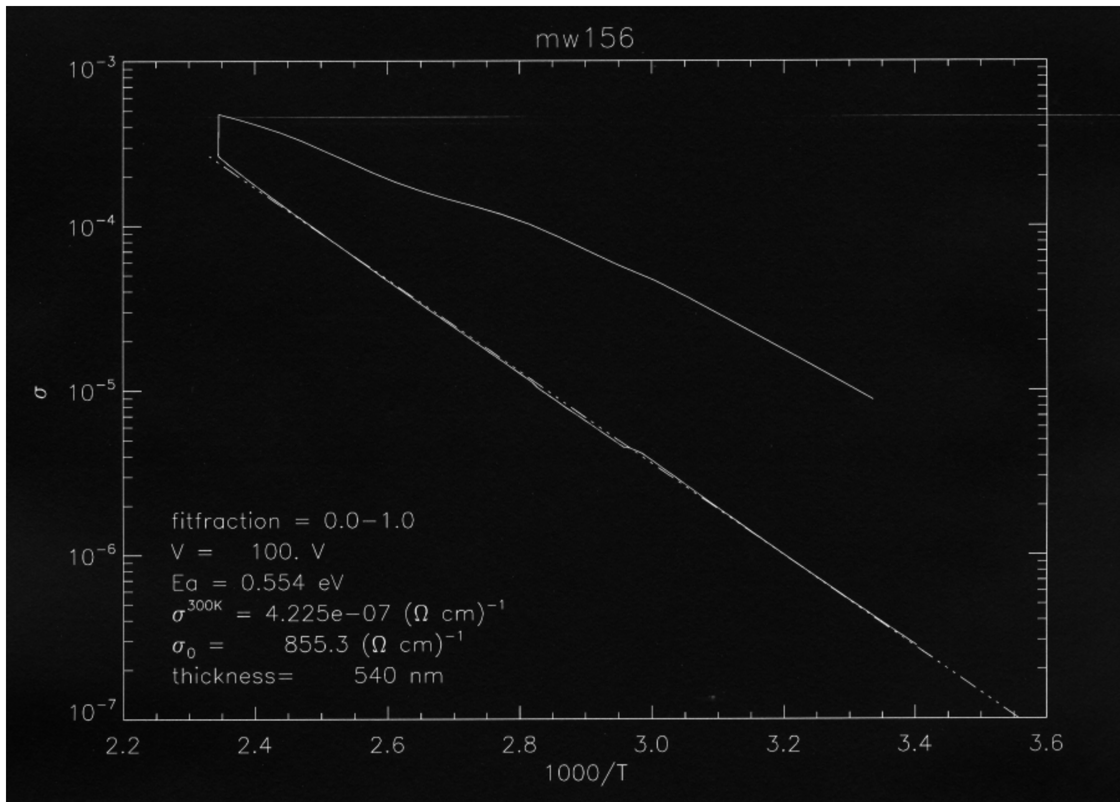

Appendix 9 Heating and cooling plots of the dark conductivity vs. 1000/*T* for a typical microcrystalline sample (V_f = 31.4%) with some degree of post oxidation. The upper graph correspond to the heating and the lower part correspond to the cooling. The registered lower values of the dark conductivity translate the improvement of the electronic properties of the films after annealing. The film was prepared with R_{H2} = 92%; P = 40 μbar and T_h = 410°C. Note how the heating and the cooling contributions are apart from each other.